学位論文

Search for η' mesic nuclei by missing-mass spectroscopy of the ^{12}C(p, d) reaction

（^{12}C(p, d)反応の分光によるη'中間子原子核の探索）

平成27年12月　博士（理学）申請

東京大学大学院理学系研究科

物理学専攻

田中 良樹

Search for η' mesic nuclei by missing-mass spectroscopy of the $^{12}\mathrm{C}(p, d)$ reaction

Doctoral Dissertation

by

Yoshiki Tanaka

December 2015

Department of Physics, Graduate School of Science,

The University of Tokyo

Abstract

One feature of the η' meson is its especially large mass compared with the other pseudoscalar mesons. Theoretically, the large mass of the η' meson is understood by the $U_A(1)$ anomaly, and this anomaly effect on the η' mass is expected to be present only with spontaneous and/or explicit breaking of chiral symmetry. In the nuclear medium, chiral symmetry is partially restored, and the mass of the η' meson can be reduced. Since such a mass reduction induces an attraction between an η' meson and a nucleus, existence of η' meson-nucleus bound states (η' mesic nuclei) is theoretically suggested.

We performed, for the first time, an experimental search for η' mesic nuclei by means of the missing-mass spectroscopy of the ^{12}C(p,d) reaction. A 2.5 GeV proton beam of SIS-18 at GSI was employed to produce the η' mesic nuclei via the ^{12}C(p,d)^{11}C$\otimes\eta'$ reaction. The momentum of the ejectile deuteron was measured by the FRS spectrometer to obtain the missing mass in the reaction. The spectrometer system was calibrated by measuring the proton-deuteron elastic scattering with a CD_2 target.

We successfully obtained an excitation-energy spectrum of ^{11}C around the η' production threshold. A high statistical sensitivity of a level better than 1% was achieved owing to a high-intensity primary beam and a thick carbon target. At the same time, an experimental resolution of 2.5 MeV was achieved, which is sufficiently smaller than the expected widths of the η' mesic nuclei.

Since no clear peak structure was observed in the excitation-energy spectrum, we determined upper limits for the formation cross sections of the η' mesic states as a function of the energy and the width of the assumed state. The determined upper limits around the η' production threshold are 0.1–0.2 μb/sr for the width of $\Gamma = 5$ MeV, 0.2–0.4 μb/sr for $\Gamma = 10$ MeV, and 0.3–0.6 μb/sr for $\Gamma = 15$ MeV at 95% confidence level. These limits are as small as theoretically-expected cross sections in cases of deep η'-nucleus potential. The obtained spectrum was also directly compared with the theoretically-calculated spectra to discuss a limitation on the η'-nucleus potential parameters.

Contents

List of Figures

List of Tables

Chapter 1

Introduction

1.1 Physics Motivation

Understanding of the hadron masses is one of the important subjects in hadron physics. While hadrons have a typical mass scale of ~ 1 GeV/c^2, the light quarks have masses of the order of $m_{u,d} \sim 5$ MeV/c^2 and $m_s \sim 100$ MeV/c^2. A spontaneous breaking of chiral symmetry in the low-energy region of QCD is considered to play an important role in dynamical generation of the hadron masses.

Our experiment studies on the η' meson, which is one of the pseudoscalar mesons with a mass of 958 MeV/c^2. This η' mass is peculiarly large compared with the other pseudoscalar mesons, π, K, and η mesons, as it has been attracting interest known as the $U_A(1)$ problem [1]. Theoretically, the large mass of the η' meson is explained by $U_A(1)$ anomaly, which breaks $U_A(1)$ symmetry explicitly [2, 3]. Then, the η' meson is not necessarily a Nambu-Goldstone boson, while the π, K, and η mesons are considered as Nambu-Goldstone bosons associated with spontaneous breaking of chiral symmetry.

Figure 1.1 schematically explains the pseudoscalar-meson spectrum with three situations of chiral symmetry [4]. The left stage shows a case when chiral symmetry is not broken spontaneously nor explicitly. As the anomaly effect on the η' mass is theoretically considered to be present only with the spontaneous and/or explicit breaking of chiral symmetry [3, 5, 6], in this case the nine mesons are expected to have a common mass. Next, in the middle stage, spontaneous breaking of chiral symmetry is introduced. The singlet meson acquires a finite mass due to the $U_A(1)$ anomaly, while the other mesons become massless Nambu-Goldstone bosons. In the right stage, explicit chiral symmetry breaking by the quark masses is also introduced, and this corresponds to the mass spectrum observed in vacuum.

In finite baryon density, chiral symmetry is partially restored, and quark condensate $\langle \bar{q}q \rangle$, which is an order parameter of chiral symmetry, is expected to be reduced by about 30% at normal nuclear density [7–9]. Since the large η' mass is explained by the interplay between the $U_A(1)$ anomaly and chiral symmetry breaking, the η' mass may be reduced in finite nuclear density. A possible mass reduction has been theoretically studied by various model calculations, and, for example, about 150 MeV/c^2 reduction is expected at normal nuclear density by the Nambu-Jona-Lasinio model [10, 11], as described in Section 1.2. Such a mass reduction in the nuclear density induces an attraction between an η' meson and a nucleus, and existence of η' meson-nucleus bound states is suggested. [3, 4, 10, 12].

Our experiment aims to investigate the proposed η' meson-nucleus bound states, which are called η' mesic nuclei. From an experimental point of view, such a meson-nucleus bound system provides an unique opportunity to directly study in-medium properties of the meson. If an η' mesic nucleus is observed as a certain quantum state, we can determine the

η'-nucleus potential, in which the in-medium mass reduction and the width are embodied, and therefore we can extract these in-medium properties experimentally.

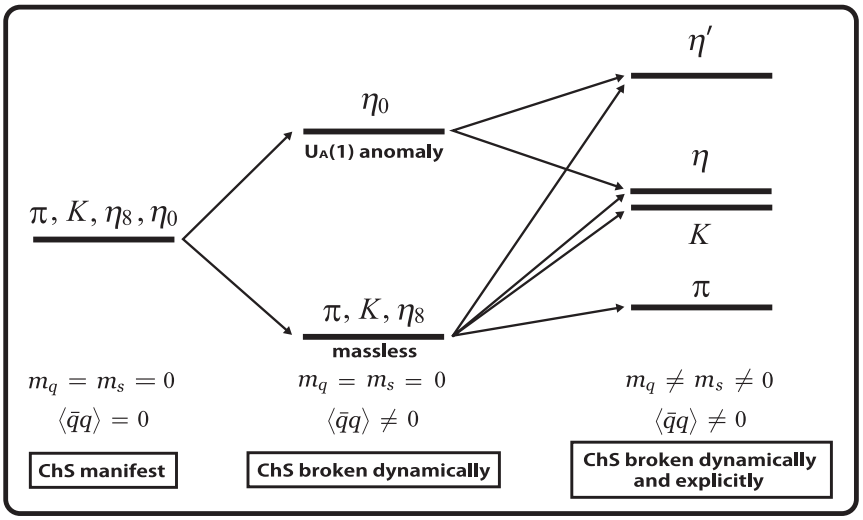

FIGURE 1.1: Pseudoscalar meson spectrum in three patterns of chiral symmetry. This figure is taken from Nagahiro *et al.* [4]

1.2 Theoretical Studies on η' Meson at Finite Density

1.2.1 η' mass at finite density

A possible mass reduction of the η' meson at finite density has been theoretically studied in model calculations. In this section, the theoretical predictions for the in-medium η' mass are briefly described.

In Nagahiro *et al.* [10] and Costa *et al.* [11], the η' mass at finite density is evaluated by the Nambu-Jona-Lasinio (NJL) model [13, 14]. The model contains a term called Kobayashi-Maskawa-t'Hooft (KMT) interaction [15–17], which explicitly breaks the $U_A(1)$ symmetry. Figure 1.2 shows obtained density dependence of the η' mass by Nagahiro *et al.* [10], for three cases of the strength of the KMT interaction: a constant strength (a), a zero strength (b), and a density dependent strength (c). The results show the η' mass is expected to be reduced in finite density when the $U_A(1)$ symmetry breaking term is present, as observed in the cases (a) and (c). The expected mass reduction at the nuclear saturation density ρ_0 is as large as 150 MeV/c^2 by considering the case (a) of Figure 1.2.

Sakai and Jido [18] considered the linear sigma model to evaluate the η' mass in finite density. Figure 1.3 shows their results of the meson masses as functions of the nuclear density. In this model, the η' mass is expected to be reduced by about 80 MeV/c^2 at the nuclear saturation density $\rho_0 = 0.17$ fm^{-3}.

Another model calculation was given by Bass and Thomas [19] using the Quark-Meson-Coupling (QMC) model. The evaluated mass reduction at the nuclear saturation density is 37 MeV/c^2 for the η-η' mixing angle of 20°.

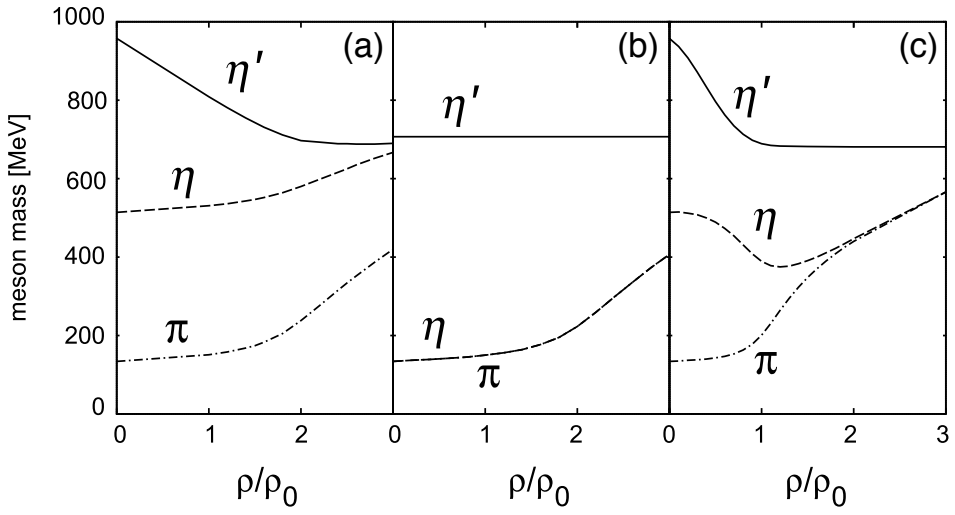

FIGURE 1.2: Density dependence of the meson masses calculated with the NJL model. This figure is taken from Nagahiro *et al.* [10] Three cases for the strength of the KMT interaction are shown: a constant strength (a), a zero strength (b), and a density dependent strength (c).

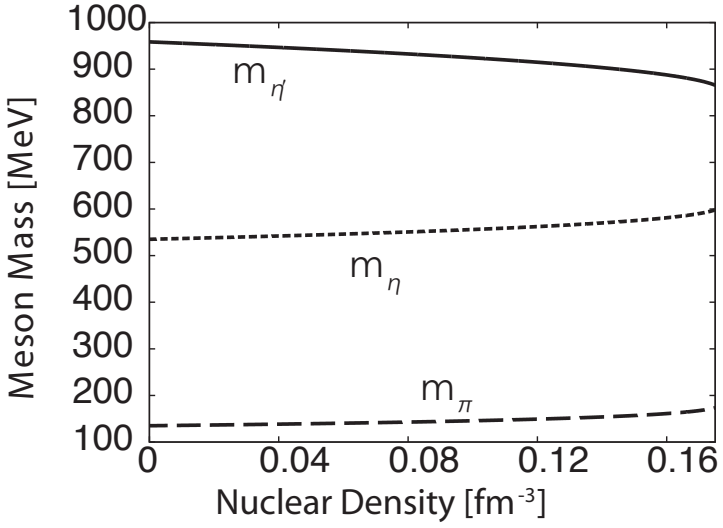

FIGURE 1.3: Density dependence of the meson masses calculated by the linear sigma model. This figure is taken from Sakai and Jido [18].

1.2.2 η' meson-nucleus bound states

Existence of η' meson bound states in nuclei has been theoretically discussed with an η'-nucleus potential induced by the η' mass reduction at finite density. Here, we consider the Klein-Gordon equation,

$$[-\nabla^2 + m_{\eta'}^2 + 2m_{\eta'}U_{\eta'}(r)]\phi(\vec{r}) = E^2\phi(\vec{r}), \tag{1.1}$$

where $m_{\eta'}$ is the η' mass in vacuum, E and $\phi(\vec{r})$ are the energy and the wave function of the bound states. For the η'-nucleus optical potential $U_{\eta'}(r)$, an empirical form of

$$U_{\eta'}(r) = (V_0 + iW_0)\frac{\rho(r)}{\rho_0} \tag{1.2}$$

is assumed. This potential is parameterized by V_0 and W_0, the real part and the imaginary part of the potential at the nuclear saturation density ρ_0. $\rho(r)$ denotes a nuclear density distribution, for which an empirical Woods-Saxon form is assumed. Then, a mass reduction at the nuclear saturation density, $\Delta m_{\eta'}(\rho_0)$, can be translated into the potential by substituting

$$m_{\eta'}^2(\rho) = (m_{\eta'} + \Delta m_{\eta'}(\rho))^2 \sim m_{\eta'}^2 + 2m_{\eta'}\Delta m_{\eta'}(\rho). \tag{1.3}$$

for the mass term $m_{\eta'}^2$ in the Klein-Gordon equation, and thus we can interpret the mass reduction as the real part of the potential by

$$V_0 = \Delta m_{\eta'}(\rho_0) \tag{1.4}$$

from the second term of Equation (1.3).

Bound states are calculated by solving the Klein-Gordon equation for given potential parameters V_0 and W_0. Figure 1.3 shows calculated η' bound states in ^{11}C for $(V_0, W_0) = (-100, -20)$, $(-150, -20)$, $(-200, -20)$, $(-100, -50)$ MeV by Jido *et al.* [3] Bound states are expected even in a small nucleus like carbon. Their binding energies and widths are plotted for each η' angular momentum labeled by "s", "p", and "d". As observed in this figure, if the imaginary part of the potential is relatively small, the bound states are expected to be well separated. In this case, the bound states can be observed as clear peaks.

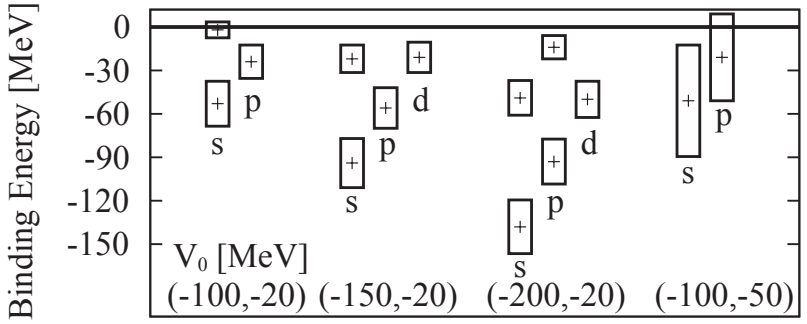

FIGURE 1.4: Calculated level structure of the η' meson bound states in ^{11}C are shown for $(V_0, W_0) = (-100, -20)$, $(-150, -20)$, $(-200, -20)$, $(-100, -50)$ MeV. This figure is taken from Jido *et al.* [3]

1.3 Experimental Situation

Experimentally, information on the in-medium η' meson or the η'-nucleus potential is not well known so far. There are only a few experiments which discuss the η'-nucleus interaction in rather indirect methods. In this section, these experimental situations are described.

CBELSA/TAPS experiment

A photo-production of the η' meson off nuclear targets has been studied by the CBELSA/TAPS collaboration at the ELSA facility. Nanova *et al.* [20] measured transparency ratios in the photo-production of the η' meson with an incident photon energy of 1.6–2.2 GeV as a function of the nuclear mass number, as shown in Figure 1.5. The mass number dependence was compared with theoretical calculations which describe propagation of η' mesons in nuclei. As a result, an absorption width of Γ =15–25 MeV at normal nuclear density was deduced for an average η' momentum of 1050 MeV/c.

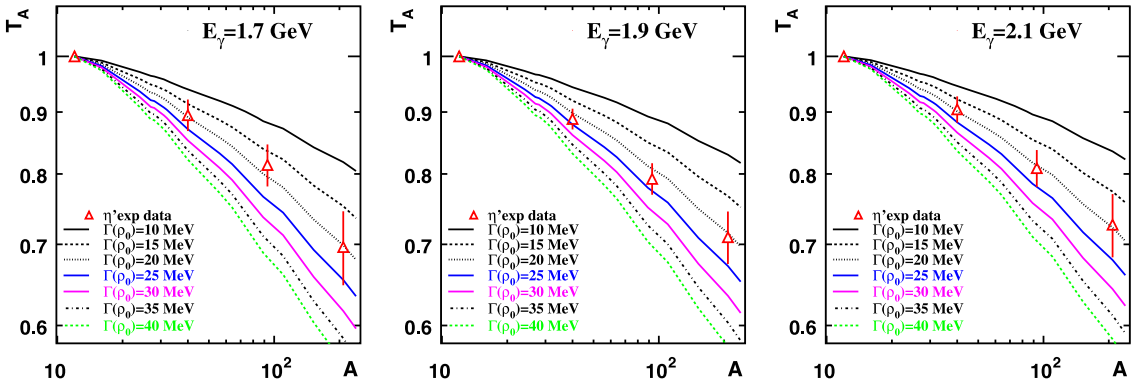

FIGURE 1.5: Transparency ratios in the photo-production of the η' meson measured by the CBELSA/TAPS collaboration. This figure is taken from Nanova *et al.* [20]

The deduced absorption width indicates the in-medium width of the η' meson is also as small as 15–25 MeV. This corresponds to $W_0 = -(7.5\text{–}12.5)$ MeV in terms of the imaginary part of the optical potential in Equation (1.2). Such a small in-medium width compared with a possible potential depth suggests possibility of an experimental observation of well-separated η' meson-nucleus bound states, as indicated in Figure 1.4.

Moreover, a real part of the potential was indirectly deduced from an excitation function and a momentum distribution of the η' mesons, which are shown in Figure 1.6 [21]. They compared these distributions with theoretical model calculations by Paryev [22], and estimated the real part of the potential to be $V_0 = -(37 \pm 10(stat.) \pm 10(syst.))$ MeV within the considered model.

COSY-11 experiment

The COSY-11 collaboration measured an excitation function of the $pp \to pp\eta'$ reaction near the η' production threshold [23–25], which is shown in Figure 1.7 as a function of the excess energy. From the evaluation of the final state interaction, they extracted the η'-proton scattering length as $\mathrm{Re}(a_{p\eta'}) = 0 \pm 0.43$ fm and $\mathrm{Im}(a_{p\eta'}) = 0.37^{+0.40}_{-0.16}$ fm. This small scattering length indicates that the real part of the potential is relatively small, which is estimated to be about $V_0 = 0 \pm 40$ MeV by a low density approximation.

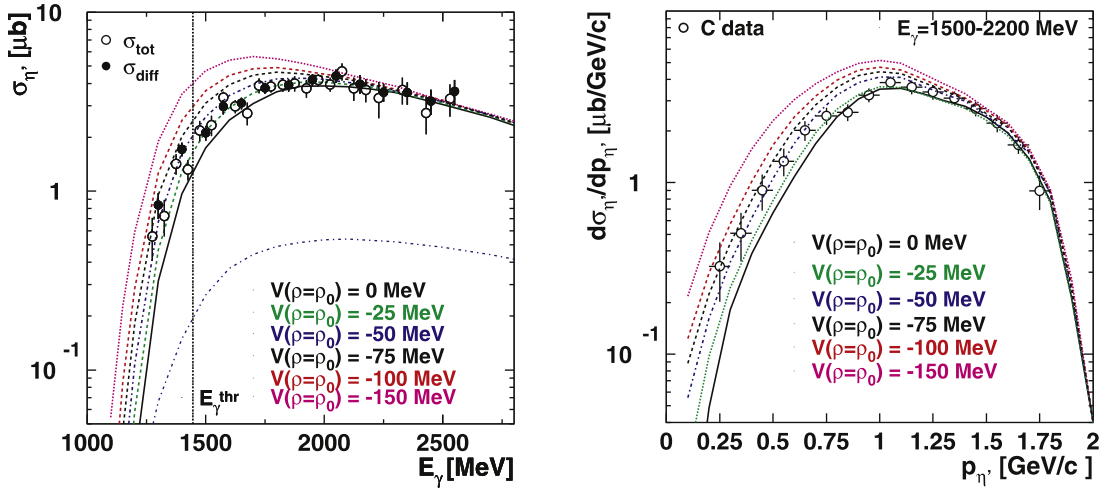

FIGURE 1.6: Total cross section and momentum distribution for the η' photo-production off ^{12}C. The lines show theoretical model calculations for different potential depths used for the comparison. This figure is taken from Nanova *et al.* [21]

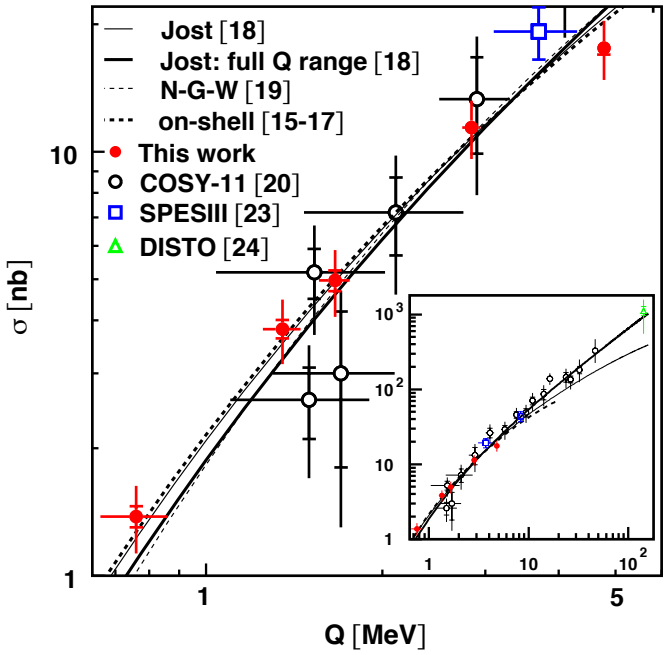

FIGURE 1.7: An excitation function of the $pp \to pp\eta'$ reaction measured by the COSY-11 collaboration. This figure is taken from Czerwiński *et al.* [23]

Heavy-ion collision at RHIC

While the two experiments explained above are suggesting a rather small potential depth or mass reduction, Csörgő *et al.* [26] reported an indirect observation of a strong mass reduction. They claimed an in-medium mass reduction by at least 200 MeV/c^2 is necessary to explain the two-pion Bose-Einstein correlation functions in the ultra-relativistic Au-Au collision experiments at RHIC.

As described in this section and in Section 1.2.1, in-medium properties of the η' meson are still not well understood both experimentally and theoretically. Therefore, an experimental investigation of η' meson-nucleus bound states is awaited in order to directly extract such information on the in-medium η' meson.

1.4 Thesis Objective

In this thesis, we present a first experimental search for η' mesic nuclei toward a direct study of in-medium properties of the η' meson. We performed a spectroscopy experiment of the ^{12}C(p,d) reaction at an incident proton energy of 2.5 GeV, and measured the missing-mass spectrum around the η' emission threshold. We aimed to achieve a high statistical sensitivity in the missing-mass spectrum so that η' mesic nuclei can be observed in case of a deep η'-nucleus potential of the order of 100 MeV as expected by the NJL model.

This thesis is organized as follows. First, we describe a principle and concept of the experiment in Chapter 2, and demonstrate the experimental feasibility based on a simulation. Next, the experimental method is explained in detail in Chapter 3. Then, in Chapter 4, we present the data analysis to obtain an excitation-energy spectrum of the ^{12}C(p,d) reaction. The obtained spectrum is statistically tested and compared with theoretically-calculated spectra for a discussion in Chapter 5. Finally, a conclusion is given in Chapter 6.

The author took a major role throughout the experiment, from the development stage to the main experiment and data analysis stage. The major contributions are listed as follows.

- Development of high-refractive-index aerogel Čerenkov detectors
- Updating the readout scheme of the multi-wire drift chambers
- Simulation of ion optics of the spectrometer system
- Hardware and software preparation of the data acquisition system
- Coding the online analysis program
- Planning detailed experimental procedures
- Performing the main measurements
- Data analysis described in this thesis

Chapter 2

Experimental Principle

We proposed a missing-mass spectroscopy experiment of the ^{12}C(p,d) reaction in order to investigate η' mesic nuclei [27, 28]. In this chapter, first, we explain the reaction and theoretical calculations for the formation of the η' mesic nuclei [4]. Next, our experimental concept is described as well as a feasibility study of the experiment.

2.1 ^{12}C(p,d) Reaction for Production of η' Mesic Nuclei

For production of η' mesic nuclei, we employ the ^{12}C(p,d)^{11}C$\otimes\eta'$ reaction, *i.e.*,

$$\text{proton (beam)} + {}^{12}\text{C (target)} \rightarrow \text{deuteron (ejectile)} + {}^{11}\text{C}\otimes\eta' \text{ (product)}, \tag{2.1}$$

at an incident proton kinetic energy of 2.5 GeV. In this reaction, one neutron in the target is picked up, and a deuteron is emitted in a forward direction. At the same time, an η' meson is created in the residual ^{11}C nucleus and forms a nuclear bound state coupling with the neutron hole state, as denoted by ^{11}C$\otimes\eta'$.

Momentum transfer of this reaction is shown in Figure 2.1 as a function of the incident proton kinetic energy. A recoil-free condition where the momentum transfer become zero is not satisfied at any kinetic energy in the ^{12}C(p,d)^{11}C$\otimes\eta'$ reaction. We adopt the proton kinetic energy of 2.5 GeV, slightly above the threshold for the elementary process, which is around 2.4 GeV. The momentum transfer at 2.5 GeV is about 400–500 MeV/c, depending on the excitation energy. Such large momentum transfer induces an η' meson with a higher angular momentum, leading to an enhancement of excited states near the η' emission threshold, as described in Section 2.2. Thus, in the first experiment, we aim to observe a narrow peak structure around the η' emission threshold.

From the experimental point of view, the (p,d) reaction is suited for two reasons. Firstly, a magnetic rigidity of the ejectile deuteron is 10% less than that of the primary beam due to the finite momentum transfer. This makes it possible to experimentally separate the deuteron from the primary proton beam by using a magnetic spectrometer. Secondly, in case of the (p,d) reaction, a high-intensity primary beam is available, compared to other reactions using secondary beams, such as the (γ,p) or (π^+,p) reaction. This is one advantage of using the (p,d) reaction, since a high statistical sensitivity is essential in this experiment, as we describe in Section 2.3.

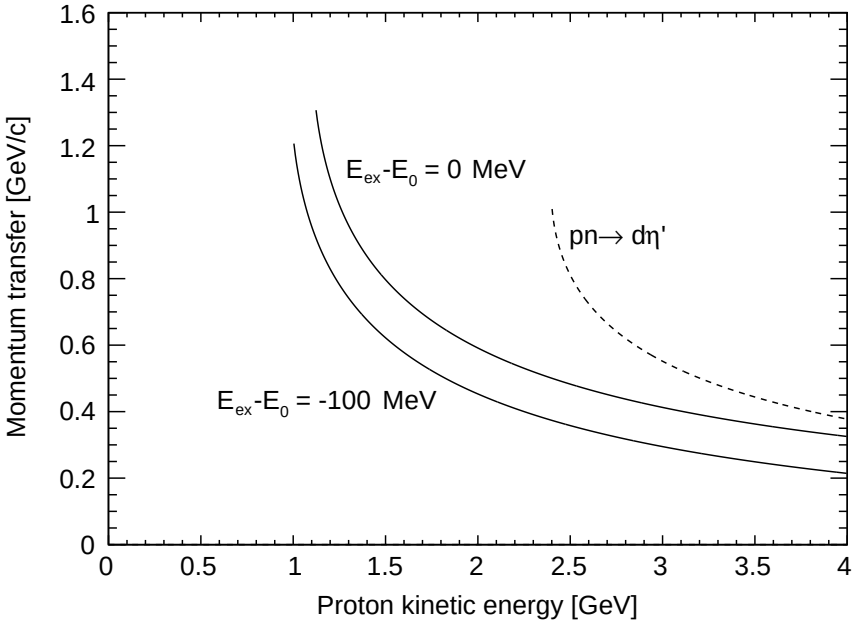

FIGURE 2.1: Incident-energy dependence of the momentum transfer is shown. The solid lines show the momentum transfer of the ^{12}C$(p,d)^{11}$C$\otimes\eta'$ reaction for excitation energies of 0 MeV and -100 MeV from the η' emission threshold. The dashed line shows the momentum transfer of the elementary process, $p + n \to d + \eta'$.

2.2 Theoretical Calculation of Formation Cross Section

Formation spectra of η' mesic nuclei in the ^{12}C$(p,d)^{11}$C$\otimes\eta'$ reaction are theoretically evaluated in Nagahiro *et al.* [4] by using the Green's function method [29, 30] for various cases of the η'-nucleus potential parameters. In this approach, the double-differential cross section is described by the elementary cross section of the $n(p,d)\eta'$ reaction and the nuclear response function $R(E)$ as

$$\left(\frac{\mathrm{d}^2\sigma}{\mathrm{d}\Omega \mathrm{d}E}\right)^{\mathrm{lab}}_{^{12}\mathrm{C}(p,d)^{11}\mathrm{C}\otimes\eta'} = \left(\frac{\mathrm{d}\sigma}{\mathrm{d}\Omega}\right)^{\mathrm{lab}}_{n(p,d)\eta'} \times R(E). \tag{2.2}$$

Since there are no experimental data of the elementary cross section of the $n(p,d)\eta'$ reaction, we estimate it to be ~ 30 μb/sr, as explained in Itahashi *et al.* [28] The nuclear response function $R(E)$ is theoretically calculated by evaluating the in-medium Green's function for the Klein-Gordon equation with the optical potential in Equation (1.2).

In the left panel of Figure 2.2, a calculated spectrum of the ^{12}C$(p,d)^{11}$C$\otimes\eta'$ reaction for $(V_0,W_0) = (-100, -10)$ MeV is shown as a function of the excitation energy E_{ex} around the η' emission threshold E_0. The thick solid line shows the total spectrum and the other lines show those of subcomponents. The η' mesic s, p, and d states are observed in the calculated spectrum. For each η' mesic state, there are two subcomponents coupled with two neutron hole states, $(0p_{3/2})^{-1}$ and $(0s_{1/2})^{-1}$, as seen in the figure. A contribution of the quasi-free η' production is also seen in the unbound region, $E_{\mathrm{ex}} - E_0 > 0$.

A calculated spectrum of the ^{40}Ca$(p,d)^{39}$Ca$\otimes\eta'$ reaction is shown for the same potential parameters, for a comparison, in the right panel of Figure 2.2. For such a heavier target, many bound states are expected, but also more neutron hole sates contribute to the

spectrum. As a result, the peaks overlap with each other and they are not well separated. This is the reason we adopt a lighter target of ^{12}C for the first experiment.

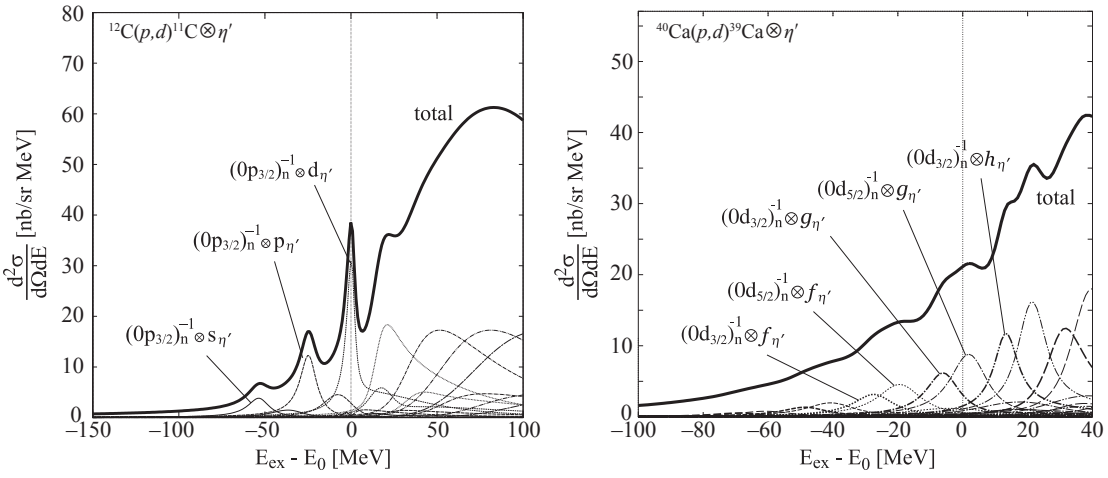

FIGURE 2.2: Calculated spectra for the ^{12}C(p,d)^{11}C⊗η' reaction (left) and the ^{40}Ca(p,d)^{39}Ca⊗η' reaction (right). Both of the spectra are calculated for the potential parameters of (V_0,W_0) = (−100, −10) MeV. These spectra are taken from Nagahiro *et al.* [4] and rearranged.

Figure 2.3 shows calculated spectra of the ^{12}C(p,d)^{11}C⊗η' reaction for various combinations of the potential parameters V_0 and W_0 [4]. Since the momentum transfer is relatively large about 400–500 MeV/c for the (p,d) reaction at the incident proton energy of 2.5 GeV, contributions of many components with higher angular momenta are seen in the spectra. Distinct peak structures of η' mesic bound states can be seen in the bound region $E_{ex} - E_0 < 0$, particularly in the cases of larger $|V_0|$ or smaller $|W_0|$. In addition to the bound states, relatively large peaks are expected also above the threshold. These are due to the so-called threshold enhancement, and, if observed, they can be interpreted as a signature of an attractive η'-nucleus potential.

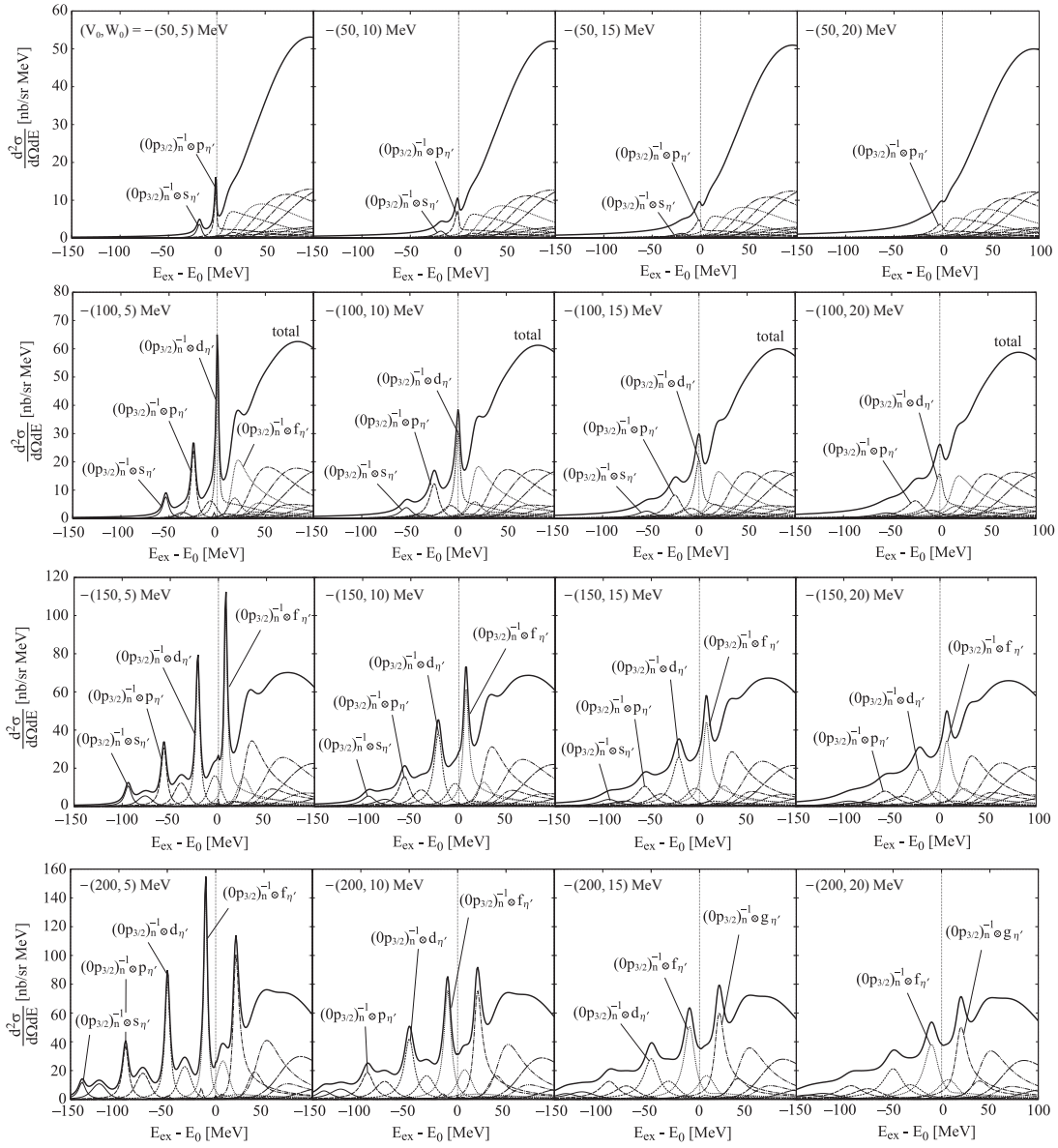

FIGURE 2.3: Calculated spectra of the ^{12}C(p,d)^{11}C$\otimes\eta'$ reaction at the incident proton energy of 2.5 GeV. The spectra are shown for the potential parameters of $V_0 = -50, -100, -150, -200$ MeV and $W_0 = -5, -10, -15, -20$ MeV. $E_{\rm ex} - E_0$ denotes the excitation energy from the η' emission threshold, which is shown by the vertical dotted line. The thick solid lines show the total spectra, while the others show contributions of the subcomponents. The neutron-hole states are labeled by $(nl)_n^{-1}$ and the η' mesic states by $l_{\eta'}$. These spectra are taken from Nagahiro *et al.* [4] and rearranged.

2.3 Experimental Concept

We employ missing-mass spectroscopy of the ^{12}C(p,d) reaction using a 2.5 GeV proton beam. In this reaction, while an η' mesic state is produced, a deuteron is emitted in a forward direction. Then we measure the momentum of the ejectile deuteron with a spectrometer system. The energy of the produced η' mesic nucleus can be calculated as a missing mass, by means of the energy and momentum conservation law. The relation between the deuteron momentum and the excitation energy from the η' production threshold is shown in Figure 2.4.

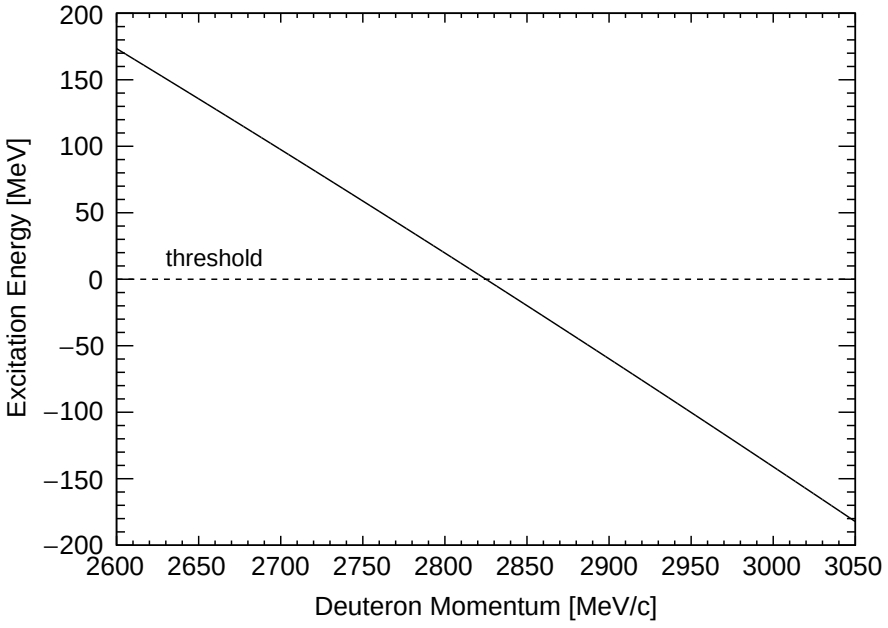

FIGURE 2.4: A relation between the excitation energy and the ejected deuteron momentum is shown for the ^{12}C(p,d) reaction at the proton energy of 2.5 GeV. The reaction angle is considered to be 0°. The dashed line corresponds to the η' emission threshold.

This type of experiment measuring only the ejectile particles is called *inclusive*, while that measuring decay particles is called *exclusive*. One advantage of this inclusive measurement over an exclusive measurement is the fact that no assumption on the decay processes is necessary. Since the inclusive spectrum is not distorted by the decay probabilities or their detection efficiencies, we can make an unbiased and straightforward interpretation of the spectrum.

However, a signal-to-noise ratio in the inclusive spectrum is very small due to a contamination of other physical background processes. In our kinematics, dominant background processes are expected to be the quasi-free processes such as

$$\text{proton (beam)} + \text{nucleon (in the target)} \rightarrow \text{deuteron (ejectile)} + \text{multi-pion}. \qquad (2.3)$$

The double differential cross section of the background processes around the momentum region of interest is estimated to be ~ 4 μb/(sr·MeV) [28]. This is about 100 times larger than the formation cross section of the η' mesic nuclei for most of the cases in Figure 2.3.

Thus, in order to overcome such a small signal-to-noise ratio, we aim to achieve a high statistical sensitivity by making use of an intense primary proton beam and a thick production target.

2.4 Expected Spectrum in Inclusive Measurement

Experimental feasibility of finding peak structures in the inclusive spectrum is discussed with a simulation. As a total cross section, both of the calculated formation cross section of the ^{12}C(p,d)^{11}C$\otimes\eta'$ reaction and the evaluated physical-background cross section [28] are combined in the simulation.

Simulated inclusive spectra are shown in Figure 2.5 for the potential parameters of $V_0 = -200, -150, -100$ MeV and $W_0 = -5, -10, -20$ MeV. Here, 3.24×10^{14} protons on a 4 g/cm^2-thick ^{12}C target are assumed, which correspond to a 4.5-day data-taking period in a realistic experimental setup. These simulation results show that peak structures near the η' emission threshold are observed even in the inclusive measurement, if the real part of the potential $|V_0|$ is as large as 150 MeV, as predicted by the NJL model [10, 11], and the imaginary part $|W_0|$ is as small as 10 MeV, as indicated by the CBELSA/TAPS experiment [20].

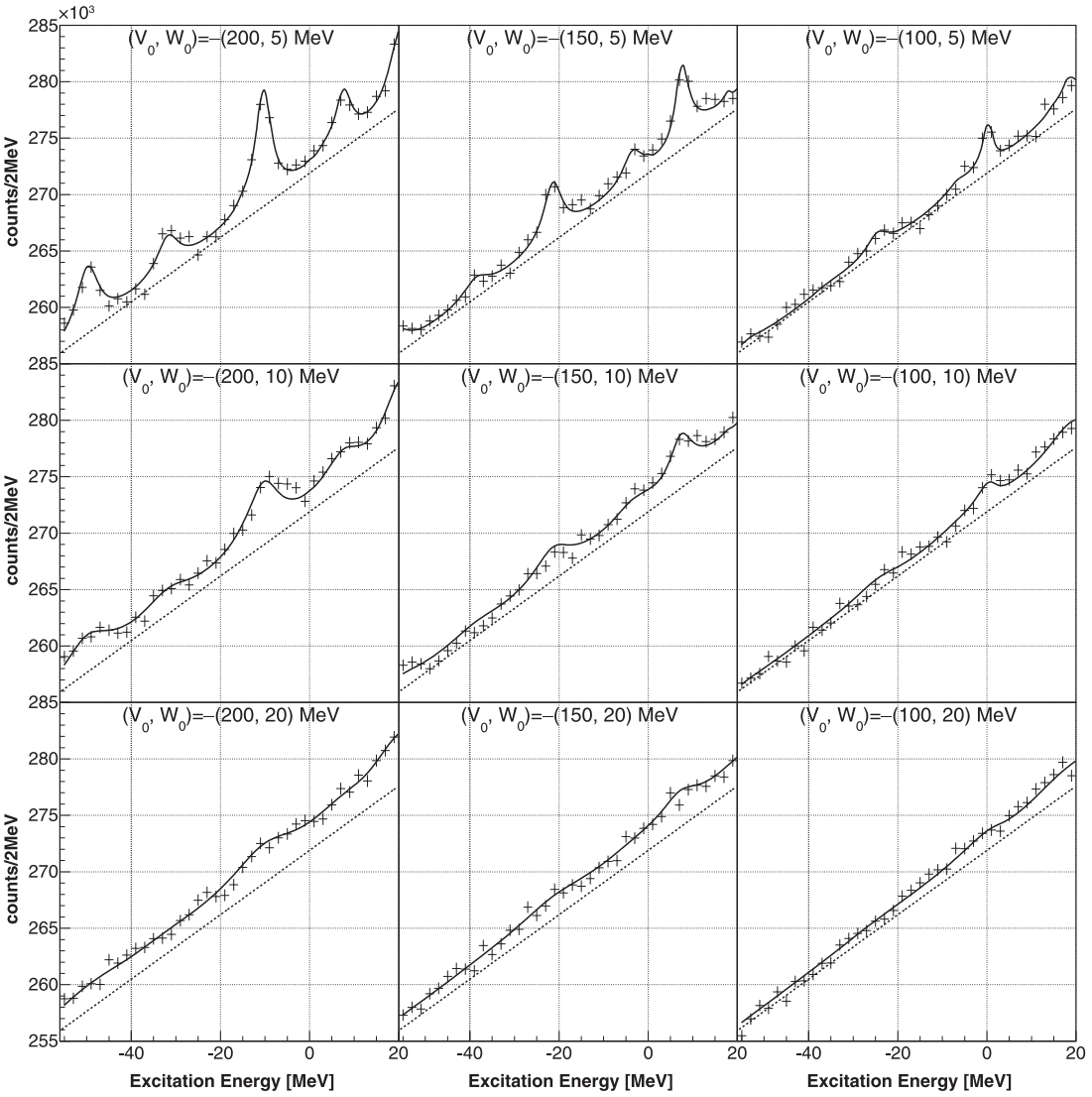

FIGURE 2.5: Simulated inclusive spectra of the ^{12}C(p,d) reaction around the η' emission threshold are shown for the potential parameters of $V_0 = -200, -150, -100$ MeV and $W_0 = -5, -10, -20$ MeV. The dashed lines correspond to the evaluated background cross section, and the solid lines are for the total cross section including both the signal and the background. The horizontal axis is the excitation energy from the η' emission threshold. In these simulations, 3.24×10^{14} protons on a 4 g/cm^2 carbon target are assumed. This figure is taken from Itahashi *et al.* [28]

Chapter 3

Experimental Method

We performed the missing-mass spectroscopy experiment of the ^{12}C(p,d) reaction to search for η' mesic nuclei for the first time. The experiment was carried out at GSI Helmholtz Center for Heavy Ion Research, located in Darmstadt, Germany. In this chapter, we describe in detail the experimental method, including the facilities, our detector system, and the performed measurements.

3.1 Experimental Facilities

The experimental facilities at GSI are schematically shown in Figure 3.1. A wide range of ions from hydrogen to uranium can be accelerated by the synchrotron SIS-18, in combination with the linear accelerator UNILAC. Beams are accelerated up to a maximum kinetic energy of 4.5 GeV for protons and 1–2 GeV/nucleon for heavy ions by the SIS-18. These beams are extracted and transferred to experimental areas such as the Fragment Separator (FRS), the Experimental Storage Ring (ESR), and the other downstream experimental halls.

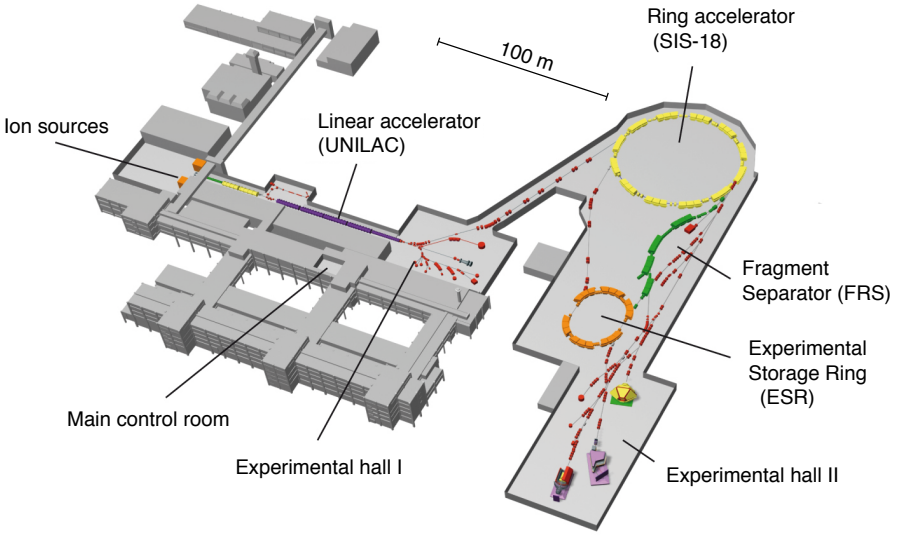

FIGURE 3.1: A schematic bird's-eye view of the GSI facilities. This figure is taken from a web page of GSI [31].

The FRS is a magnetic forward spectrometer designed as a projectile fragment separator [32]. Primary beams are injected to a production target at the entrance of the FRS, and

secondary beams of radioactive isotopes are produced at relativistic energies via projectile fragmentation. The produced isotopes can be separated in flight with a good resolution by the FRS. The separated isotopes can be studied at the final focal plane of the FRS, or can be injected into the downstream experimental areas such as the ESR.

We used the FRS as a high-resolution spectrometer to precisely measure the momenta of the deuterons ejected in the ^{12}C(p,d) reaction. As the FRS is designed as a fragment separator, it has large degree of freedom in the ion-optical setup. This leads to flexibility in the momentum resolution, momentum acceptance, and background rejection capability. Such an application of the FRS to the high-resolution spectroscopy was successfully demonstrated in the previous pionic-atom experiments [7, 33–38], where the deeply-bound pionic lead and tin atoms were discovered and studied with the (d,^{3}He) reaction.

3.2 Beam

We employed proton beams of two kinetic energies, 2.5 GeV and 1.6 GeV, supplied by the SIS-18. The 2.5 GeV beam was used for the production and reference measurements of the ^{12}C(p,d) and d(p,d) reactions around the η' emission threshold, while the 1.6 GeV beam was used to measure the d(p,d) elastic scattering for the calibration of the spectrometer. Conditions of the primary beams are summarized in Table 3.1.

The beams accelerated by the SIS-18 were extracted by a slow extraction and transported to the FRS target region. We adjusted spill lengths of the slow extraction at 4 seconds for the 2.5 GeV beam and 1 second for the 1.6 GeV beam in order to optimize an overall rate of data acquisition. As it took 3 seconds for acceleration of each spill, overall spill cycles were 7 seconds for 2.5 GeV and 4 seconds for 1.6 GeV.

The delivered beam was centered and focused at the target position of the FRS. This was achieved by tuning magnetic fields of two sets of quadrupole doublets and two dipole magnets in the beam transfer line from the SIS-18 to the FRS. Since a small spot size at the center of the target is important for a high-resolution momentum measurement, we frequently monitored the beam profile at the target position and confirmed the centering and focusing of the beam.

Typical beam intensities were of the order of 10^{10} protons per spill for both the energies. Such high intensity beams were very important to accumulate data with good statistics. We performed calibration measurements of intensity monitors for the 2.5 GeV proton beam to evaluate the beam intensity accurately. The detailed analysis of the beam intensity is described in Section 4.6.

Table 3.1: Conditions of the primary beams.

Energy	Spill cycle	Spill length	Intensity	Purpose
2.5 GeV	7 s	4 s	$\sim 10^{10}$ protons/spill	production, reference
1.6 GeV	4 s	1 s	$\sim 10^{10}$ protons/spill	calibration

3.3 Target

Targets used in the experiment are listed in Table 3.2. A carbon target with an areal density of 4115 mg/cm^2 was adopted for the main measurement of the ^{12}C(p,d) reaction. Deuterated polyethylene (CD_2) targets with areal densities of 4022 mg/cm^2 and 1027 mg/cm^2 were prepared as well. The thicker CD_2 target was used to measure the d(p,d) reaction

around the η' emission threshold, and the thinner CD_2 target was used for the spectrometer calibration with the proton-deuteron elastic scattering at 1.6 GeV, as explained in Sections 3.7.2 and 3.7.3, respectively.

The targets were installed on a target ladder of the FRS. The ladder is made of 2 cm-thick copper equipped with 75 cylindrical holes with each radius of 1 cm. All of the targets used in this experiment were cylindrical shape, and they are mounted inside the holes of the target ladder. One of the holes of the ladder has no material attached, which is listed as empty target. The empty target was used to evaluate instrumental background due to possible reactions between a halo structure of the beam and the target ladder.

TABLE 3.2: A list of the targets used in the experiment.

Material	Thickness	Areal density	Reaction
C	22.196 ± 0.006 mm	4115 ± 1 mg/cm^2	^{12}C(p,d) reaction
CD_2	36.868 ± 0.085 mm	4022 ± 9 mg/cm^2	d(p,d) reaction
CD_2	9.332 ± 0.016 mm	1027 ± 2 mg/cm^2	d(p,d) reaction
empty	–	–	–

3.4 Fragment Separator

The FRS is a magnetic spectrometer consisting of four stages of separators. Its configuration is expressed as

(TA)–QQQSDSQQ–(F1)–QQSDSQQQ–(F2)–QQQSDSQQ–(F3)–QQSDSQQQ–(F4),

where D, Q, and S stand for a dipole magnet, a quadrupole magnet, and a sextupole magnet, respectively. TA and F1–F4 denote the target area and the first to the final focal planes. Each stage consists of one dipole magnet with a bending angle of 30 degrees, quadrupole doublets and triplets around the dipole magnet, and two sextupole magnets at the entrance and the exit of the dipole magnet. A schematic configuration is shown in the top panel of Figure 3.2.

There are two requirements for ion optics in this experiment. First, we need an achromatic focal plane at F2 and a dispersive focal plane at F4 unlike the standard optics modes of the FRS. Since the momentum difference between the primary beam and the signal deuteron is only about 10%, the high-energy proton beam is dumped around the exit of the first dipole magnet (D1) and possibly produces secondary background. Such secondary particles can be rejected at the achromatic focal plane using a small size scintillator as an active slit. Then, the momentum of the signal deuteron is analyzed with the trajectory at the dispersive focal plane F4. The second requirement is to keep small dispersion throughout the FRS. This is necessary to obtain a wide momentum acceptance and hence cover a wide missing-mass region.

We developed a new ion-optics mode fulfilling the above requirements with a GICOSY program [39]. The GICOSY is a simulation tool to calculate ion-optical systems based on transfer matrices up to the fifth order terms. The designed optics mode is schematically shown in the second and third top panels of Figure 3.2. Beam trajectories are plotted with initial positions and angles of −1.5, 0, 1.5 mm and −8, −4, 0, 4, 8 mrad for the horizontal direction, and −1.5, 0, 1.5 mm and −12, −6, 0, 6, 12 mrad for the vertical direction. Initial momentum deviations are taken to be −1, 0, and 1% in the figure. The achromatic focus at F2 and the dispersive focus at F4 are achieved as seen in the horizontal beam trajectories.

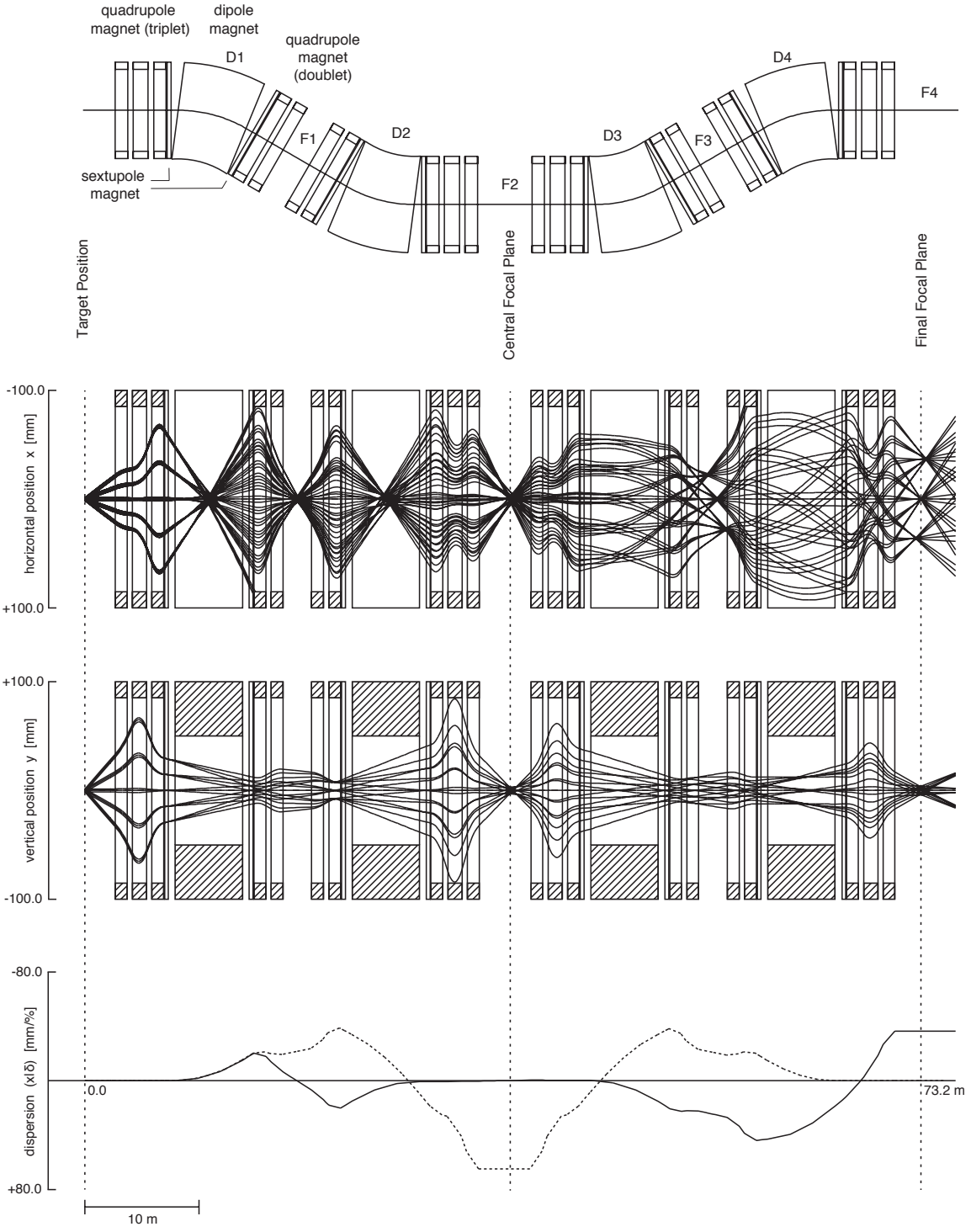

FIGURE 3.2: Designed new optics of the FRS calculated by GICOSY. A schematic configuration of the FRS magnets is shown (top). Calculated beam trajectories are plotted for the horizontal direction (second top) and the vertical direction (third top). The trajectories are plotted for initial positions of $x_{\mathrm{TA}}, y_{\mathrm{TA}} = -1.5$, 0, 1.5 mm, initial angles of $a_{\mathrm{TA}} = -8$, -4, 0, 4, 8 mrad and $b_{\mathrm{TA}} = -12$, -6, 0, 6, 12 mrad, and relative momentum deviations of $\delta = -1$, 0, 1%. Dispersion lines are plotted along the beam line for the new mode by the solid line and for the standard mode by the dashed line, respectively (bottom). Note that the direction of the beam axis is shown in a different scale from the horizontal and vertical directions.

The bottom panel of Figure 3.2 shows dispersion lines. Dispersion values from the target position are plotted along the beam axis for this newly-developed optics (solid line) and the standard FRS optics (dotted line). The dispersion is kept below $\sim$ 4 cm/% for the developed mode, while the maximum dispersion in the standard mode is about 6.5 cm/%.

The first-order transfer matrix from the target position to the dispersive focal plane F4 calculated with the GICOSY program is

$$\begin{pmatrix} (x|x) & (x|a) & (x|y) & (x|b) & (x|\delta) \\ (a|x) & (a|a) & (a|y) & (a|b) & (a|\delta) \\ (y|x) & (y|a) & (y|y) & (y|b) & (y|\delta) \\ (b|x) & (b|a) & (b|y) & (b|b) & (b|\delta) \end{pmatrix}_{\mathrm{TA}\to\mathrm{F4}} = \begin{pmatrix} 0.48 & 0.0 & 0.0 & 0.0 & -36.4 \\ 0.88 & 2.07 & 0.0 & 0.0 & 0.0 \\ 0.0 & 0.0 & -0.04 & -0.33 & 0.0 \\ 0.0 & 0.0 & 3.02 & -0.01 & 0.0 \end{pmatrix}, \quad (3.1)$$

where x and y denote the horizontal and vertical positions, a and b do the horizontal and vertical angles. δ is a relative momentum deviation expressed as $\delta = P/P_{\mathrm{center}} - 1$ with the momentum P and the central momentum of the spectrometer P_{center}. Units used in Equation (3.1) are mm for x and y, mrad for a and b, and % for δ. In this thesis, we adopt a left-handed coordinate system for convenience of detector analysis. Thus, the output of the GICOSY program, which is in a right-handed coordinate, is reversed for the horizontal direction.

The momentum resolving power R of the designed optics is

$$R = \left| \frac{(x|\delta)}{2(x|x)\Delta x_{\mathrm{TA}}} \right| = 3.8 \times 10^3, \quad (3.2)$$

assuming a spot size at the target Δx_{TA} of 1 mm. This contributes to the missing-mass resolution by only about 0.6 MeV/c^2, which is sufficiently smaller than the expected natural widths of the η' mesic nuclei.

We performed measurements at several central momenta of the FRS in order to cover a wide spectral region. We scaled all the magnetic fields by factors between 0.98 and 1.02, and investigated the excitation-energy region from roughly -90 MeV to $+30$ MeV from the η' emission threshold. The relation between the scale factor of the FRS and the excitation-energy range is given in Figure 3.3. These measurements with the several scale factors are also important when a structure is observed in a spectrum. If an observed structure shifts according to the change of the scale factors, it can be safely attributed to a physical structure. The details of the measurement conditions are explained in Section 3.7.

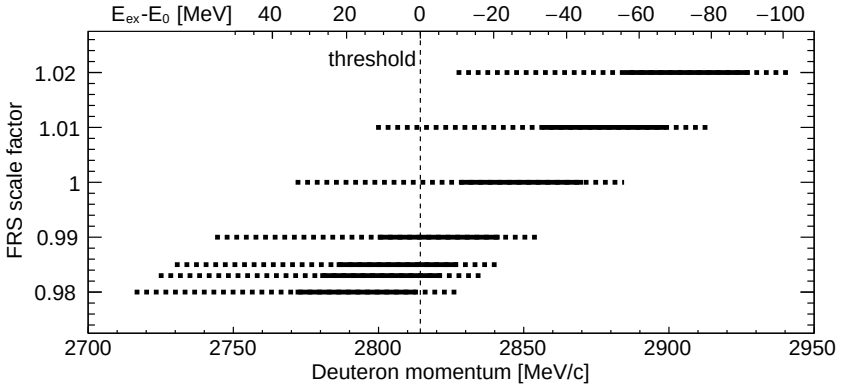

FIGURE 3.3: The relation between the FRS scale factor and the range of the excitation energy from the threshold, $E_{\mathrm{ex}} - E_0$, is shown. The thick solid lines show linear-acceptance regions used for the spectrum analysis in Section 4.9, while the thick dashed lines include also low-acceptance regions. The thin dashed line indicates the η' emission threshold.

3.5 Detector System

3.5.1 Overview of detector setup

An overview of the experimental setup at the FRS is shown in Figure 3.4. The reaction targets were installed at the FRS target region together with beam monitors. The proton beam extracted from the SIS-18 impinged onto the target to produce η' mesic nuclei with the (p,d) reaction. The ejected deuterons were detected at the downstream focal planes, F2 and F4.

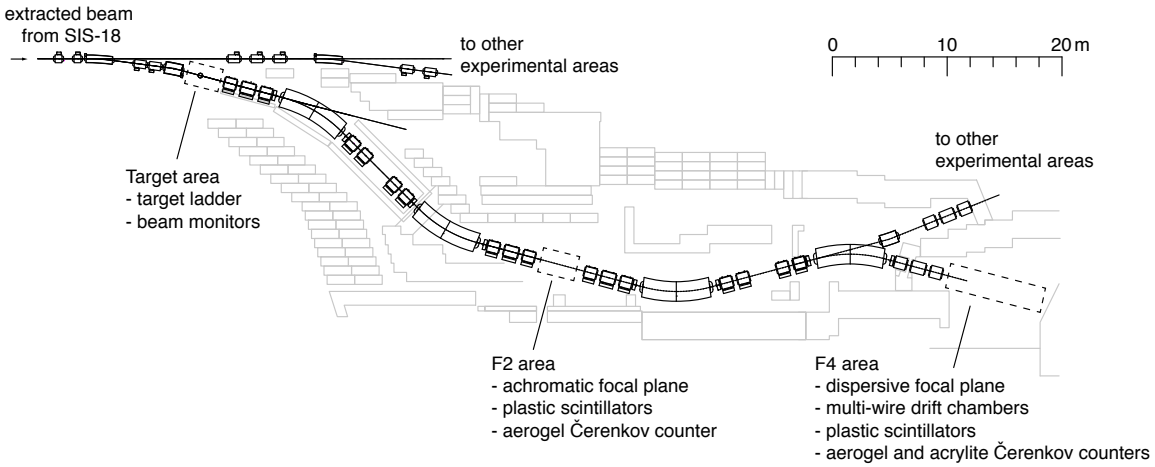

FIGURE 3.4: An overview of the experimental setup at the FRS. Components at each area are listed. Configurations of beam lines, magnets, and shielding blocks are shown as well.

The momenta of the ejected deuterons were measured at the F4 dispersive focal plane. We installed two sets of multi-wire drift chambers (MWDC's) as tracking detectors. Then the deuteron momenta can be deduced from the reconstructed track projected onto the focal plane.

Since large amount of protons produced by the (p,p') inelastic scattering reached the F4 focal plane as an experimental background, the particle identification was necessary. This identification was based on the velocity difference between the deuterons and the background protons in the momentum region of interest. For this purpose, we measured a time of flight (TOF) between F2 and F4 using scintillation counters installed at these focal planes. Furthermore, high-refractive-index aerogel Čerenkov detectors and a total-reflection Čerenkov detector were employed for on-line identification of the deuteron and tuning of a hardware trigger condition.

Detailed detector configurations at the target area and the F2 and F4 regions are explained in Sections 3.5.2–3.5.4.

3.5.2 Experimental setup at the target region

An experimental setup at the FRS target region is shown in Figure 3.5. A target ladder, horizontal and vertical slits, and standard beam-diagnostics devices (SEETRAM, CG1, CG2, and SC01) were installed in the vacuum chamber. These components can be moved by remote control. Two plastic scintillators SC00 and SC02 were additionally attached on the chamber. The positions of these scintillators are indicated in Figure 3.5.

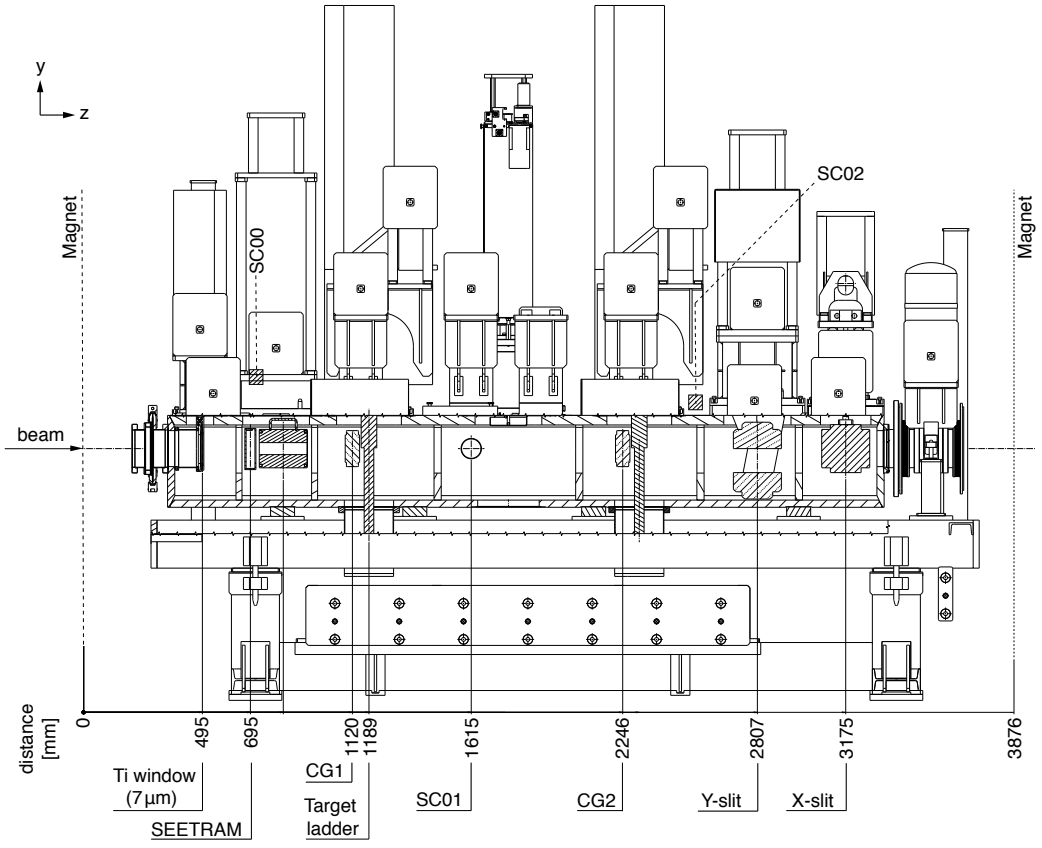

FIGURE 3.5: An experimental setup at the FRS target area.

SEETRAM

SEETRAM is a secondary-electron transmission monitor, which is aiming to monitor a beam intensity [40]. Three thin titanium foils of 10 μm thickness are inserted on the beam axis, and secondary electrons emitted from the foils are collected as an electric current. The current is converted into logic pulses by a current digitizer, which outputs logic pulses with a rate proportional to the input current. The logic pulses are counted and recorded by a VME scaler module.

In our experiment, SEETRAM was only used for intensity calibration and beam tuning. During the main measurements, SEETRAM was moved out from the beam axis in order to reduce unnecessary material on the beam axis.

Current Grids

Current Grids (CG1 and CG2) are detectors for measuring a spatial distribution of a primary beam [41]. P10 gas (mixture of 90% argon and 10% methane) is filled inside the detectors, and ionized electrons are gas-amplified and read out as a current. The beam profile can be obtained with a resolution of 1 mm.

We frequently used CG1 and CG2 in order to monitor the focusing and centering of the primary beam on the target position. These devices were placed off the beam axis during the data acquisition.

Plastic scintillators

Three plastic scintillators (SC00, SC01, and SC02) were used to monitor the beam intensity during the main measurements by counting the scattered particles off the target. SC00 and SC02 were attached on the vacuum chamber, and SC01 was set inside a pocket of the chamber. The signals from the photomultipliers attached to these scintillators were converted into logic pulses by a NIM discriminator module, and counted by a VME scaler.

Slit

Horizontal (X) and vertical (Y) slits were installed downstream of the target position. We used these slits in a measurement of the proton-deuteron elastic scattering at 2.5 GeV to limit the reaction angle and confirm an analysis method for a differential cross section.

3.5.3 Detector setup at the achromatic focal plane

Figure 3.6 shows an experimental setup at the F2 area. A vacuum chamber for FRS standard devices was placed in the first half of this area. Additionally, two plastic scintillators (SC2H and SC2V), a high-refractive-index aerogel Čerenkov detector (mini-HIRAC), and two TPCs (TPC23, TPC24) were installed in air in the second half of this region. These TPCs are standard position detectors of the FRS [42], and we used them for on-line tuning of the beam in this experiment. SC2H, SC2V, and mini-HIRAC are explained in more detail.

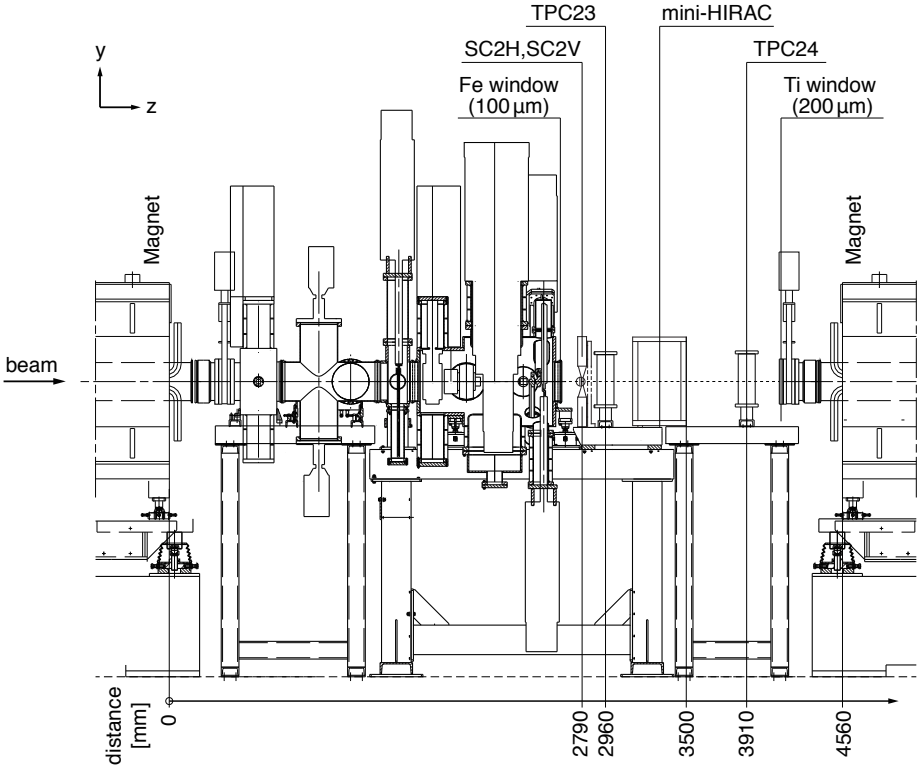

FIGURE 3.6: An experimental setup around the F2 focal plane.

SC2H and SC2V

Two plastic scintillators, SC2H and SC2V, were installed at the F2 achromatic focal plane. Small scintillators were adopted in order to select particles originating from the target position. The timing information obtained by these scintillators was used as a start time of the TOF between F2 and F4.

Schematic drawings of these scintillators are shown in Figure 3.7. ELJEN EJ-230 scintillators with an active areas of 60 mm × 60 mm were used, and produced scintillation lights were detected by the attached photomultipliers (Hamamatsu, H7195MODB). The applied voltages to the cathodes of the photomultipliers are listed in Table 3.3.

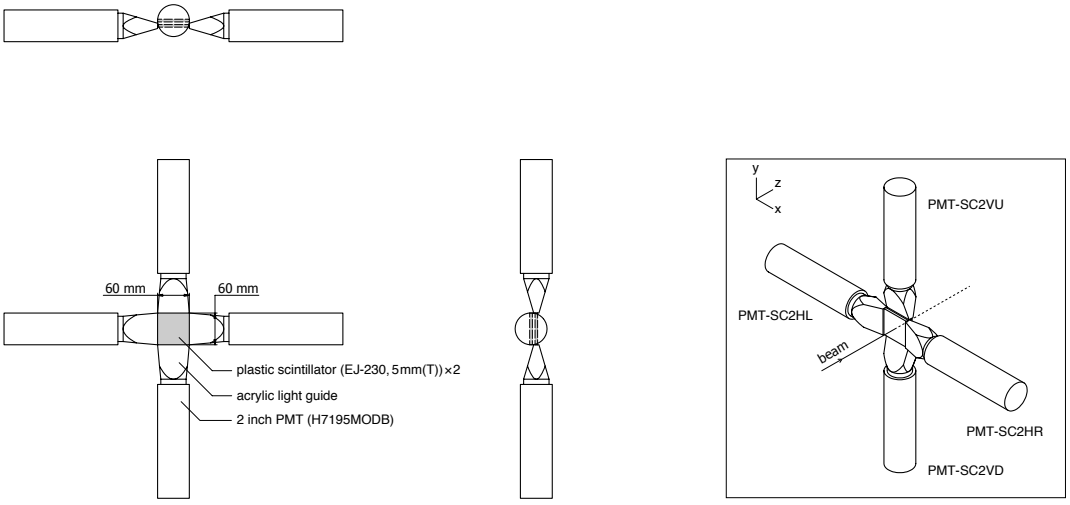

FIGURE 3.7: Schematic drawings of SC2H and SC2V. The attached photomultipliers were labeled as shown in the 3D view.

TABLE 3.3: A list of high voltages applied to the photomultipliers of SC2H and SC2V.

PMT Name	Voltage
PMT-SC2HL (left)	−1500 V
PMT-SC2HR (right)	−1450 V
PMT-SC2VU (top)	−1650 V
PMT-SC2VD (bottom)	−1600 V

mini-HIRAC

A small aerogel Čerenkov detector (mini-HIRAC) was installed for tuning of the particle identification. Silica aerogel with a high refractive index of about 1.17 [43] were used as a radiator. This index corresponds to the Čerenkov threshold velocity of $0.85 \times c$, which is slightly higher than the deuteron velocity. Emitted Čerenkov photons were reflected by a diffuse reflector plate[1] and detected by the two photomultipliers attached on the top and the bottom of the reflector box.

[1] Diffuse reflection was adopted in order to reduce an incident-position dependence of the detection efficiency. The white reflectance coating 6080 of Labsphere Inc. was used for a reflector.

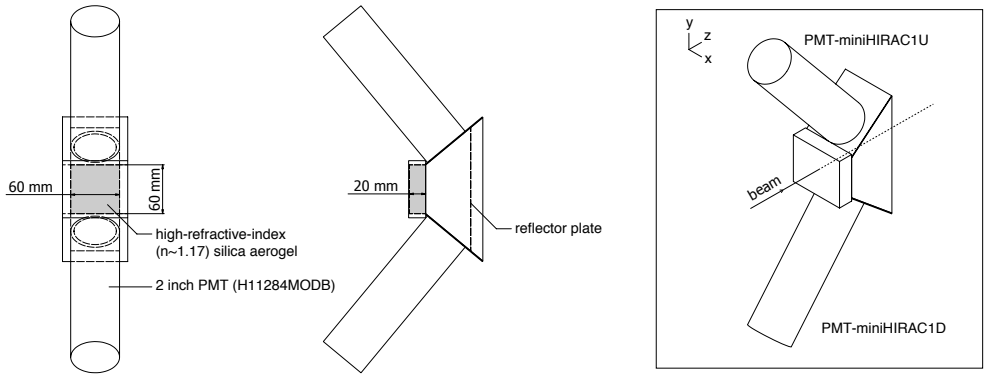

FIGURE 3.8: A schematic drawing of mini-HIRAC. The silica aerogel radiator is shown by the shaded region.

3.5.4 Detector setup at the dispersive focal plane

An experimental setup at the F4 focal plane is schematically shown in Figure 3.9. The focal plane was set around 2300 mm downstream from the last quadrupole magnet. Two sets of multi-wire drift chambers (MWDCs) were installed near the focal plane for the track reconstruction. The FRS-standard TPCs were placed as well for on-line monitoring of the beam profiles. Two scintillation counters (SC41 and SC42) and two Čerenkov counters (HIRAC and TORCH) were installed downstream of the tracking detectors.

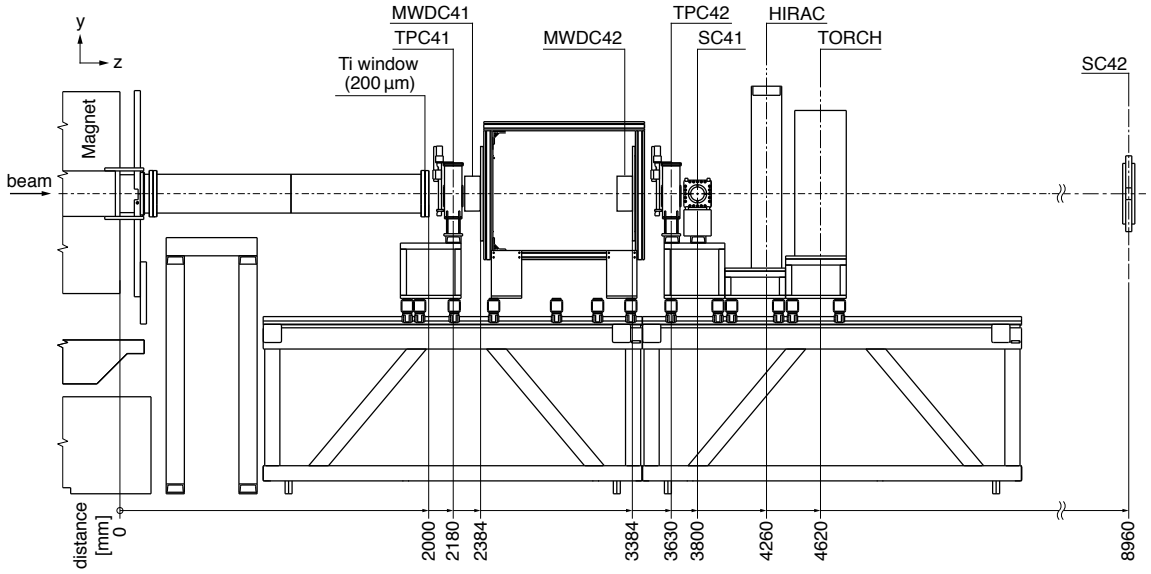

FIGURE 3.9: An experimental setup at the F4 area.

MWDC

Two sets of multi-wire drift chambers (MWDCs) were installed for the track reconstruction. The structure of the MWDC is shown in Figure 3.10. The active region is 240 mm in the horizontal direction and 140 mm in the vertical direction. Each drift chamber consists of eight wire planes, X1, X'1, X2, X'2, U, U', V, and V' planes, each of which has 48 sense wires with a pitch of 5 mm. The planes with the prime marks have patterns shifted by

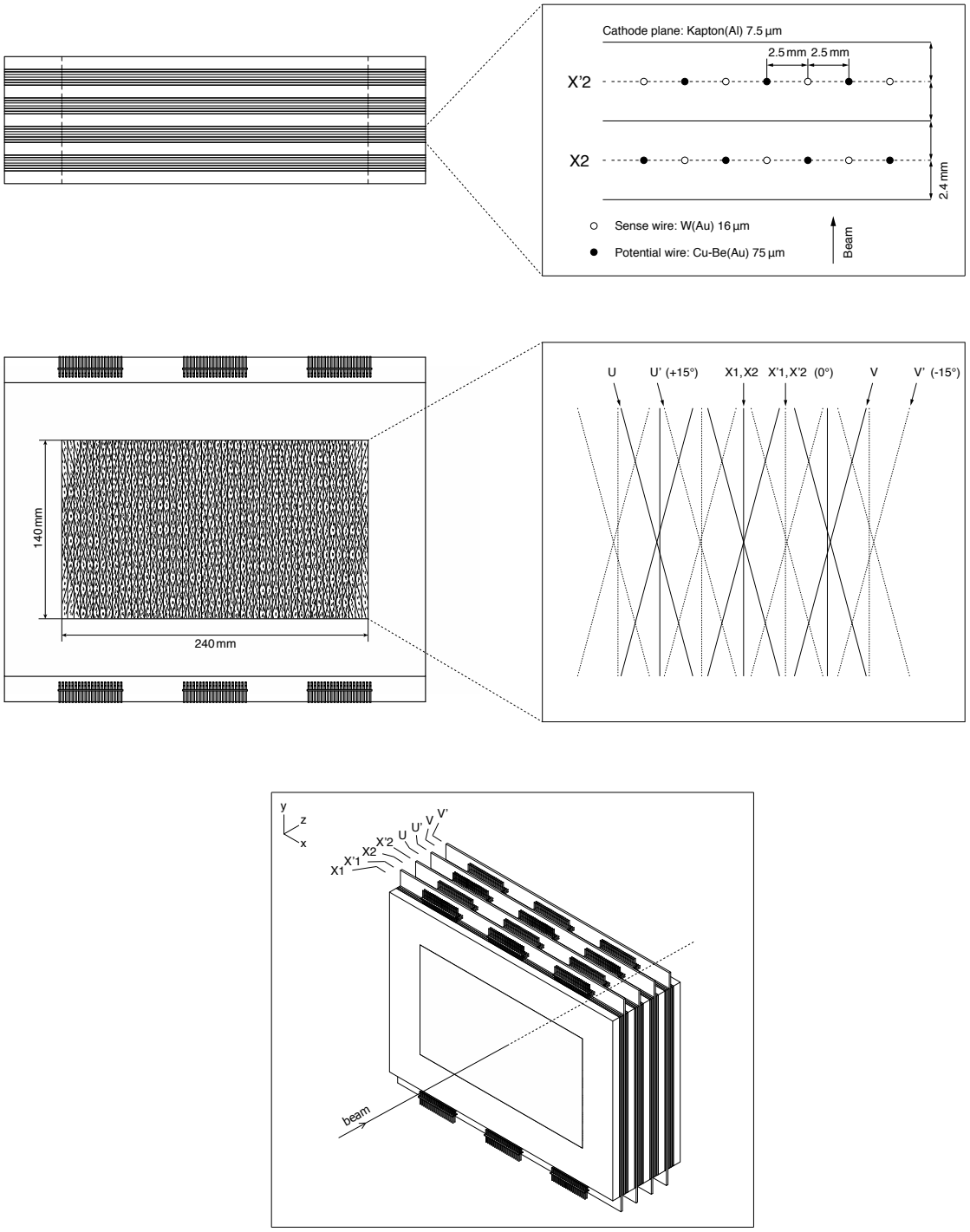

FIGURE 3.10: A schematic drawing of MWDC. A top view is shown with an enlarged configuration of the wires and the cathode planes (top). A front view is shown with the directions of the X, U, V type wires (middle). A simplified three dimensional view is shown (bottom).

half cell compared to those planes without the prime marks, as illustrated in the top panel of Figure 3.10. These paired planes allow us to determine hit positions in these planes. Directions of the wires in the X-type, U-type, and V-type planes are 0, −15, and +15 degrees from the vertical axis, respectively. These configurations were adopted in order to obtain a better sensitivity in the horizontal direction, because momenta of the particles are deduced by their horizontal tracks.

The MWDCs were operated with a gas mixture of 76% argon, 20% isobutane, and 4% methylal (dimethoxymethane). The mixed gas was continuously introduced at a slow flow rate about 50 mL/min. Applied voltages to the cathode planes and the potential wires were −1450 V and −1500 V, respectively[2]. A voltage of the sense wires was kept at the ground level. Then with the created electric fields, ionized electrons were drifted, gas-amplified, and collected by the sense wires.

Signals from the sense wires were read out and digitized by amplifier-shaper-discriminator (ASD) modules. In these modules, ASD chips described in Orito *et al.* [44] were employed. Amplified and discriminated signals were output as the low-voltage differential signaling (LVDS). A leading edge and a falling edge of the output signals were recorded by VME time-to-digital convertors (TDC).

SC41 and SC42

Two plastic scintillators, SC41 and SC42, were installed for timing measurements. Figure 3.11 shows schematic drawings of these scintillators. ELJEN EJ-230 and EJ-200 were used as scintillators for SC41 and SC42, respectively. Active areas are shown by the shaded regions in Figure 3.11. Since SC42 was placed about 7 m downstream of the focal plane, the larger scintillator was adopted. Scintillation lights were guided to 2-inch photomultipliers (Hamamatsu, H7195MODB) attached on both the left and right sides. The applied voltages to the cathodes of these photomultipliers are listed in Table 3.4.

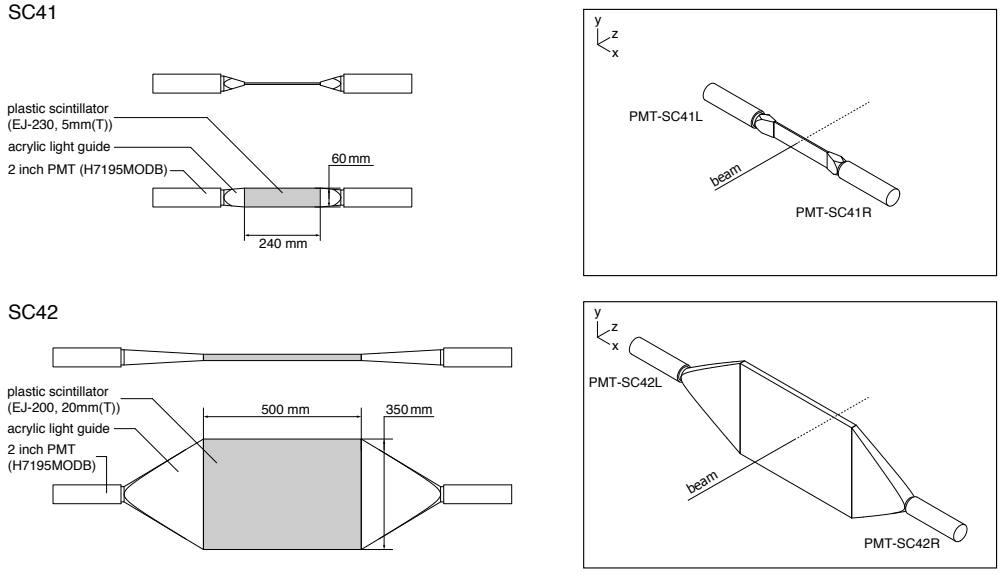

FIGURE 3.11: Schematic drawings of SC41 and SC42 at the F4 focal plane.

[2] For a short time, −1450 V and −1400 V were applied. These data sets were separately treated in an analysis for calibration parameters of the MWDCs.

TABLE 3.4: A list of high voltages applied to the photomultipliers of SC41 and SC42.

PMT Name	Voltage
PMT-SC41L (left)	−1380 V
PMT-SC41R (right)	−1420 V
PMT-SC42L (left)	−1240 V
PMT-SC42R (right)	−1210 V

HIRAC

HIRAC is a high-refractive-index aerogel Čerenkov detector which has a similar structure to mini-HIRAC. Figure 3.12 shows a schematic drawing of HIRAC. We used the high-refractive-index ($n \sim 1.17$) silica aerogel for the radiator. Since HIRAC was placed at the dispersive focal plane, the radiator with the active area of 270 mm × 90 mm was adopted. Produced Čerenkov photons were reflected by the diffuse reflector, and detected by the eight photomultipliers attached on the reflector box.

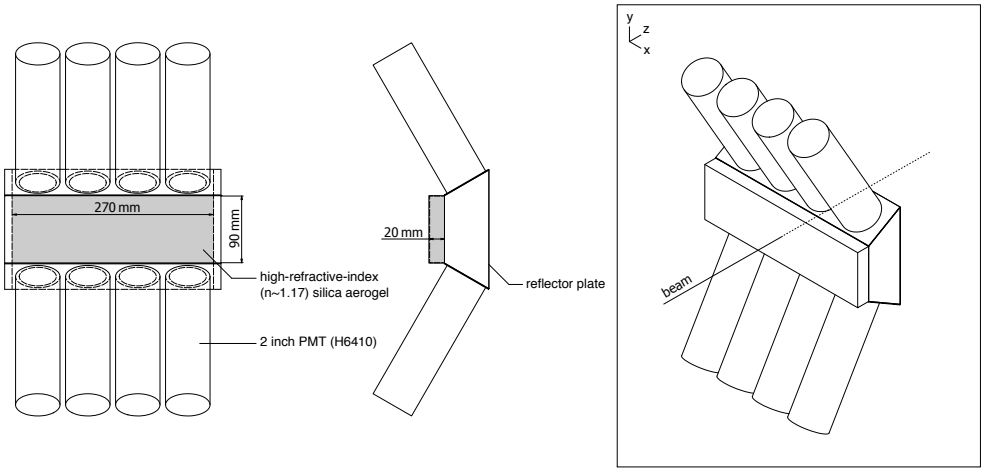

FIGURE 3.12: A schematic drawing of HIRAC at the F4 focal plane is shown.

TORCH

TORCH is a total-reflection Čerenkov detector which has an Acrylite radiator with a refractive index of about 1.5 [45]. This detector has two threshold velocities: the Čerenkov threshold ($\sim 0.67 \times c$) and the total-reflection threshold ($\sim 0.89 \times c$), and only particles with a velocity between these thresholds are detected. Thus, unlike the aerogel detectors, TORCH is only sensitive for the signal deuterons.

3.6 Data Acquisition System

A data acquisition system (DAQ) was constructed with a GSI-standard MBS system [46]. Electronics modules distributed in four VME crates were synchronously controlled. VME scalers, charge-to-digital converters (QDCs), time-to-digital converters (TDCs), and a waveform digitizer were employed to record the signals of the detectors. Table 3.5 summarizes the VME modules used in this experiment.

TABLE 3.5: A list of the used VME modules.

Module type	Module name
Scaler	CAEN-V830
TDC	AMSC-AMT-TDC
TDC	CAEN-V1290
QDC	CAEN-V792
Waveform digitizer	CAEN-V1742

Signals from the detectors were recorded as follows. Firstly, signals from the photomultipliers of the scintillators and the Čerenkov counters were divided into digital and analog branches. Timing information of the digital signals by NIM discriminators was recorded by the CAEN-V1290 TDCs, and charges of the analog pulses were recorded by the CAEN-V792 QDCs. In addition, the analog signals of SC2H, SC2V, SC41, and SC42 were also measured by the waveform digitizer, which sampled the waveforms with a rate of 1 GHz [3]. Secondly, rising and falling times of the MWDC signals were recorded by the AMSC-AMT-TDCs. Moreover, signals of the intensity monitors and the scintillators were counted by the VME scalers.

The DAQ system was triggered by a TOF-based coincidence of the SC2H and SC41 signals. A schematic trigger circuit is shown in Figure 3.13. We adjusted the delay lengths for the inputs to the TOF-based coincidence so that the coincidence of SC2H and SC41 was taken only for deuteron events. Figure 3.14 shows timing diagrams for four cases including accidental double hits. Since the TOF between F2 and F4 of the proton is 20 ns shorter than that of the signal deuteron, the background proton can be clearly rejected for the single-hit case (b) in Figure 3.14. We also need to consider the accidental double-proton cases, (c) and (d), because the proton rate was about 10^6/spill and was about 200 times higher than that of the deuterons. When there were two protons within a short time, only the first hit was taken by the mean timer in this circuit[4]. Thus, the case (c) in Figure 3.14 was rejected, but the case (d) was accepted by this trigger circuit.

A typical rate of the requested trigger was about 1×10^4/spill with an intensity of the primary beam about 4–5$\times 10^{10}$/spill in the measurement of the ^{12}C(p,d) reaction. A computer-busy time of this DAQ system was about 0.4 ms per event, which corresponds to the maximum DAQ rate of 2.5 kHz. However, due to a micro-structure of the beam, only about 3–4$\times 10^3$ triggers were typically accepted per 4-second spill.

[3] The maximum sampling rate of V1742 is 5 GHz. We reduced the rate to make a data size smaller.

[4] This was because the first discriminators in front of the mean timers had longer output widths of 30–40 ns, and the second discriminators had widths of about 10 ns.

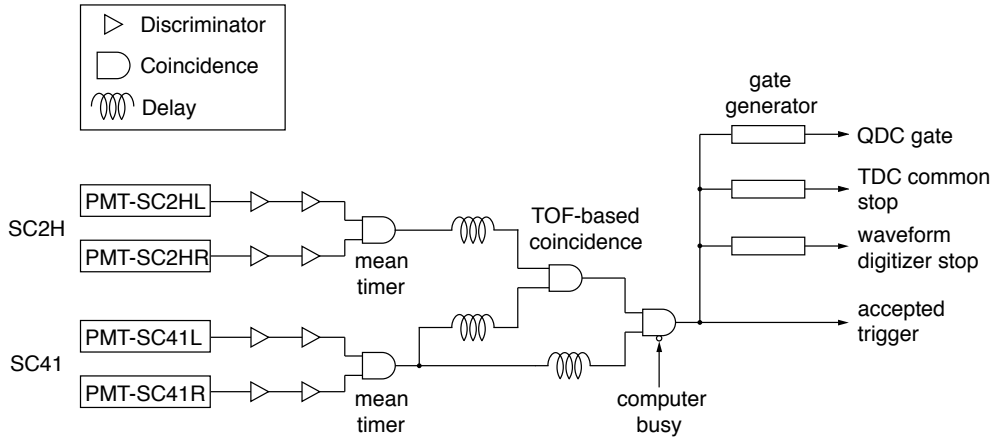

FIGURE 3.13: A diagram of the trigger circuit is shown.

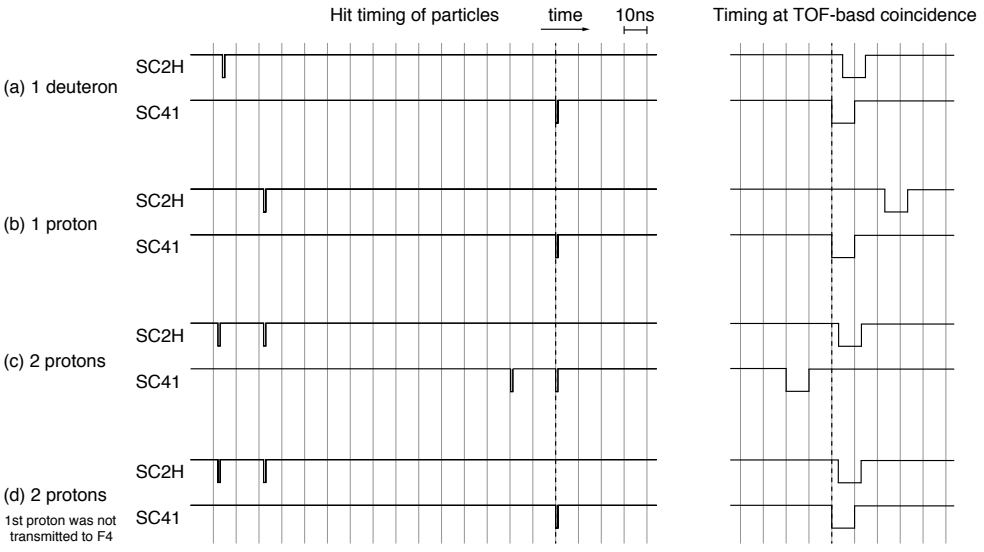

FIGURE 3.14: Timing diagrams of the TOF-based trigger are shown for four cases: single deuteron (a), single proton (b), accidental two protons (c), and accidental two protons in which the first proton was not transmitted to F4 (d). The left-hand side shows hit timing, and the right-hand side shows timing at the input of TOF-based coincidence. The cases (b) and (c) were rejected, but the case (d) made a contamination in the recorded data.

3.7 Summary of Measurements

Measurements performed during the first experiment in August 2014 are summarized in this section.

3.7.1 Production measurement

We performed the production measurements of the ^{12}C(p,d) reaction with several scale factors for the central momentum of the FRS in order to cover a wide momentum range. Table 3.6 lists the adopted scale factors with their dataset names, momentum ranges, and durations of the measurements. The momentum regions around the η' emission threshold were intensively measured. The measurements at the scaling factor of 1.000 were divided into two data sets, because the focus position at F4 was slightly shifted between them, and they were separately treated in the analysis in Chapter 4.

TABLE 3.6: Summary of the production measurements. The momentum range corresponds to a linear-acceptance region explained in Section 4.8.

Dataset name	Scale factor	Momentum region	Duration
Prod0980	0.980	2771–2813 MeV/c	579 min.
Prod0983	0.983	2780–2822 MeV/c	558 min.
Prod0985	0.985	2786–2827 MeV/c	591 min.
Prod0990	0.990	2800–2842 MeV/c	654 min.
Prod1000a	1.000	2828–2870 MeV/c	674 min.
Prod1000b	1.000	2828–2870 MeV/c	705 min.
Prod1010	1.010	2856–2899 MeV/c	351 min.
Prod1020	1.020	2885–2928 MeV/c	120 min.

3.7.2 Reference measurement

We measured the (p, d) reaction also with 4022 mg/cm^2-thick CD_2 target in order to obtain the $d(p, d)$ spectrum near the η' emission threshold. In the $d(p, d)$ spectrum, no peak structures of η' mesic nuclei are expected. Thus, this spectrum provides a reference of the physical background in the production measurement, which is mainly the quasi-free processes, as described in Section 2.3.

These reference measurements were performed with five scale factors for the FRS from 0.980 to 1.020, as listed in Table 3.7. The dataset names and durations of the measurements are also tabulated in the table.

TABLE 3.7: Summary of the reference measurements.

Dataset name	Scale factor	Duration
Ref0980	0.980	121 min.
Ref0990	0.990	120 min.
Ref1000	1.000	129 min.
Ref1010	1.010	119 min.
Ref1020	1.020	118 min.

3.7.3 Spectrometer calibration

We measured the proton-deuteron elastic scattering for the calibration of the spectrometer. The 1.6 GeV proton beam was injected onto the 1027 mg/cm^2-thick CD_2 target, and the monochromatic deuterons with the momentum of 2820 MeV/c [5] were ejected by the elastic scattering. By measuring these deuterons at the F4 focal plane, the proper functionality of the spectrometer was confirmed, and the ion-optical properties of the FRS were evaluated.

Table 3.8 summarizes scale factors for the FRS and the number of repetitions of the calibration measurements. Each measurement was performed for about half an hour, and the calibration was repeated every $\sim$ 8 hours. The δ dependence of the optical parameters was obtained by the measurements with the various scale factors. Moreover, the stability of the spectrometer system can be evaluated from the repetitions of the measurements.

TABLE 3.8: Summary of the calibration measurements of the FRS. The calibration measurements were performed with various scale factors from 0.980 to 1.020. The measurements were repeated to check the stability of the whole system.

Scale factor	Number of measurements
0.980	5
0.983	2
0.985	1
0.990	5
0.995	1
1.000	8
1.005	1
1.010	3
1.020	1

3.7.4 Other measurements for dedicated purposes

We performed several short measurements for dedicated purposes. They are summarized as follows.

Production measurement with an unbiased DAQ trigger

Production measurements were performed for a short time with an unbiased DAQ trigger in order to know overall particles including the background protons. Hit information in SC2H or SC41 was required as the unbiased trigger. We compare measured TOF distributions with the unbiased trigger and with the main TOF-based trigger in analysis of the particle identification in Section 4.2.

Empty target measurement

We performed a measurement with the empty target in order to inclusively evaluate an instrumental background from the target ladder, the target chamber, and the dumped primary beam. Since the observed rate of the deuterons at F4 was sufficiently small, the deuterons in the main measurements can be attributed to the reactions in the installed targets.

[5] In the calculation of this deuteron momentum, a detailed analysis of the beam energy and the energy loss in the target were taken into account, as described in Section 4.5.

Intensity calibration

We measured 2.5 GeV primary beams at a wide range of intensities for the calibration of the intensity monitors. The beams were detected with the intensity monitors and the scintillation counters at F2. By taking correlations between the outputs of the detectors, calibration factors for the intensity monitors were evaluated. The analysis is described in Section 4.6.

Confirmation of cross-section analysis

We measured the proton-deuteron backward elastic scattering also at 2.5 GeV in order to confirm our analysis method for a differential cross section. The evaluated cross section of this elastic scattering is compared with known values reported in Berthet *et al.* [47] Moreover, an effective solid angle of the FRS is evaluated by comparing these measurements with and without the slit at the target region. The analysis is explained in Section 4.7.

Chapter 4

Data Analysis

4.1 Overview of Data Analysis

This chapter is dedicated to explain the data analysis. The goal of the analysis is to obtain the missing-mass spectrum of the ^{12}C(p,d) reaction around the η' emission threshold from the data of the production measurements. The spectrum of the d(p,d) reaction is evaluated as well with the data of the reference measurements.

The outline of this chapter is as follows. First, the deuteron identification is described in Section 4.2. Next, the track reconstruction with the MWDC data is explained in Section 4.3. Optics parameters of the spectrometer are analyzed with the data of the proton-deuteron elastic scattering in Section 4.4. Then the missing mass can be calculated using the reconstructed track and the ion-optics parameters in Section 4.5. Next, the calibration of the beam intensity and normalization of the spectra are discussed in Sections 4.6 and 4.7. Furthermore, the momentum acceptance of the spectrometer is evaluated in Section 4.8. Finally, the missing-mass spectra of the ^{12}C(p,d) and d(p,d) reactions are presented in Section 4.9.

4.2 Particle Identification

4.2.1 Concept for particle identification analysis

Deuteron events are identified at the first step of the data analysis. Although a majority of the background protons were rejected by the DAQ trigger based on the TOF between F2 and F4, there are still a substantial amount of the proton events in the recorded data. These are due to the accidental multi-hit protons with a time difference of about 20 ns, as explained in the case (d) in Figure 3.14.

The understanding of the background by the accidental multi-hit is confirmed in measured TOF spectra. TOF between SC2H and SC41 and that between SC41 and SC42 without further corrections are defined and calculated with the measured TDC values as

$$\mathrm{TOF_{raw}(SC2H\text{-}SC41)} = \frac{\mathrm{TDC_{2HL}} + \mathrm{TDC_{2HR}}}{2} - \frac{\mathrm{TDC_{41L}} + \mathrm{TDC_{41R}}}{2}, \tag{4.1}$$

$$\mathrm{TOF_{raw}(SC41\text{-}SC42)} = \frac{\mathrm{TDC_{41L}} + \mathrm{TDC_{41R}}}{2} - \frac{\mathrm{TDC_{42L}} + \mathrm{TDC_{42R}}}{2}, \tag{4.2}$$

where TDC_X stands for the TDC value of the PMT-SC X signal (X = 2HL, 2HR, 41L, 41R, 42L, 42R). Obtained $\mathrm{TOF_{raw}}$(SC2H-SC41) and $\mathrm{TOF_{raw}}$(SC41-SC42) are shown in Figure 4.1 for the unbiased DAQ trigger in the left panel and the TOF-based trigger in the right panel. For the unbiased trigger, both the proton events and the deuteron events

are identified from a comparison with expected values shown in Figure 4.2. A ratio of the amount of the deuterons to that of the protons measured with the unbiased trigger is evaluated to be about 1/200. Furthermore, accidental multi-hit events are seen, which have random values for $\mathrm{TOF_{raw}}$(SC2H-SC41) but proton-like values for $\mathrm{TOF_{raw}}$(SC41-SC42). These events exactly correspond to the case (d) in Figure 3.14, and could not be rejected by the TOF-based trigger, as seen in the right panel of Figure 4.1.

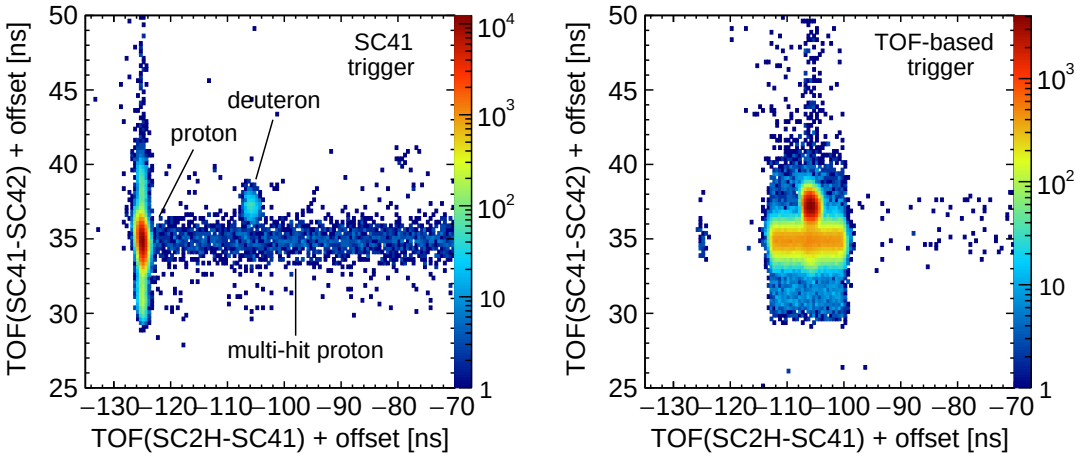

FIGURE 4.1: Measured $\mathrm{TOF_{raw}}$(SC2H-SC41) and $\mathrm{TOF_{raw}}$(SC41-SC42) without various corrections for the unbiased SC41 DAQ trigger (left) and for the TOF-based trigger (right).

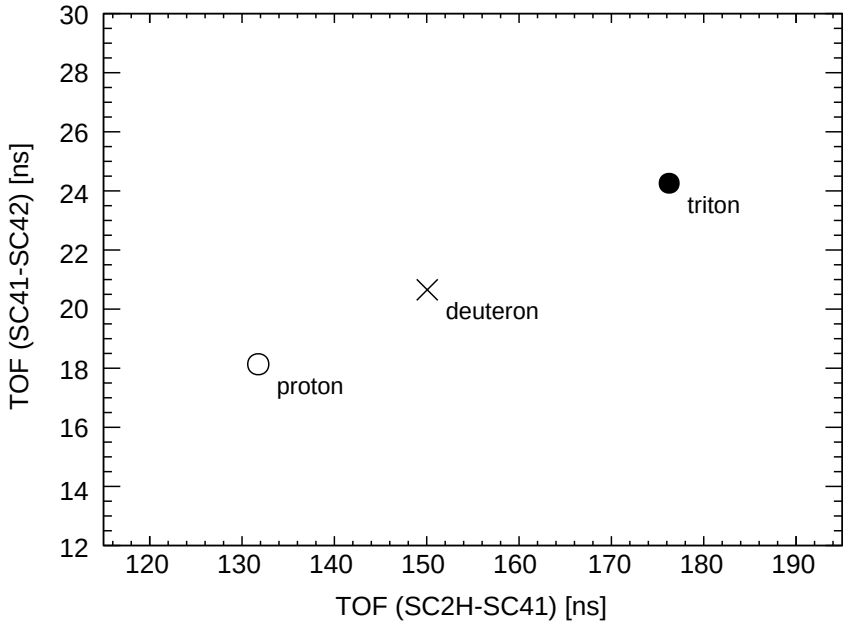

FIGURE 4.2: Expected values of TOF(SC2H-SC41) and TOF(SC41-SC42) for a proton, deuteron, and triton. These are calculated with evaluated path lengths between the scintillators.

Only two scintillation counters, SC2H and SC41, are used in the following analysis of the particle identification. This is because the two Čerenkov counters, HIRAC and TORCH, located downstream of SC41 have inhomogeneity in their internal structures, and requiring a condition for these detectors or SC42, located further downstream, may cause a distortion of a spectrum. Thus, we use only SC2H and SC41 for the particle identification.

Two methods are employed to identify the deuteron events with SC2H and SC41. The first is a waveform analysis of the SC2H signals. The signals from the photomultipliers PMT-SC2HL and PMT-SC2HR were recorded not only by a standard TDC and QDC but also by a waveform digitizer. The multi-hit events, mostly due to the background protons, are rejected by the analysis of these waveforms, as described in Section 4.2.2. Secondly, TOF(SC2H-SC41) is analyzed with various corrections in Section 4.2.3. By applying a tight cut condition for TOF(SC2H-SC41), the background events are further rejected.

4.2.2 Waveform analysis

Typical scintillator signals obtained by the waveform digitizer are shown in Figure 4.3. The blue lines are typical waveforms for the deuteron-like events in the two dimensional TOF shown in Figure 4.1, and the red lines are for the proton-like events. Double hits are seen, as expected, in SC2H for the proton case.

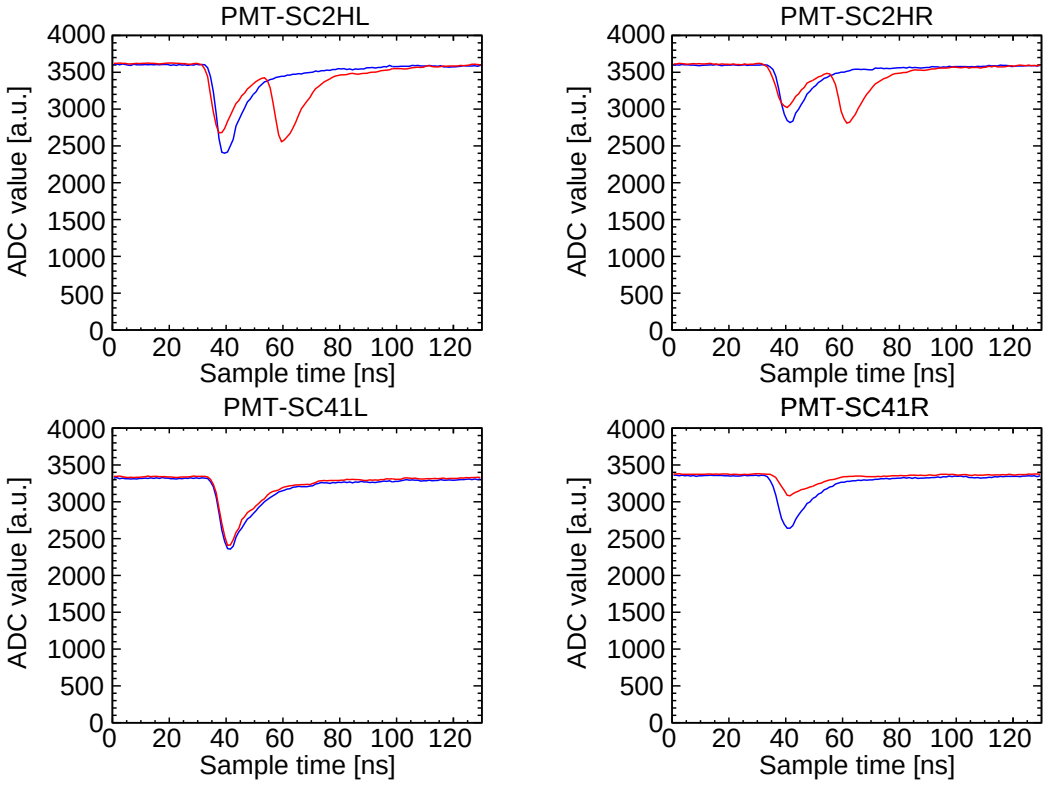

FIGURE 4.3: Examples of the scintillator waveforms are shown for a deuteron-like event (blue) and a proton-like event (red).

In order to identify the single-hit events, we fit the waveforms of PMT-SC2HL and PMT-SC2HR by the following empirical test function:

$$f(t) = (p_0 + p_1 t) - p_2 \cdot \exp\left(-\frac{(t-p_3)^2}{2(p_4+p_5 t)^2}\right), \tag{4.3}$$

where p_i $(i = 0, 1, \ldots, 5)$ are fitting parameters. The first and the second terms represent a baseline, and the third term is a test function of a single peak. The parameter p_5 is phenomenologically introduced to express an asymmetric pulse shape.

A sum of squared residuals (SSR) is used to quantify the result of the fitting. SSR for the photomultiplier PMT-SC2HL is denoted by SSR-2HL and for PMT-SC2HR by SSR-2HR. Figure 4.4 shows obtained distributions of $\log_{10}$(SSR-2HL) and $\log_{10}$(SSR-2HR). Two peaks are seen in both the figures; the peak at the lower SSR corresponds to events well fitted by the single pulses, and the other peak corresponds to the multi-hit events.

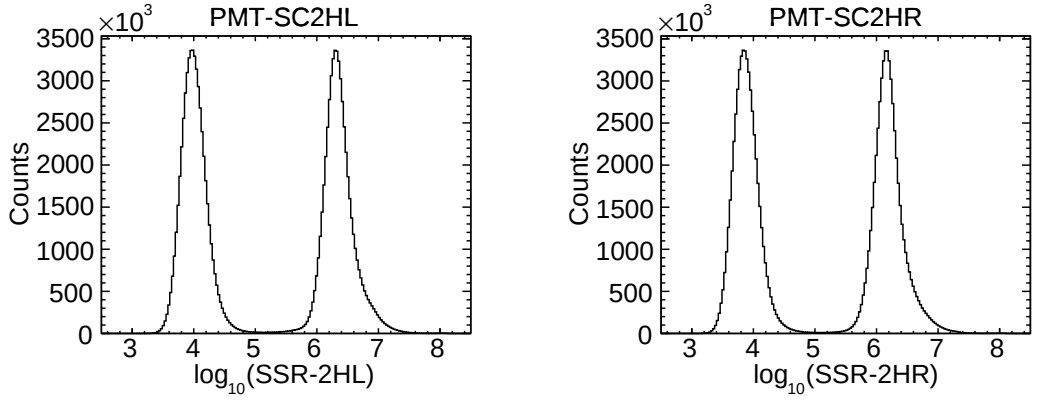

FIGURE 4.4: Obtained histograms of $\log_{10}$(SSR-2HL) (left) and $\log_{10}$(SSR-2HR) (right).

Selection of the single-pulse events is discussed on correlation plots of $\log_{10}$(SSR) and the fitted height parameter p_2 in Equation (4.3). Obtained histograms are shown in Figure 4.5. Correlations between SSR and p_2 can be seen for the single-hit events. Then we select events surrounded by the red lines[1] as the single-hit events, taking into account the correlations between SSR and p_2. Events with $p_2 \geq 4000$ are also rejected because the separation is not clear due to the overflow of the signals.

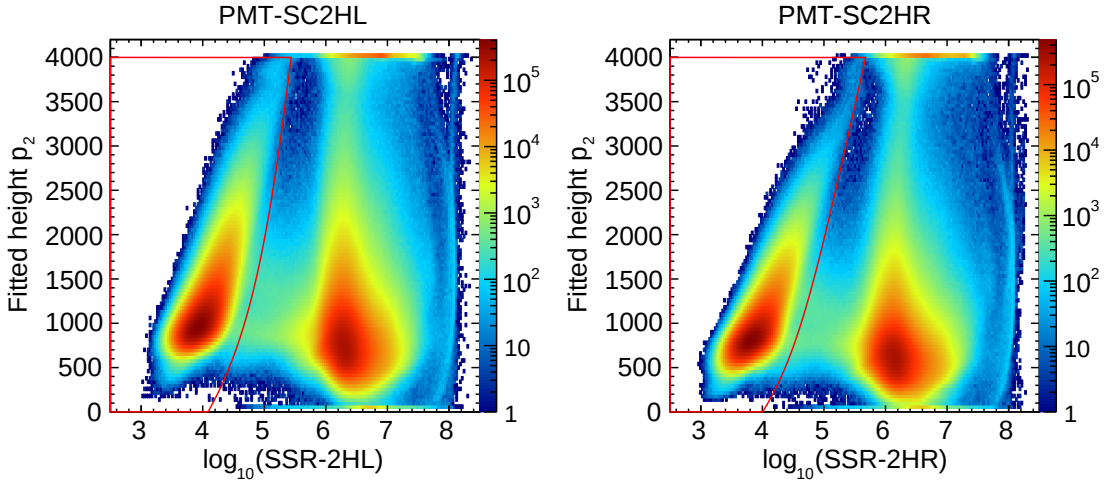

FIGURE 4.5: Correlation plots of $\log_{10}$(SSR) and the fitted height parameter p_2. Obtained histograms are shown for PMT-SC2HL (left) and PMT-SC2HR (right). Red lines are used to select the single-hit events.

[1] These red curves are determined as follows. First, we fitted the main part of the single pulse events in Figure 4.5 by a function $\log_{10}(\text{SSR}) = f_1(p_2)$ = linear function + exp(linear function) and the other part by $\log_{10}(\text{SSR}) = f_2(p_2)$ = constant function. Then, $0.3f_1(p_2) + 0.7f_2(p_2)$ is used as a boundary.

4.2.3 TOF analysis

TOF between SC2H and SC41 is analyzed for further rejection of the background protons. Two types of corrections are introduced to improve the time resolution:

$$\begin{aligned}\mathrm{TOF}_{\mathrm{corrected}}(\mathrm{SC2H\text{-}SC41}) = \mathrm{TOF}_{\mathrm{raw}}(\mathrm{SC2H\text{-}SC41}) + (x \text{ and } a \text{ corrections}) \\ + (\text{time-walk corrections}).\end{aligned} \tag{4.4}$$

The first corrections are introduced to compensate path length and velocity dependences of TOF, which appear as correlations with horizontal position x and angle a of the reconstructed track. The second corrections are so-called time-walk corrections, which cancel pulse-height dependences of the measured timing.

The corrections with x and a are explained in Figure 4.6. The left-top panel shows a correlation between $\mathrm{TOF}_{\mathrm{raw}}$(SC2H-SC41) and the horizontal position x at F4 [2]. We correct the observed correlation by a fourth-order polynomial, and a figure with the correction is shown in the right-top panel. Next, a correlation with the horizontal angle a shown in the left-bottom panel is corrected by a second-order polynomial. As a result, also the correlation with a is compensated, as shown in the right-bottom panel.

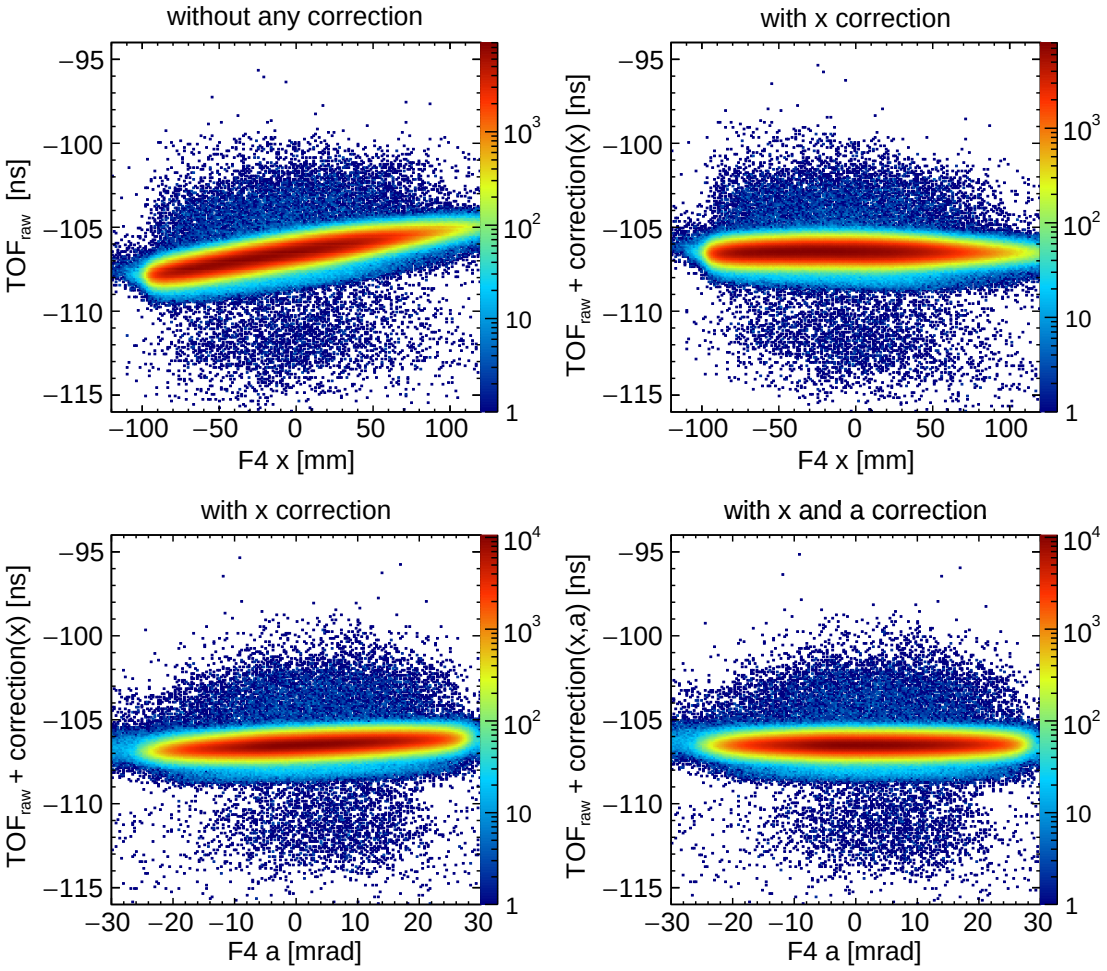

FIGURE 4.6: Horizontal position and angle dependences of TOF(SC2H-SC41). See the text for the detail.

[2] x with an optics correction is used. See Sections 4.3 and 4.4 for analysis of the track reconstruction and optical corrections.

The time-walk corrections are discussed with the height parameters p_2, obtained by the waveform fitting. The four panels on the left-hand side in Figure 4.7 show correlations between TOF and the p_2 parameters for PMT-SC2HL, PMT-SC2HR, PMT-SC41L, and PMT-SC42R. Then we phenomenologically introduce corrections with quadratic functions of $\log_{10}(p_2)$, taking into account correlations of the pulse heights between the left PMT and the right PMT. As a result, we obtain TOF including the time-walk corrections, as shown in the four panels on the right-hand side of Figure 4.7.

Obtained TOF spectra including all the corrections are shown in Figure 4.8 for all the data sets of the production measurements. Histograms with the black lines correspond to the total events, while those with the red lines are for the single-hit events selected by the waveform analysis. The accidental events are strongly suppressed by the single-hit selection, while the deuteron peaks are almost kept. Furthermore, a good time resolution of $\sigma = 1.7 \times 10^2$ ps is achieved for the deuterons with the various corrections introduced in this section.

For main analysis of the missing-mass spectrum, we select events within the $\pm 5\sigma$ regions around the deuteron peaks in the TOF spectra, in addition to the single-hit selection by the waveform analysis. These $\pm 5\sigma$ regions are shown by the red dashed lines in Figure 4.8.

4.2.4 Deuteron identification efficiency

We evaluate the deuteron identification efficiency in three steps as follows. First, events with the overflow pulse height and those with no TDC value are rejected, which leads to 0.6–0.9% rejection of the deuteron events. Secondly, the overkill by the single-pulse waveform selection is evaluated using a TOF spectrum for the rejected events by this single-pulse selection. Such a spectrum is shown by the green dotted line in the top panel of Figure 4.8 as an example. The overkill probability is evaluated to be 2–3% by integrating the small enhancement at the deuteron TOF position. Thirdly, the overkill probability by the TOF selection is estimated to be 0.2–0.3% from the tail structure of the deuteron peak in the TOF spectrum. By combining these three contributions, the deuteron identification efficiency is evaluated to be 96–97% for all the data sets of the production measurements.

The deuteron identification efficiency is taken into account for the absolute normalization of the spectra in Section 4.7.2. There would be additional deuteron overkill related to accidental multi-hit, for example due to a hardware dead time in the DAQ circuit. We estimate the additional overkill by the accidentals is at most a few percent level from the typical particle rate at the focal planes. This is sufficiently smaller than the other systematic error of $\pm 13\%$ for the absolute normalization of the spectra, which is discussed in Section 4.7.2.

4.2.5 Proton rejection efficiency

Possible contamination of the remaining protons is evaluated from the constant regions of the TOF spectra. The regions indicated by the black dashed lines in Figure 4.8 are used for the evaluation, because the deuteron peaks in the TOF spectra have long tail structures on their right side[3], as observed in the figure. As a result, the evaluated level of the proton contamination is 2×10^{-4} compared with the number of the identified deuterons. This makes a negligibly small contribution in the missing-mass spectrum.

[3] These tail structures are due to accidental events including both deuteron and proton at F2 and only the deuteron at F4. If the proton is slightly earlier than the deuteron at F2 and it is not transmitted to F4, such an event makes a tail structure on the right-hand side of the deuteron peak in the TOF spectrum. In an opposite case, with a proton slightly later at F2, TOF is not affected because the timing is measured by leading-edge discriminators.

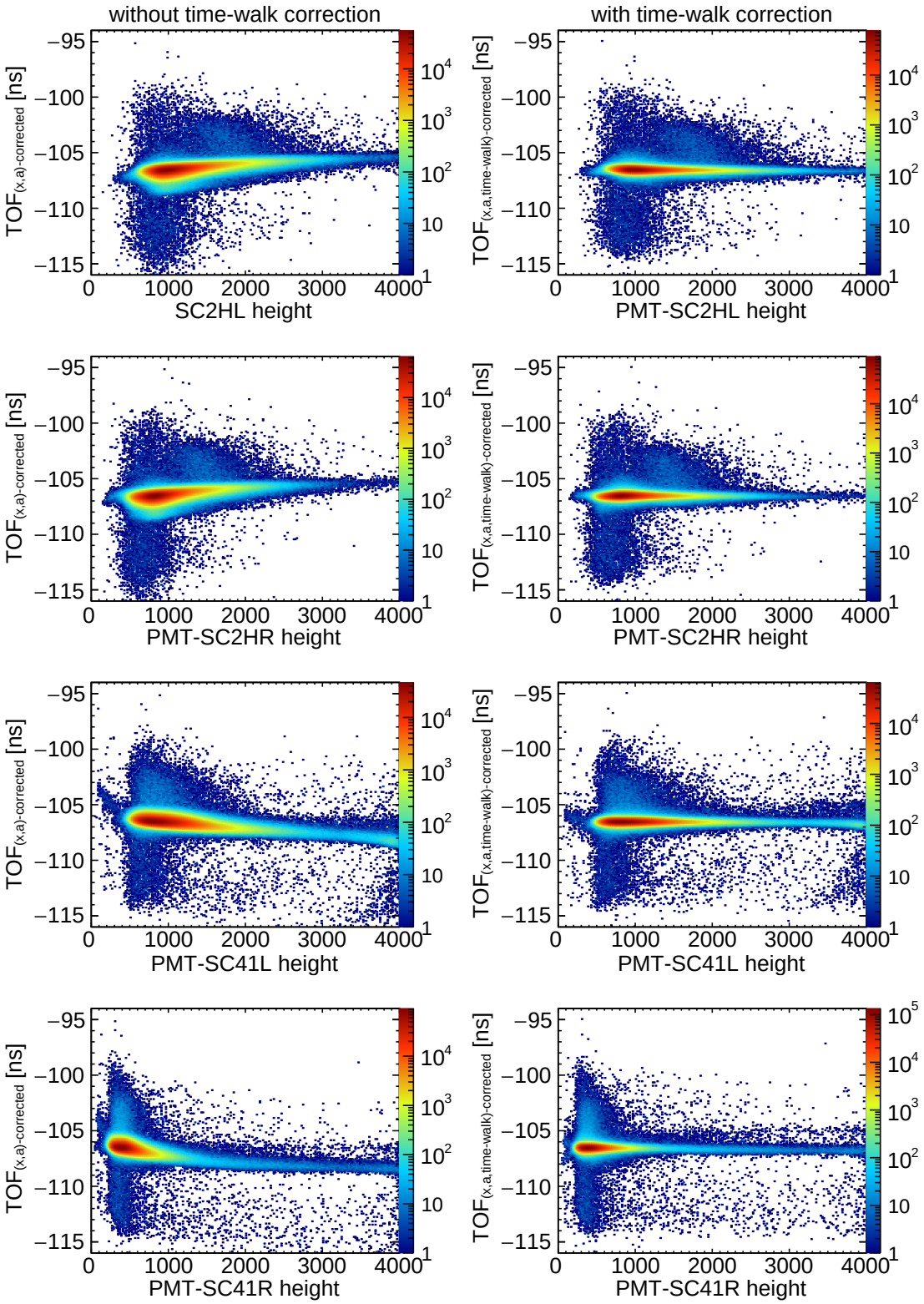

FIGURE 4.7: Correlations between TOF(SC2H-SC41) and the pulse height parameters p_2 are shown without the time-walk corrections (left) and with the corrections (right) for PMT-SC2HL, PMT-SC2HR, PMT-SC41L, and PMT-SC42R.

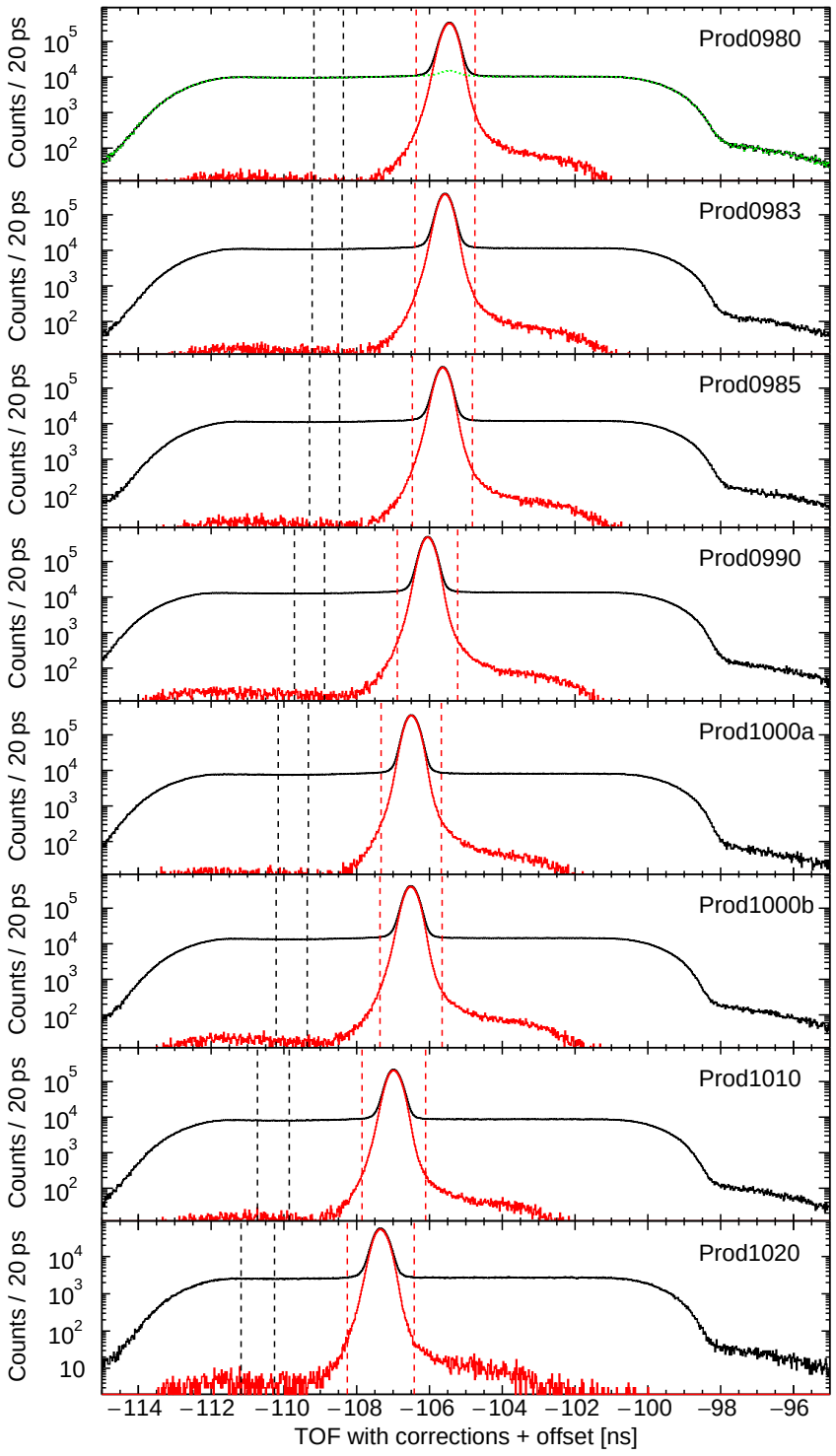

FIGURE 4.8: Obtained TOF spectra including all the corrections for all the production data sets. Total events are shown by the black histograms, while events selected by the waveform analysis are shown in red. The regions indicated by the red dashed lines are used for the deuteron selection, and those by the black dashed lines are used to evaluate the proton contamination. The green dotted line in the top panel show a TOF spectrum for events rejected by the waveform analysis. This spectrum is used for evaluation of the deuteron overkill by the waveform selection.

4.3 Analysis of Multi-Wire Drift Chambers

Data of the MWDCs are analyzed to reconstruct tracks of the deuterons at the F4 focal plane. The analysis consists of two steps as follows:

1. A measured drift time is converted to a drift length.
2. χ^2 fitting with a linear track is performed for all possible combinations of hit positions, and a track with a minimum χ^2 is adopted.

We explain the calibration of the time-to-length conversion in Section 4.3.1 and the χ^2 fitting of the track in Section 4.3.2. Moreover, a position resolution and tracking efficiency are evaluated in Sections 4.3.3.

4.3.1 TDC to drift length conversion

We construct a calibration function to convert a measured drift time to a drift length by an iterative analysis. The calibration function is constructed for every 16 wires read out by one ASD[4], because we can assume a same time offset by hardware for these 16 wires. An analysis method of the calibration functions is explained in this section.

An initial function to convert a drift time to a drift length is obtained by assuming a uniform distribution of the converted drift length. This function $L_0(t)$ can be constructed using the measured drift-time distribution $T(t)$ as

$$L_0(t) = 2.5\,\mathrm{mm} \times \frac{\int_{t_0}^{t} T(t')dt'}{\int_{t_0}^{t_{\max}} T(t')dt'}\,, \tag{4.5}$$

where $t_{\max}$ is a TDC value for the maximum drift time and t_0 for the minimum drift time.

The conversion function is then iteratively updated using $L_0(t)$ as an initial function. In order to obtain conversion functions of one test plane for the next step, we reconstruct a track using only the other types of the planes[5], and deduce a hit position in the test plane based on the reconstructed track. Then the drift length in the test plane is evaluated by a distance from the hit position to the nearest wire. The bottom panel of Figure 4.9 shows a correlation plot of the evaluated drift length and the measured TDC value in the nearest wire. The updated calibration function can be obtained by fitting this correlation, as shown by the red curve. Such analysis is iteratively continued with the data of the production measurements until no significant deviation of the calibration function is seen.

One of the advantages of this iterative treatment is the fact that the assumption of the uniform distribution for the converted length is not necessary. Furthermore, this method is not affected by multi hits. The top panel of Figure 4.9 shows the drift time distributions for the total hits in black and for the nearest wire to the reconstructed track in red. A contribution of the multi hits is seen in this figure, which can cause a distortion for the calibration with the uniform-distribution assumption.

The calibration is repeated for the data sets of about every 1 hour in order to check a time dependence of the experimental environment. Figure 4.10 shows obtained drift lengths for two fixed TDC values as functions of the time and date of the data sets. A daily-periodic variation can be seen with a maximum shift of about 100 μm. This could be due to a temperature variation, because the local maxima of the drift lengths are seen in the afternoon. In addition, two datasets have deviated drift lengths, as shown by the

[4] 16 wires read out by one ASD always belong to a same plane.

[5] For example, a track is reconstructed only with the U, U', V, and V' planes, when we consider an updated calibration function for the X2 plane.

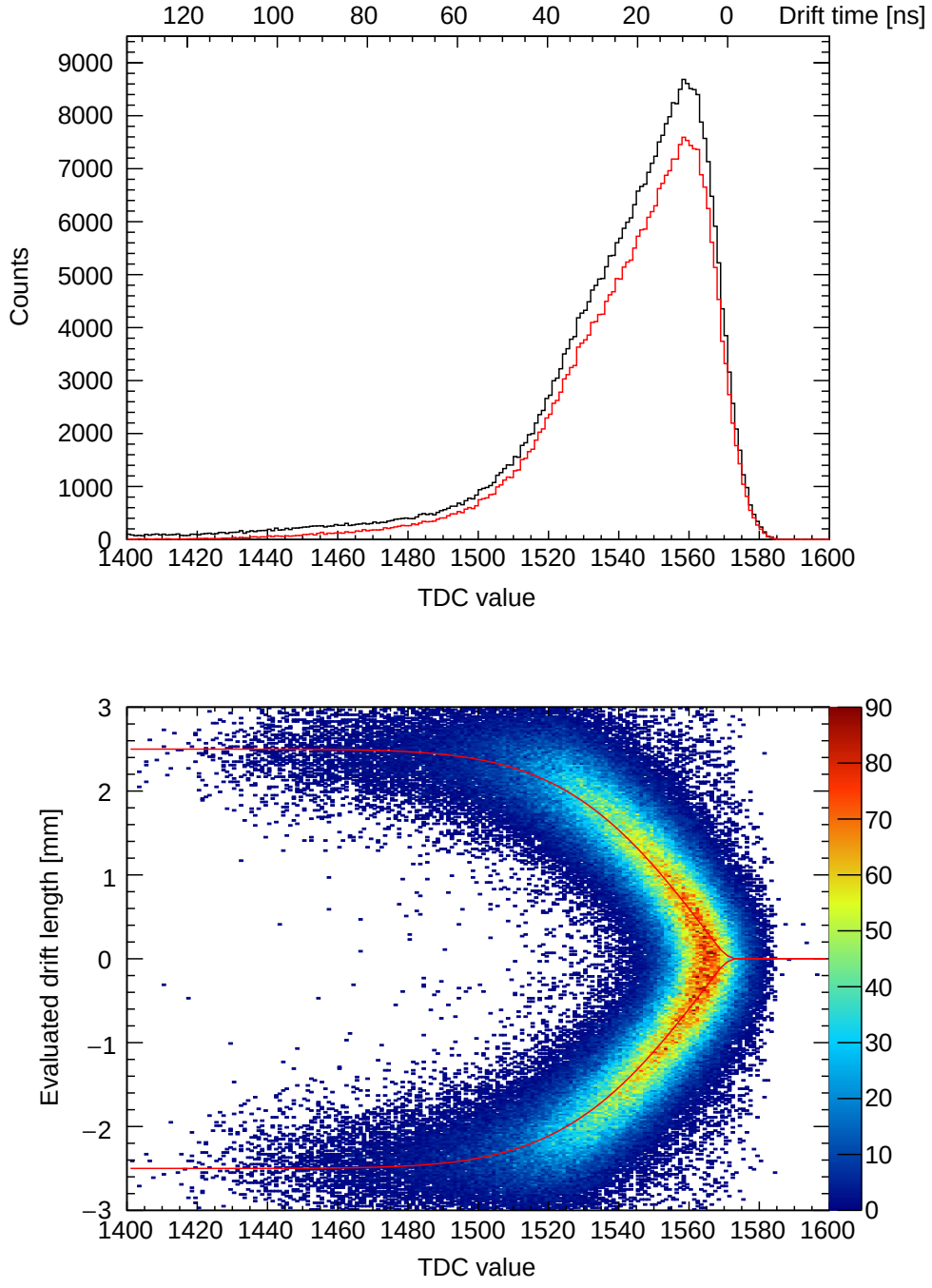

FIGURE 4.9: Drift time distributions (top) and a correlation between the measured time and the evaluated drift length (bottom) are shown for the middle 16 wires in the U plane of MWDC41. In the top panel, the drift time distributions are shown for total hits in black and for the nearest wire to the deduced hit position in red. The red curve in the bottom panel shows the evaluated time-to-length conversion function.

open circles and the open stars. These are because the data sets with the open circles were taken with a different high-voltage setting, and those with the open stars were taken with an unbiased SC2H trigger which had a slightly different trigger timing. Since these minor effects are clearly reproduced, we can confirm a good quality of the data and correctness of the analysis.

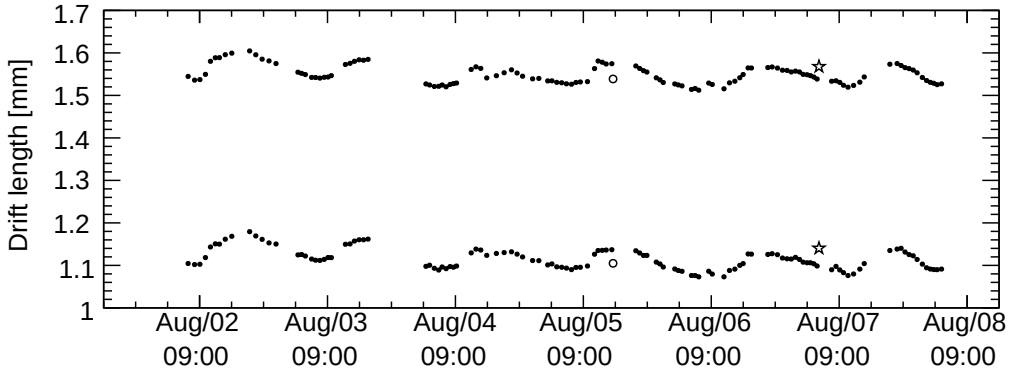

FIGURE 4.10: A periodic variation of the drift lengths is shown for the middle 16 wires in the U plane of MWDC41. The upper points are the obtained drift lengths for a TDC value of 1540, and the lower points are for a TDC value of 1550. Two data sets measured with different conditions are shown by the open markers. See the text for their detail.

4.3.2 χ^2 fitting of track

We perform χ^2 fitting of hit positions for the track reconstruction. A track at F4 is parametrized by a horizontal position x and slope x' and a vertical position y and slope y' at a reference position taken at the V' plane of MWDC41. Then χ^2 can be defined as

$$\chi^2(x, x', y, y') = \sum_i \left(\frac{(w_i \pm l_i) - ((x + z_i x') \cos\theta_i + (y + z_i y') \sin\theta_i)}{\sigma_i} \right)^2, \tag{4.6}$$

where w_i is the wire position with a hit, and l_i is the converted drift length in the i-th plane. As w_i is defined in the tilted coordinate of the plane, $(w_i \pm l_i)$ represents two possible hit positions in this coordinate. z_i is the position of the i-th wire plane in the beam direction, and θ_i is the tilt angle of this plane. σ_i is a plane resolution in the i-th plane obtained in Section 4.3.3. Since there are some possibilities in each plane for the sign of the drift length and the choice of the hit in case of multi-hit events, we perform the χ^2 fitting for all the possible combinations[6]. Then we adopt a result which gives a minimum χ^2 as the reconstructed track at F4.

However, this conventional method with the χ^2 fitting creates a distortion in the reconstructed position spectrum. The origin of the distortion is the fact that the minimum χ^2 is always chosen, and even in a simplified case with an exactly known time-to-length function, the distortion is reproduced by a simulation, as we demonstrate in Appendix B. This distortion appears strongly in the drift directions of the wire planes used in the fitting, and it may cause structures in the spectrum around the wire positions.

In order to avoid a possible distortion of the position distribution at the F4 focal plane, we employ only the U-type and V-type planes for the main track reconstruction. Then

[6] The minimization of χ^2 for a given combination can be done analytically for the χ^2 defined in Equation (4.6), because it is a second-order function of the fitting parameters.

structures due to the distortion may appear in the U or V directions (15° from the horizontal direction x), but those in the x direction, which is directly related to the momentum, can be reduced. For the tracking only with the U-type and V-type planes, we require that at least six planes have hits and every pair of the planes have hits at least in one of the paired planes[7]. A reduced χ^2 distribution obtained by this tracking is shown in Figure 4.11. Events with $\chi^2/\mathrm{ndf} < 20$ are selected for the analysis of the missing mass.

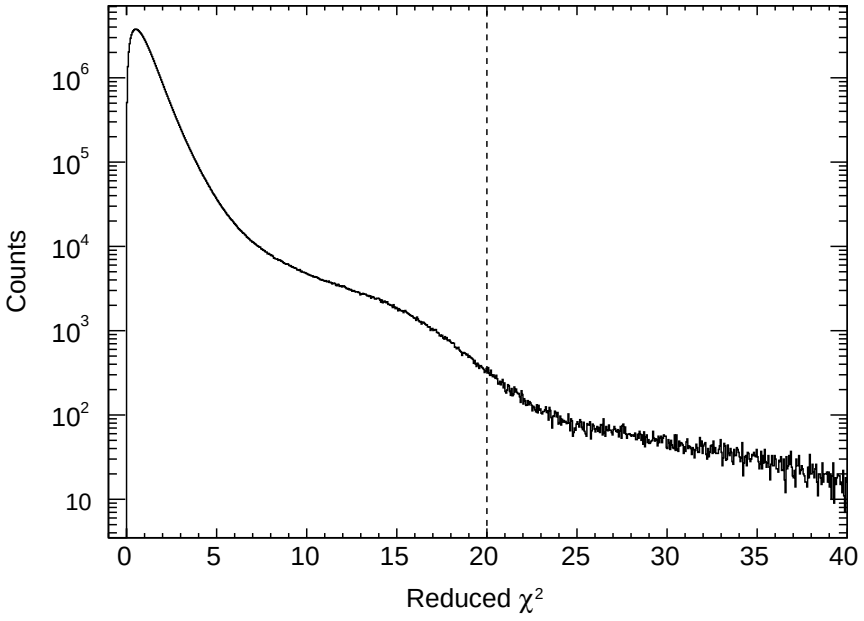

FIGURE 4.11: A distribution of the reduced χ^2 of fitting only with the U and V-type planes. We select events with $\chi^2/\mathrm{ndf} < 20$ for the further analysis, as indicated by the dashed line.

Furthermore, we introduce a random smearing using a Gaussian distribution with a standard deviation of 3 mm. Since this scale is as large as the maximum drift length, the distortion caused by the tracking method is sufficiently reduced. This additional smearing is added only for the analysis of the production measurements and the reference measurements after the ion-optical correction described in Section 4.4.

4.3.3 Resolution and efficiency

A position resolution of each wire plane is evaluated with a method described in Carnegie *et al.* [48] In this method, two residuals are considered for each plane: a residual with a tracking including the tested plane and that excluding this plane. Then a good estimation for the resolution of this plane is given by a geometrical mean of standard deviations of the two types of the residual distributions.

Obtained resolutions are shown in the top panel of Figure 4.12 as functions of the time and date of the data sets. The black points show the averaged resolution for the U and U' planes of MWDC41, the red points for the V and V' planes of MWDC41, the green

[7] For example, an event with hits in the U,U',V planes of MWDC41 and U',V,V' planes of MWDC42 is analyzed. In this example, the sign of the drift length in the V plane of MWDC41 and that in U' plane of MWDC42 are not well determined. In such a case, we perform a tracking including the X-type planes only to fix the signs of the drift lengths in these planes, before we perform the main tracking.

points for the U and U' planes of MWDC42, and the blue points for the V and V' planes of MWDC42. A typical resolution of about 0.20–0.23 mm is obtained, taking into account a periodic variation also seen for the resolution.

The tracking efficiency is evaluated for the deuteron events[8] by two steps as follows. Firstly, we evaluate a probability of having enough hits in the MWDCs, which is necessary for the χ^2 fitting explained in Section 4.3.2. Secondly, for the events with the enough hits, a probability of having $\chi^2/\,\mathrm{ndf} < 20$ is evaluated. The overall tracking efficiency is obtained by multiplying the above two probabilities. The bottom panel of Figure 4.12 shows the obtained efficiency as a function of the time and date of the data sets for the production and reference measurements. The obtained tracking efficiency is 0.998–0.999 throughout the experiment.

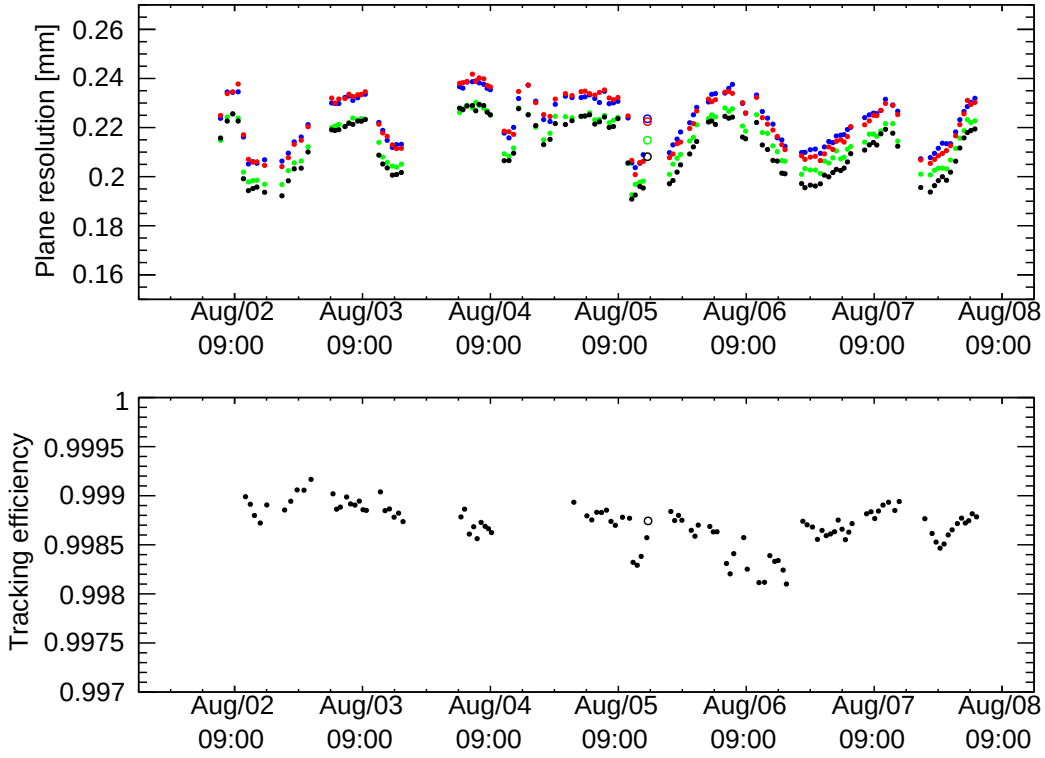

FIGURE 4.12: The position resolutions and the tracking efficiency of the MWDCs are shown in the top and bottom panels, respectively. These are plotted as functions of the time and date of the data sets. The open circles correspond to the data sets with a different high-voltage setting. The colors in the top panel correspond to the different planes of the MWDCs; the averaged resolution for the U and U' planes of MWDC41 is shown in black, for the U and U' planes of MWDC41 in red, for the U and U' planes of MWDC42 in green, and for the V and V' planes of MWDC42 in blue. See the text for the detailed definitions of the position resolutions and the tracking efficiency.

[8] For the evaluation of the tracking efficiency, we select the deuteron events only by the SC2H waveform analysis, because the TOF analysis requires tracking information for the "x and a corrections" in Equation (4.4).

4.4 Ion-Optics Calibration

The data of the calibration measurements are analyzed in order to obtain the ion-optical properties of the spectrometer. The top panel of Figure 4.13 shows the reconstructed horizontal positions and angles at F4 in the calibration measurements. The figure is overlaid for five measurements at scale factors of 0.98, 0.99, 1.00, 1.01, and 1.02. The elastic peaks are observed as the vertical lines in the figure, on the continuous background due to the reaction with carbon in the CD_2 target. The positions of the elastic peaks correspond to the excitation energy about 80 MeV from the ground state of ^{11}C. The bottom panel of Figure 4.13 shows the positions and angles with an optics correction. The analysis to determine the optics-correction parameters is explained in the following paragraphs.

Firstly, for each calibration peak, the horizontal position x is fitted by a quadratic function of the horizontal angle a. Then, coefficients p_0, p_1, and p_2 defined in

$$x = p_0 + p_1 a + p_2 a^2 \tag{4.7}$$

are obtained for all the data sets.

Secondly, momentum dependence of these coefficients are analyzed. When the calibration is carried out at a scale factor f, the emitted deuteron has a relative momentum deviation of $\delta = \frac{1}{f} - 1$ in the spectrometer. In order to evaluate the δ dependence, the obtained p_0, p_1, and p_2 for all the calibration measurements are plotted as a function of δ in the left three panels of Figure 4.14. The top left shows p_0, which is the horizontal position at $a = 0$. This graph is fitted by a second-order polynomial as shown by the red curve. The middle-left panel shows p_1, which represents distance to the focus position. As we can see in the figure, p_1 linearly depends on δ, which means a tilted focal plane. The focus position was slightly shifted during the intensity calibration measurement. Calibration data before that change are shown by cross marks ($\times$), and after the change by open circles ($\circ$). A constant shift is observed between the cross marks and open circles. Thus, they are fitted separately by linear functions with a same slope but different constant parameters, as shown by the red line and the blue line in the figure. The bottom-left panel shows δ dependence of p_2. This graph is fitted by a second-order polynomial. As a result of the fittings described above, x can be expressed with a and δ as

$$x = (p_{00} + p_{01}\delta + p_{02}\delta^2) + (p_{10} + p_{11}\delta)a + (p_{20} + p_{21}\delta + p_{22}\delta^2)a^2. \tag{4.8}$$

The fitted parameters p_{ij} are listed in Table 4.1. In particular, p_{01} represents the dispersion of the optics. The obtained value is almost consistent with the designed value of -36.4 mm/%.

TABLE 4.1: Fitted parameters for the ion-optics calibration. The value of p_{10} after the focus position shift is written in the parenthesis.

Parameter	Fitted value
p_{00}	-3.27 mm
p_{01}	-35.14 mm/%
p_{02}	-0.59 mm/%^{2}
p_{10}	0.086 mm/mrad (-0.057 mm/mrad)
p_{11}	-0.473 mm/(mrad·%)
p_{20}	0.0032 mm/mrad^2
p_{21}	0.0011 mm/(mrad^2·%)
p_{22}	0.0013 mm/(mrad^2·%^{2})

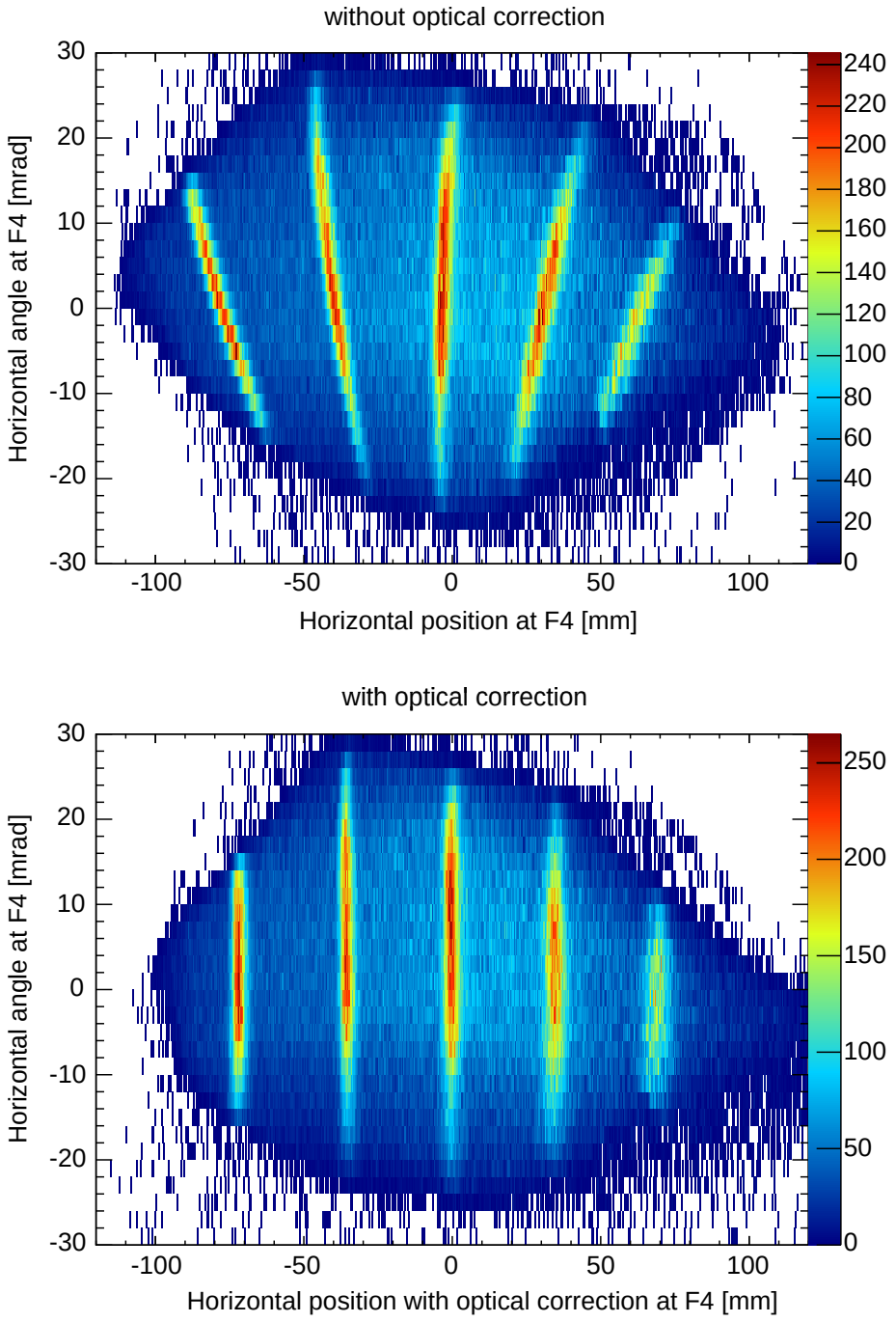

FIGURE 4.13: Horizontal positions and angles at F4 obtained in the calibration measurements. The top panel is before the optics correction and the bottom panel is after the optics correction. The figures are overlaid for five measurements at scale factors of 0.98, 0.99, 1.00, 1.01, and 1.02.

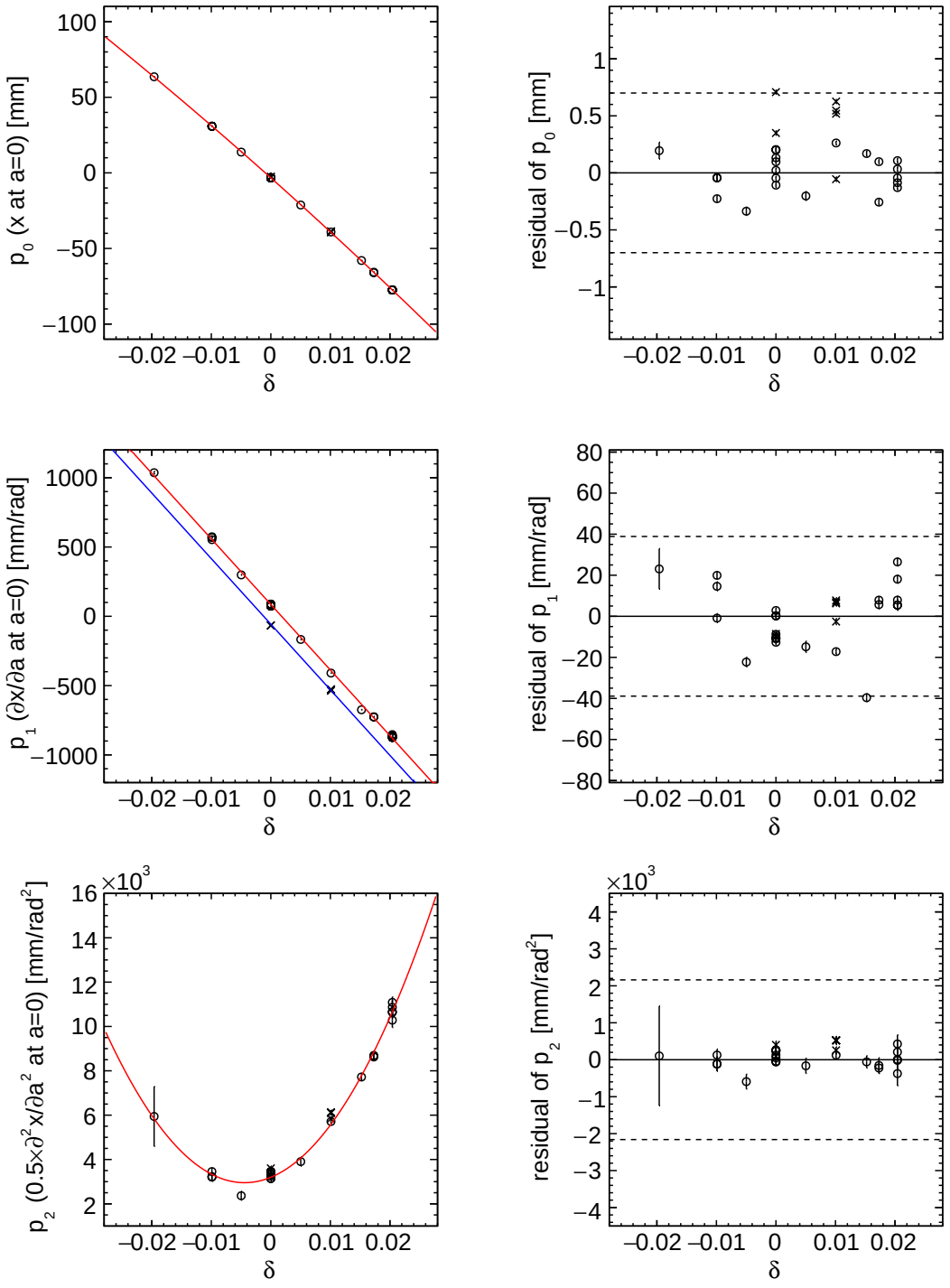

FIGURE 4.14: Fitting of the optics calibration parameters. Position x deduced at $a = 0$ was fitted by a quadratic function of δ shown by a red line (top, left). The slope of this plot is a value of dispersion at F4. Next, the first derivative $\partial x/\partial a$ deduced at $a = 0$ was fitted by a linear function of δ (second top, left). Datasets before the change of the focal plane position are shown by cross marks and fitted by a blue line, while the datasets after it are shown by open circles and fitted by a red line.

In the analysis of the main measurements, the relative momentum deviation of the deuteron can be obtained with the measured position x and angle a by solving Equation (4.8) for δ. As this is a second-order equation of δ, it can be analytically solved, and $\delta(x, a)$ is obtained as a function of x and a. We also define an optics-corrected position x_c by

$$x_c = (\text{dispersion}) \times \delta(x, a) = p_{01} \times \delta(x, a) \tag{4.9}$$

for practical convenience in analysis. This x_c is used in the bottom panel of Figure 4.13.

The stability of the calibration is evaluated by using the residuals in the fittings. The right three panels of Figure 4.14 show the residual plots of the fittings in the left panels. The dashed lines in the residual plots correspond to 0.7 mm shift in x_c assuming $|a| = 18$ mrad. Since we select events with $|a| < 18$ mrad in the missing-mass analysis in Section 4.9, we evaluate the systematic error for the stability of the calibration to be 0.7 mm.

In the calibration measurements at the FRS scale factors of 1.01 and 1.02, the ground state and excited states of ^{11}C are observed near the edge of the acceptance. The positions of these peaks are used for additional confirmation of the above calibration, as described in Appendix C.

4.5 Calculation of Missing Mass

A calculation of the missing mass in the (p,d) reaction is described in this section. First, a calculation of the deuteron momentum and a correction for the beam energy are explained. Then we calculate the missing mass using the deuteron momentum and the beam energy. The expected resolution and systematic errors for the missing mass are discussed as well.

4.5.1 Deuteron momentum

The deuteron momentum P_d in the main measurement is calculated with δ obtained by the optics correction and the scale factor of the FRS, f_{FRS}, as

$$P_d = f_{\text{FRS}}(1 + \delta) \times P_{\text{calibration}}. \tag{4.10}$$

$P_{\text{calibration}}$ is the monochromatic momentum of the deuterons in the calibration measurements. $P_{\text{calibration}}$ is evaluated to be 2828.0 ± 1.0 MeV/c by a kinematical calculation including energy losses in the CD_2 target. The values used in the calculation are listed in Table 4.2.

TABLE 4.2: Values used in the calculation of the calibration momentum are listed. Determination of the beam energy is described in Appendix A. Energy losses of the beam and the ejectile are calculated for a half thickness of the CD_2 target by using the LISE++ calculator [49], in which the ATIMA program [50] based on the LS theory [51] is implemented.

Title of value	Value
Beam energy from SIS-18 (1.6 GeV beam)	1621.6 ± 0.8 MeV
Energy loss (proton) in 1/2 of the target	-1.0 MeV
Beam energy at the middle of the target	1620.6 ± 0.8 MeV
Deuteron energy at the middle of the target	1518.9 ± 0.8 MeV
Energy loss (deuteron) in 1/2 of the target	-1.1 MeV
Energy of the emitted deuteron	1517.8 ± 0.8 MeV
Momentum of the emitted deuteron	2828.0 ± 1.0 MeV/c

4.5.2 Correction for beam energy

An extraction-time dependence of the beam energy is observed in the proton-deuteron elastic scattering at 2.5 GeV. As described in detail in Appendix A, the beam energy decreases with a rate of $\frac{dT_p}{dt} = -1.57$ MeV/s during each 4-second spill. By taking into account this observed time dependence, we calculate the kinetic energy of the primary proton as

$$T_p = \overline{T}_p - 1.57 \text{ MeV/s} \cdot (t_{\text{extraction}} - \bar{t}_{\text{extraction}}). \tag{4.11}$$

$\overline{T}_p$ is a mean energy of the beam, which is evaluated to be 2499.1 ± 2.0 MeV in Appendix A. The second term is the correction for the beam energy with the extraction time $t_{\text{extraction}}$[9]. A mean value of the extraction time $\bar{t}_{\text{extraction}}$ is subtracted from $t_{\text{extraction}}$ to keep the mean beam energy unchanged.

4.5.3 Calculation of missing mass

In this section, we explain a calculation of the missing mass in the ^{12}C (p,d) reaction using the deuteron momentum P_d obtained in Equation (4.10) and the proton kinetic energy T_p in Equation (4.11). First, we calculate the momenta of the beam and the deuteron, P'_p and P'_d, including corrections for the energy losses in the target as

$$P'_p = \sqrt{(T_p + M_p - \Delta E_p)^2 - M_p^2}, \tag{4.12}$$

$$P'_d = \sqrt{\left(\sqrt{P_d^2 + M_d^2} + \Delta E_d\right)^2 - M_d^2}, \tag{4.13}$$

where M_p and M_d are the proton mass and the deuteron mass, and ΔE_p, ΔE_d are the calculated energy losses in the half thickness of the target, as listed in Table 4.3. Then the missing mass in the ^{12}C(p,d) reaction can be calculated as

$$M_{^{12}\text{C}(p,d)X} = \sqrt{\left(M_{^{12}\text{C}} + \sqrt{M_p^2 + P_p'^2} - \sqrt{M_d^2 + P_d'^2}\right)^2 - \left(P'_p - P'_d\right)^2}. \tag{4.14}$$

Since an important quantity is the missing mass around the η' emission threshold, final spectra are plotted in an excitation energy from the threshold defined by

$$E_{\text{ex}} - E_0 = (M_{^{12}\text{C}(p,d)X} - M_{^{11}\text{C}} - M_{\eta'})c^2. \tag{4.15}$$

Missing masses are calculated also for target masses of the deuteron and the neutron for a comparison with the data of the reference measurements. The neutron mass is used as an approximation for a nucleon in the target nucleus to discuss the inclusive background. These missing masses are denoted by $M_{d(p,d)X}$ and $M_{n(p,d)X}$, and they are calculated with Equation (4.14) substituting $M_{^{12}\text{C}}$ by M_d and M_n, respectively.

TABLE 4.3: Calculated energy losses in the production and reference measurements.

Evaluated energy losses	Production (carbon)	Reference (CD_2)
$-\Delta E_p$ in 1/2 of the target	−3.6 MeV	−3.7 MeV
$-\Delta E_d$ in 1/2 of the target	−4.3 MeV	−4.4 MeV

[9] $t_{\text{extraction}}$ is obtained from a start timing of each spill and a 1 kHz clock recorded by the VME scaler.

4.5.4 Evaluation of the experimental resolution

The missing-mass resolution in the main measurements is evaluated based on the measured proton-deuteron elastic peaks combined with energy loss and straggling calculations. We consider five contributions listed in Table 4.4. Firstly, the resolutions due to the energy loss and straggling (2., 3.) and the smearing (5.) are calculated as listed in the table. Next, the contribution from the energy spread of the 2.5 GeV beam is evaluated using the elastic peak with the 2.5 GeV beam. The left panel of Figure 4.15 shows the elastic peak at 2.5 GeV with the optics correction and the beam-energy correction. The obtained width of the peak is 1.6 mm (σ). Then an upper limit of the contribution (1.) is estimated by subtracting expected energy-loss and straggling contributions and attributing all the rest to the energy spread of the beam. Similarly, an upper limit for the contribution from the spectrometer side (4.) for the deuteron momentum in the main measurements, around 2.8 GeV/c, is evaluated with the elastic peak at 1.6 GeV. This elastic peak at 1.6 GeV is shown in the right panel of Figure 4.15, and its width is estimated to be 1.7 mm (σ). Finally, taking the square root of the quadratic sum of all the contributions, the overall experimental resolution is evaluated to be 2.5 ± 0.1 MeV/c^2.

TABLE 4.4: Evaluated contributions to the experimental resolution are listed.

	Contribution to the missing-mass resolution	Evaluated value
1.	Energy spread of the 2.5 GeV primary beam	< 0.7 MeV/c^2
2.	Uncertainty of energy loss in the target	1.2 MeV/c^2
3.	Energy straggling at F2	0.7 MeV/c^2
4.	Resolution in the spectrometer side for $P_d \sim 2.8$ GeV/c	< 0.7 MeV/c^2
5.	Smearing values for horizontal positions ($\sigma = 3$ mm)	2.0 MeV/c^2
	Total	2.4–2.6 MeV/c^2

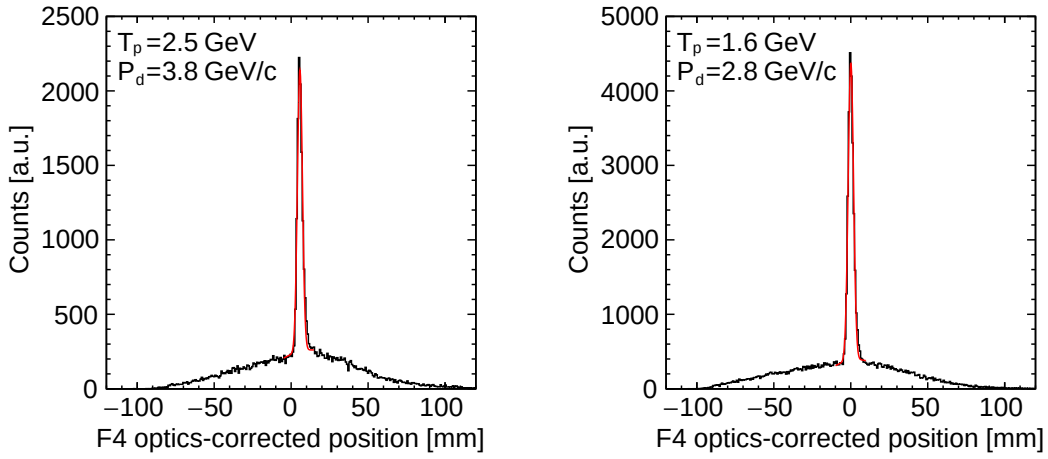

FIGURE 4.15: Proton-deuteron elastic peaks at the incident energies of 2.5 GeV (left) and 1.6 GeV (right). The extraction-time dependence of the beam energy is corrected in these histograms for the evaluation of the resolution in the main measurements. Each peak is fitted by a Gaussian peak with a second-order polynomial background function, as indicated by the red curves.

4.5.5 Systematic error of calculated missing mass

We consider three sources of systematic errors in the missing-mass calculation as listed in Table 4.5. Firstly, a contribution from the stability of the optics calibration is evaluated to be 0.5 MeV/c^2 based on the systematic error of 0.7 mm in the optics-corrected horizontal position. Secondly, a systematic error originating from uncertainties of the absolute beam energies is evaluated to be 1.4 MeV/c^2 in Appendix A. In this evaluation, the error for the calibration momentum $P_{\mathrm{calibration}}$, which is originating from the error of the 1.6 GeV beam energy, is included. Thirdly, a reaction angle is neglected in the analysis. This affects the evaluation of the deuteron momentum in the calibration measurements by about 0.03% assuming a reaction angle up to 1°. This contribution corresponds to 0.8 MeV/c^2 for the missing mass. Finally, a total systematic error is estimated to be 1.7 MeV/c^2 by taking the square root of the quadratic sum of all the contributions.

TABLE 4.5: Evaluated systematic errors for the missing mass are listed.

Source of systematic error	Evaluated error
Ion-optics calibration	0.5 MeV/c^2
Calibration of the beam energies	1.4 MeV/c^2
Neglecting reaction angles	0.8 MeV/c^2
Total	1.7 MeV/c^2

4.6 Analysis of Beam Intensity

4.6.1 Calibration of SEETRAM detector

We performed dedicated measurements to calibrate the SEETRAM detector for the 2.5 GeV proton beam. Since SEETRAM has almost no sensitivity for a proton beam with an intensity less than 1 MHz, it is not possible to calibrate this detector in a single measurement. Therefore, two measurements were carried out to first relate the response of the SEETRAM detector to the number of scattered particles off the thick carbon target, and then relate it to the number of beam particles in a measurement with a lower intensity.

The left-top panel in Figure 4.16 shows a correlation between the SEETRAM counts per spill and the number of scattered particles counted by SC02 obtained in the first measurement with the higher intensity. The slope is evaluated to be $(2.72 \pm 0.02) \times 10^{-3}$ as shown by the red line. The error is estimated from a histogram of the slope between each point and an estimated offset point shown in the right-top panel. We take the width (σ) of this slope histogram as the error of the evaluated slope.

In the second measurement, the lower intensity proton beam was delivered to the F2 area. The number of the beam particles were directly counted by SC2H at F2, and the scattered particles from the target were counted by SC02 at the same time. The left-bottom panel of Figure 4.16 shows an obtained correlation between these counts per spill. The slope is evaluated to be $(2.55 \pm 0.14) \times 10^{-4}$, where the error is similarly estimated from the slope histogram shown in the right-bottom panel.

By combining the results in the two measurements, the SEETRAM count can be converted to the absolute number of the protons. Since the gain of the SEETRAM was increased by a factor of 10 only during this calibration, the number of the protons for 1

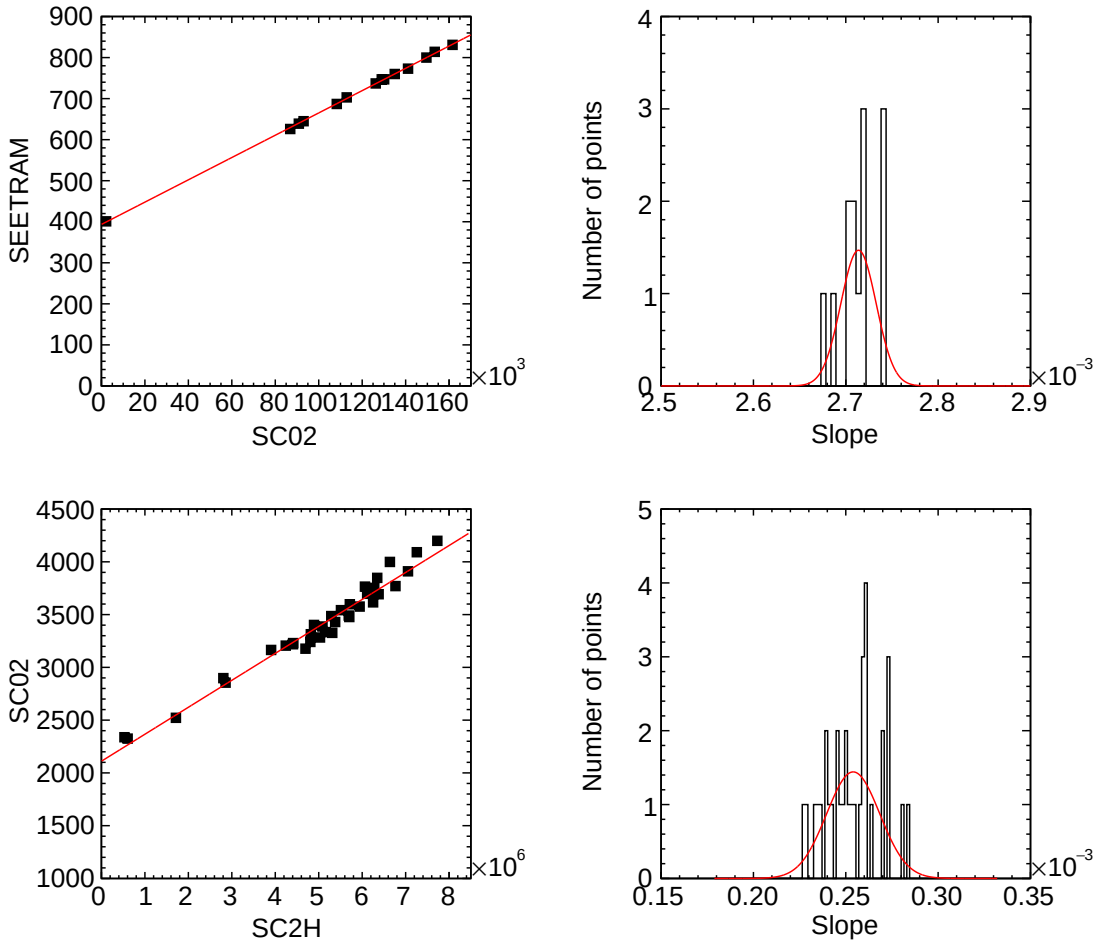

FIGURE 4.16: Intensity calibration of SEETRAM via the SC02 counts. A correlation between the SEETRAM and SC02 counts (top-left) and a fluctuation of the slope (top-right) obtained in the first measurement are shown. Similarly, a correlation between the SC02 and SC2H counts (bottom-left) and a fluctuation of the slope (bottom-right) are shown for the second measurement. The SEETRAM counts have an offset due to a positive offset applied to the current digitizer. The offset seen for SC02 is due to the dark counts of the photomultiplier.

SEETRAM count in the standard setting is obtained as follows.

$$\begin{aligned} 1\,\text{SEETRAM} &= 10 \times (1 \text{ SEETRAM in the calibration}) \\ &= \frac{10}{(2.72 \pm 0.02) \times 10^{-3} \times (2.55 \pm 0.14) \times 10^{-4}} \text{ protons} \\ &= (1.44 \pm 0.08) \times 10^{7} \text{ protons} \end{aligned} \tag{4.16}$$

The validity of this calibration is confirmed by evaluating a differential cross section of the proton-deuteron elastic scattering at 2.5 GeV in Section 4.7.1.

4.6.2 Calibration of SC01

The response of SC01 is calibrated as well for both the thick carbon target and CD_2 target in order to monitor the beam intensity during the main measurements. Short production and reference measurements with SEETRAM are analyzed, and obtained relations between

the SEETRAM counts and the SC01 counts per spill are shown in Figure 4.17. Both the graphs are fitted by quadratic functions. The obtained relations are used to estimate the beam intensity during the main measurements.

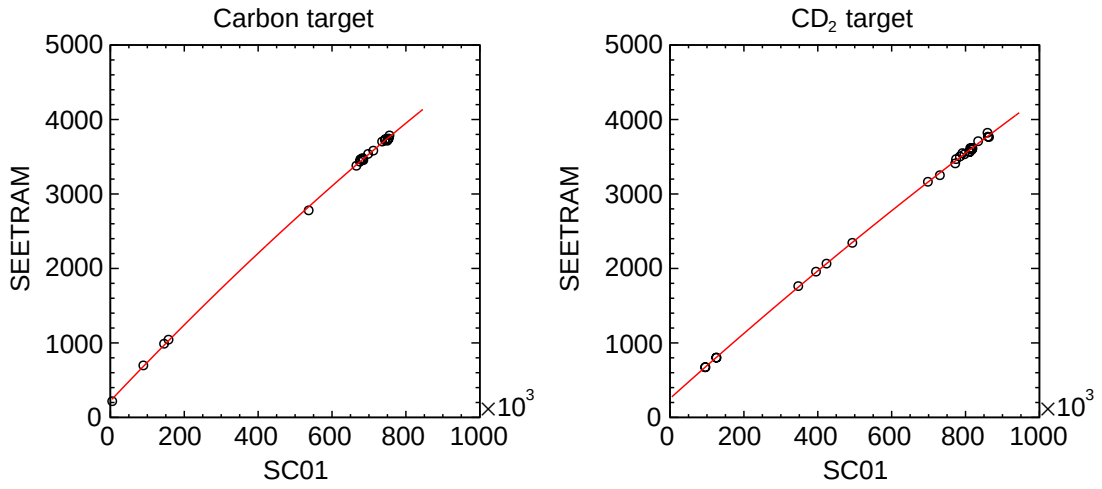

FIGURE 4.17: Correlations between the SC01 counts and the SEETRAM counts per spill for the 4115 mg/cm^2-thick carbon target (left) and the 4022 mg/cm^2-thick CD_2 target (right). These graphs are fitted by quadratic functions, as shown by the red curves.

4.7 Normalization of Cross Section

4.7.1 Cross section of proton-deuteron elastic scattering at 2.5 GeV

We evaluate a differential cross section of the $d(p,d)p$ elastic backward scattering at a proton energy of 2.5 GeV in this section. We compare the obtained cross section with data reported in Berthet *et al.* [47] for confirmation of the analysis method.

The measurements of the elastic scattering at 2.5 GeV were performed with three settings for the slits in the target region, as listed in Table 4.6. The solid angle $\Delta\Omega_{\rm lab}$ was limited by the FRS in the first measurement and by the slit positions in the second and third measurements. Thus, the differential cross section can be evaluated from the second and the third measurements. The first measurement is then used to estimate the solid angle covered by the FRS.

TABLE 4.6: Experimental conditions in the measurements of the proton-deuteron elastic backward scattering at T_p = 2.5 GeV. In run Nos. 640 and 641, horizontal(H) and vertical(V) slits placed downstream of the reaction target were used to limit the solid angle.

Run No.	CD_2 target thickness [mg/cm^2]	Slit position [mm(H) × mm(V)]	Solid angle ($\Delta\Omega_{\rm lab}$) [sr]
639	4022 ± 9	no slit	FRS acceptance
640	4022 ± 9	± 9.9(H) ± × 3.2(V)	3.94 ×10^{-5}
641	4022 ± 9	± 7.0(H) × ± 2.7(V)	2.35 ×10^{-5}

Figure 4.18 shows obtained optics-corrected position spectra in the measurements. Peaks of the elastic scattering are observed with continuous background by the reactions with carbon in the CD_2 target. The yield of each elastic peak is evaluated as follows. First, we sum up the number of events in an integral region defined by the red dashed lines. Next,

the contribution from the continuum is estimated by a fitting in side-band regions shown by the blue points. We fit these points by a quadratic function, and evaluate the background contribution in the integral region.

The differential cross section $\left(\frac{\mathrm{d}\sigma}{\mathrm{d}\Omega}\right)_{\mathrm{lab}}$ is evaluated by using the following equation.

$$\left(\frac{\mathrm{d}\sigma}{\mathrm{d}\Omega}\right)_{\mathrm{lab}} = \frac{Y}{N_p \cdot n_d \cdot \Delta\Omega_{\mathrm{lab}} \cdot \varepsilon}, \tag{4.17}$$

where Y is the yield of the elastic peak, N_p is the total number of protons injected on to the CD_2 target, which is evaluated by analysis of the SEETRAM detector, and n_d is the number density of the target. ε represents the overall efficiency of the data acquisition and analysis. Evaluated values for the right-hand side of Equation (4.17) are summarized in Table 4.7.

TABLE 4.7: Evaluated values for the calculation of the differential cross section of the elastic scattering at 2.5 GeV. These values are used in the right-hand side of Equation (4.17). Numbers in parentheses are estimated errors .

Run No.	Y	N_p	n_d [cm^{-2}]	$\Delta\Omega_{\mathrm{lab}}$ [sr]	ε
639	$1.34(3) \times 10^4$	$6.25(35) \times 10^{12}$	3.022×10^{23}	$\Delta\Omega_{\mathrm{lab,ref}}$	0.958
640	565(69)	$7.65(42) \times 10^{12}$	3.022×10^{23}	3.94×10^{-5}	0.988
641	441(54)	$9.98(55) \times 10^{12}$	3.022×10^{23}	2.35×10^{-5}	0.949

The differential cross section is calculated using Equation (4.17) with the values listed in Table 4.7. By combining the second and third measurements for the statistical errors, we obtain the cross section as

$$\left(\frac{\mathrm{d}\sigma}{\mathrm{d}\Omega}\right)_{\mathrm{lab}} = 6.4 \pm 0.6\,(stat.) \pm 0.4\,(syst.)\ \mu\mathrm{b/sr}. \tag{4.18}$$

This corresponds to

$$\left(\frac{\mathrm{d}\sigma}{\mathrm{d}\Omega}\right)_{\mathrm{cm}} = 0.98 \pm 0.09\,(stat.) \pm 0.06\,(syst.)\ \mu\mathrm{b/sr}. \tag{4.19}$$

in the center of mass frame.

This result is compared with the values reported in Berthet *et al.* [47] Figure 4.19 summarizes the differential cross sections in the center of mass frame as a function of the proton energy. The closed circle shows the value we obtained in this section, while the open circles show the data by Berthet *et al.* [47] The error bars show only the statistical errors for both the data sets. There are additional systematic errors of ±6% for the closed point and ±8% for the open points. Our value is consistent with the known data within the experimental errors. Therefore, we can confirm the correctness of the cross-section analysis including the intensity calibration.

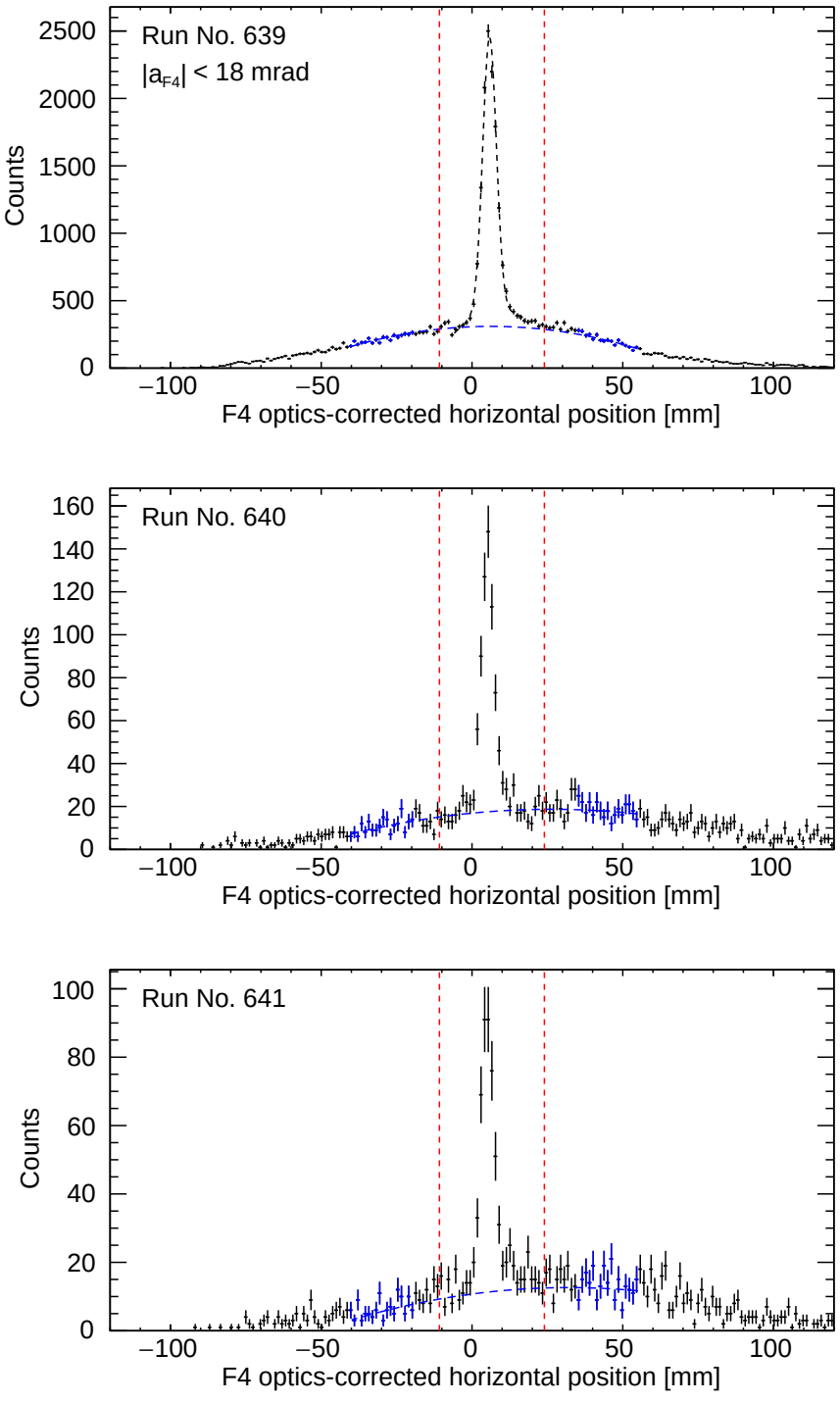

FIGURE 4.18: Obtained spectra of the proton-deuteron elastic backward scattering at 2.5 GeV. The measurement conditions are summarized in Table 4.6. The red dashed lines indicate integral regions for counting the yields. The blue points are used for side-band fitting of the continuous background, and the blue dashed curves show the estimated background.

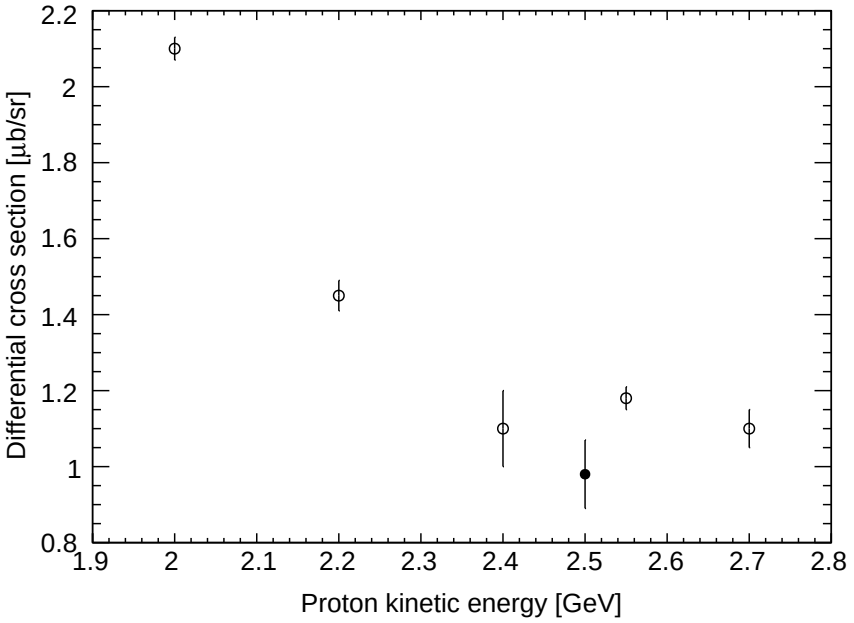

FIGURE 4.19: Comparison of differential cross sections of the proton-deuteron backward elastic scattering in the center of mass frame. The closed circle shows the cross section obtained in the present analysis, while the open circles show those by Berthet *et al.* [47] Error bars indicate only the statistical errors for both the data sets. There are additional systematic errors of ±6% for the closed circle and ±8% for the open circles.

4.7.2 Normalization of ^{12}C(p,d) and CD$_2$(p,d) spectra

Absolute normalization of double differential cross sections of the ^{12}C(p,d) and CD$_2$(p,d) reactions are considered using short data sets with the SEETRAM detector. Each spectrum is normalized at one reference point which corresponds to the peak position of the proton-deuteron elastic scattering, discussed in Section 4.7.1. As the solid angle in the FRS acceptance is deduced at this point, the absolute normalization of the spectra can be done independently of an acceptance correction discussed in Section 4.8.

The solid angle $\Delta\Omega_{\mathrm{lab,ref}}$ limited by the FRS is evaluated from the elastic-peak measurement without the slits in the target area, shown in the top panel of Figure 4.6. By using the evaluated cross section in Equation (4.18) and the values in Table 4.7, we obtain $\Delta\Omega_{\mathrm{lab,ref}} = (1.16 \pm 0.13) \times 10^{-3}$ sr at the optics-corrected position of $x_{\mathrm{ref}} = 5.8$ mm. This solid angle includes the selection of the horizontal angles at F4 smaller than 18 mrad applied to the top spectrum in Figure 4.6. We use this solid angle for the normalization of the main spectra under the same cut condition.

The normalization of the double differential cross section is given at $E_{\mathrm{ex}} - E_0 = E_{\mathrm{ref}}$, corresponding to the reference position x_{ref}, by the following equation:

$$\left(\frac{\mathrm{d}^2\sigma}{\mathrm{d}\Omega \mathrm{d}E}\right)_{\mathrm{lab},\, E_{\mathrm{ex}} - E_0 = E_{\mathrm{ref}}} = \left(\frac{\mathrm{d}Y}{\mathrm{d}x}\right) \cdot \left(\frac{\mathrm{d}x}{\mathrm{d}E}\right) \cdot \frac{1}{N_p \cdot n \cdot \Delta\Omega_{\mathrm{lab,ref}} \cdot \varepsilon}. \tag{4.20}$$

$(\mathrm{d}Y/\mathrm{d}x)$ is the density of the yield at x_{ref} in the position spectrum, and $(\mathrm{d}x/\mathrm{d}E)$ is given by a kinematics calculation. N_p, n, and ε are the number of protons, the number density of the target, and the overall efficiency, respectively.

Obtained spectra in the production and reference measurements with SEETRAM are shown in Figure 4.20. Histograms of the optics-corrected positions are plotted for identified deuteron events under the selection of the horizontal angles at F4 smaller than 18 mrad. The yield densities at the reference point x_{ref} are estimated by fitting the histograms by second-order polynomial functions around x_{ref}.

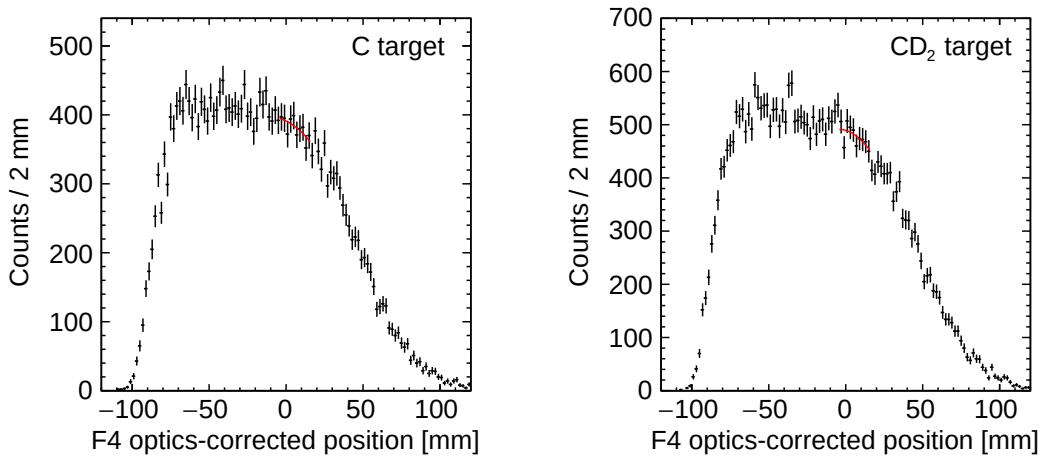

FIGURE 4.20: Position spectra obtained in the short measurements for the cross-section normalization. The left panel shows the production measurement, and the right panel shows the reference measurement. The red curves are fitted quadratic functions for evaluation of yield densities at the reference position of $x_{\mathrm{ref}} = 5.8$ mm.

Evaluated values for the right-hand side of Equation (4.20) are summarized in Table 4.8. E_{ref} and $(\mathrm{d}x/\mathrm{d}E)$ are calculated by kinematics calculations, N_p is deduced by the SEETRAM analysis, and n is calculated from the target thickness. For the overall efficiency ε, the DAQ efficiency, the efficiency of the deuteron identification, and the tracking efficiency are included. Finally, we obtain the double differential cross sections of 5.4 ± 0.7 μb/(sr·MeV) for the ^{12}C(p,d) reaction and 9.4 ± 1.2 μb/(sr·MeV) for the CD_2(p,d) reaction at the reference energy E_{ref}, as listed in the last line of Table 4.8.

TABLE 4.8: Evaluated values for the absolute normalization of the ^{12}C(p,d) and CD_2(p,d) spectra.

	C target	CD_2 target
E_{ref} [MeV]	-7.0	-7.2
$(\mathrm{d}Y/\mathrm{d}x)$ [mm^{-1}]	192 ± 5	241 ± 5
$(\mathrm{d}x/\mathrm{d}E)$ [mm/MeV]	1.57	1.57
Number of protons N_p	$(0.93 \pm 0.05) \times 10^{12}$	$(1.09 \pm 0.06) \times 10^{12}$
Target density n [cm^{-2}]	2.065×10^{23}	1.511×10^{23}
$\Delta\Omega_{\mathrm{lab,ref}}$ [sr]	$(1.16 \pm 0.13) \times 10^{-3}$	$(1.16 \pm 0.13) \times 10^{-3}$
Overall efficiency ε	0.252	0.211
$\left(\frac{\mathrm{d}\sigma^2}{\mathrm{d}\Omega \mathrm{d}E}\right)_{\mathrm{lab},\ E_{\mathrm{ex}}-E_0=E_{\mathrm{ref}}}$ [μb/(sr·MeV)]	5.4 ± 0.7	9.4 ± 1.2

4.8 Acceptance Correction

A correction for the momentum acceptance of the FRS is necessary to obtain the overall cross-section spectrum. This is because a measured momentum distribution is always affected by the momentum acceptance of the spectrometer. This acceptance can be expressed as a function of the relative momentum deviation δ in the spectrometer. Thus, by comparing measurements with different FRS scale factors at a same momentum region, we can estimate the acceptance shape of the FRS.

In the analysis of the production and reference measurements, we select events with the horizontal angles at F4 smaller than 18 mrad in order to have a flat acceptance shape. The left panel of Figure 4.21 shows histograms of the optics-corrected horizontal positions at F4 without the angular selection in black and with the selection in red. Although the number of the events is reduced by the selection, a wider region can be used for analysis without dealing with the round-shape acceptance. The right panel of Figure 4.21 shows a two-dimensional histogram of the corrected horizontal positions and angles at F4. Events near the edge of the acceptance are rejected by the selection of the F4 angle, and the straight acceptance shape is realized.

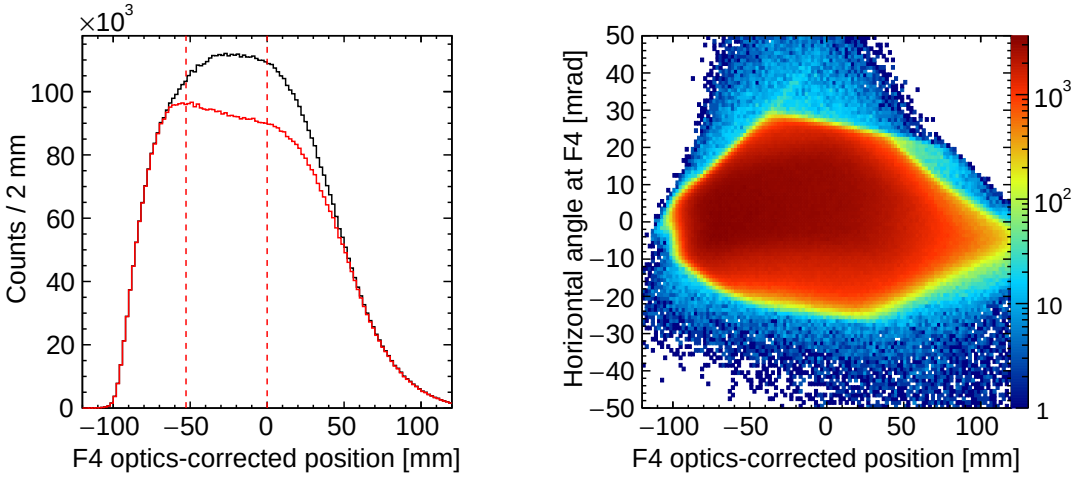

FIGURE 4.21: Selection of the horizontal angle at F4 is explained. The left panel shows optics-corrected horizontal positions at F4. The right panel shows two dimensional histograms of the corrected horizontal position and angle at F4. Events near the edge of the acceptance can be removed by the selection of horizontal angle.

Next, we evaluate the acceptance function under the selection of the horizontal angle. Since the histogram is well fitted by a linear function between the red dashed lines in the left panel of Figure 4.21, we assume a linear function for the acceptance as $A(\delta) = 1 + a_1\delta = 1 + a_1 x_c/(x|\delta)$ in the corresponding region of $0\% \leq \delta \leq 1.5\%$.

The slope parameter a_1 is deduced from the data sets of the reference measurements. We compare measured momentum distributions normalized by estimated intensities for different scale factors of the FRS. A ratio of the counts between two scale factors at a common deuteron momentum gives a ratio of the acceptance between two different relative momenta of the spectrometer. This can be written as

$$\frac{H_j(P)}{H_i(P)} = \frac{A(\frac{P}{P_0 f_j} - 1)}{A(\frac{P}{P_0 f_i} - 1)} \simeq 1 + a_1(f_i - f_j), \tag{4.21}$$

where $H_i(P)$ and $H_j(P)$ are the normalized counts at a momentum P with scale factors of f_i and f_j, respectively. The momentum P corresponds to the relative momentum deviations of $\delta = \frac{P}{P_0 f_i} - 1$ for f_i and $\delta = \frac{P}{P_0 f_j} - 1$ for f_j. Then the ratio of the counts $H_j(P)/H_i(P)$ gives the slope parameter a_1.

The measured momentum distributions normalized by the estimated intensities are shown in the left panel of Figure 4.22. The five data sets are plotted in different colors, as explained in the caption of the figure. The spectra are relatively normalized by

$$\sum(\text{estimated beam intensity by SC01}) \cdot (\text{overall efficiency}). \tag{4.22}$$

Then we take ratios between two adjacent scale factors in their overlap region and fitted by Equation (4.21) to extract the slope parameter. Such analysis is repeated for all the four combinations of the neighboring scale factors. The obtained slope values are summarized in the right panel of Figure 4.22. The error bars only include the statistical errors, and additional uncertainties originating from the normalization are estimated to be of the order of 5%. By taking the region including all the four points, we evaluate the slope parameter to be $a_1 = (0.07 \pm 0.03)\,\%^{-1}$. This value is consistent with one estimated by a Monte Carlo simulation program MOCADI [52], in which beam transportation is simulated with given transfer matrices and apertures of the optical elements.

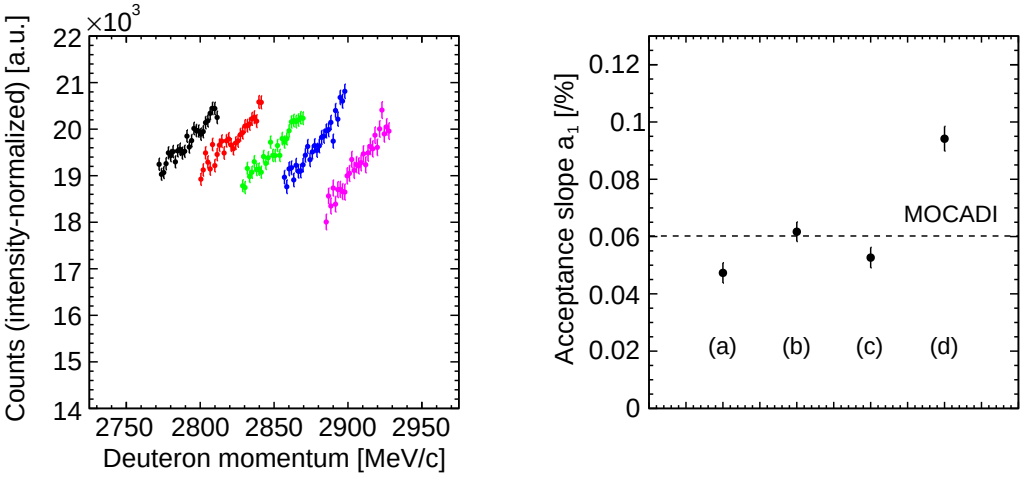

FIGURE 4.22: Evaluation of the slope of the momentum acceptance is explained. The measured momentum distributions normalized by the estimated intensities are shown in the left panel for Ref0980(black), Ref0990(red), Ref1000(green), Ref1010(blue), and Ref1020(magenta). The evaluated slope a_1 is shown in the left panel. The four points correspond to results by taking ratios of Ref0980/Ref0990(a), Ref0980/Ref0990(b), Ref0980/Ref0990(c), and Ref0980/Ref0990(d). The dashed line shows an estimated value by the MOCADI simulation.

4.9 Excitation-Energy Spectra

4.9.1 Spectra of the production measurements

Excitation-energy spectra of the production measurements are discussed in this section. The analysis consists of the following procedures:

- Excitation-energy distributions are plotted for all the data sets. Each histogram is normalized by the estimated intensity with the SC01 counts.
- The acceptance correction is made for the straight acceptance region.
- Relative normalization is adjusted to achieve smooth connection between the data sets.
- Averaging the data sets at every energy bin.
- Absolute normalization of the double differential cross section at the reference point.

The top panel of Figure 4.23 shows obtained distributions of the excitation energy $E_{\rm ex} - E_0 = (M_{^{12}{\rm C}(p,d)X} - M_{^{11}{\rm C}} - M_{\eta'})c^2$ for all the production measurements. The eight data sets are plotted in different colors, as explained in the caption of the figure. Each histogram is normalized by the estimated intensity with SC01, as in Equation (4.22). In these histograms, events with the horizontal angles at F4 smaller than 18 mrad are selected in order to obtain the straight acceptance region ($0\% \leq \delta \leq 1.5\%$). The straight acceptance regions are selected and plotted in the middle panel of Figure 4.23.

Next, the acceptance correction discussed in Section 4.8 is applied to the spectra; for every data point in the middle panel of Figure 4.23, the relative momentum deviation in the spectrometer δ is calculated for its central energy, and then the height and the error are scaled by $A^{-1}(\delta)$. The corrected spectra are given in the bottom panel of Figure 4.23.

The acceptance-corrected spectra show gaps between the data sets. These are due to the uncertainties in the normalization of the effective intensities by SC01, which are of the order of 5%. Since the different data sets should smoothly overlap with each other from the physical point of view, we introduce a fine adjustment for the relative normalization as follows. In the overlap region between the two data sets, we take a ratio of one spectrum to the other, and fit the ratio spectrum with a constant function to estimate the adjustment factor for the relative normalization. Such analysis is performed for all the combinations of the two neighboring spectra. The spectra with this fine adjustment are shown in the top panel of Figure 4.24.

Finally, a combined spectrum is obtained by averaging the different data sets at every energy bin and applying the absolute normalization at the reference energy, as discussed in Table 4.8. The obtained spectrum of the double differential cross section is shown in the bottom panel of Figure 4.24. The spectra of the different data sets are well combined as seen in the figure. The overall systematic error for the absolute normalization of the double differential cross section is evaluated to be $\pm 13\%$ based on the normalization at the reference energy discussed in Section 4.7.2.

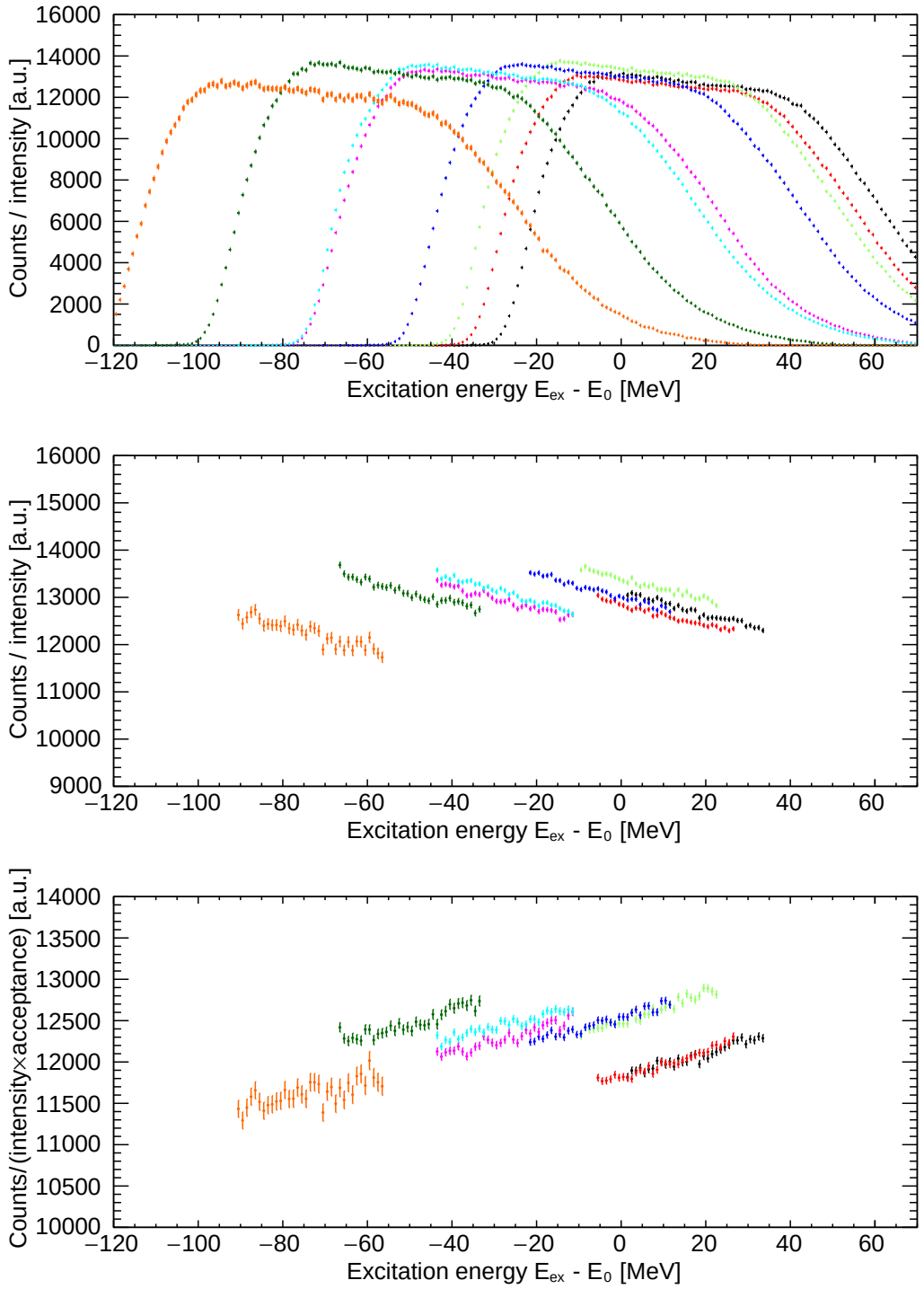

FIGURE 4.23: Analysis of the excitation-energy spectrum of the ^{12}C(p,d) reaction is explained. Histograms of the excitation energy normalized by the estimated intensities are shown (top) for all the production data sets: Prod0980 (black), Prod0983 (red), Prod0985 (light green), Prod0990 (blue), Prod1000a (magenta), Prod1000b (cyan), Prod1010 (dark green), and Prod1020(orange). The acceptance-straight regions are selected (middle), and the acceptance-corrected spectra are shown (bottom).

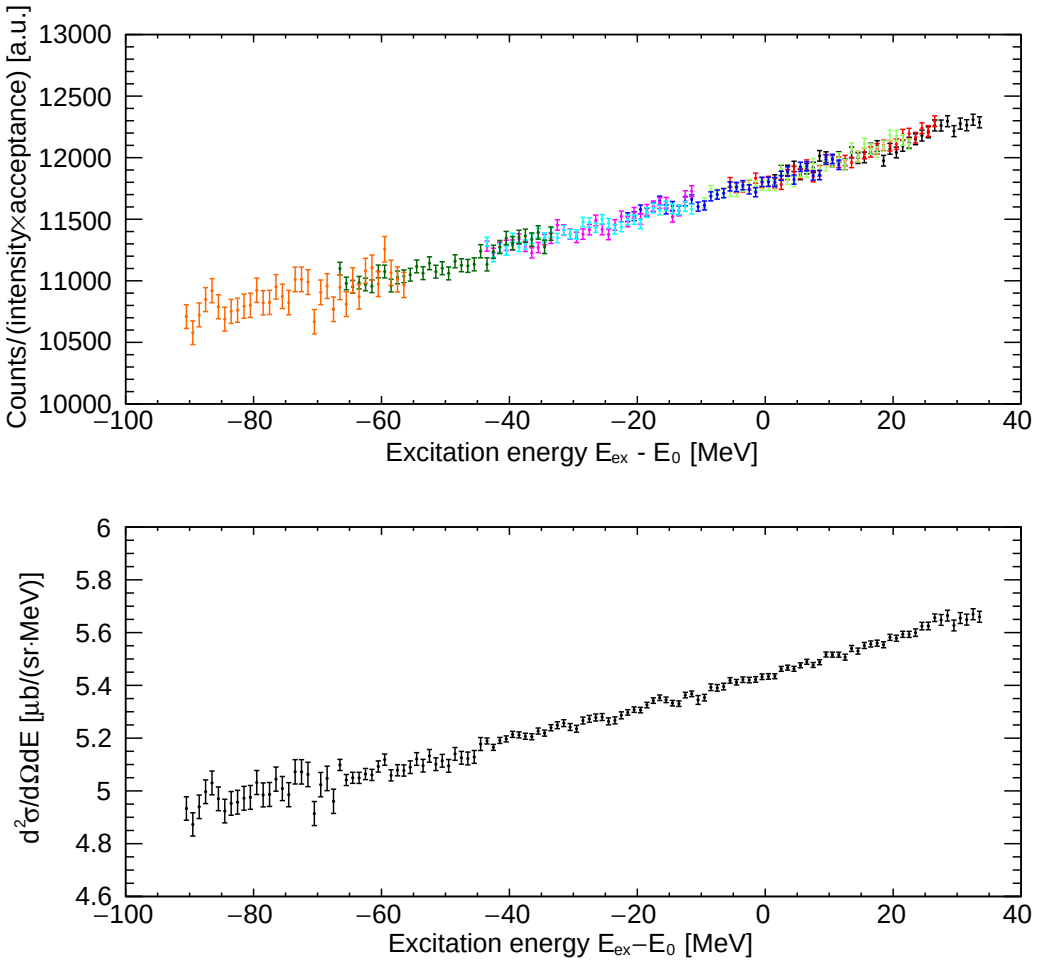

FIGURE 4.24: The excitation-energy spectrum of the ^{12}C(p,d) reaction with the adjustment of the relative normalization is given (top). The definition of the colors is the same as Figure 4.23. The combined spectrum including averaging at every bin and the absolute normalization is shown (bottom). Note that there is the overall systematic error of ±13% in the absolute normalization of the spectrum, as discussed in Section 4.7.2.

4.9.2 Spectra of the reference measurements

Spectra of the reference measurements are analyzed in an excitation energy defined as $E_{\mathrm{ex}(n)} = M_{n(p,d)X}\, c^2$, in which the missing mass is calculated for the neutron mass. This is to compare the inclusive background between the ^{12}C(p,d) and d(p,d) reactions, where dominant contributions are expected to be quasi-free processes such as $pN \to dX$.

Figure 4.25 shows obtained spectra for the reference measurements with the CD_2 target. The configuration of this figure is the same as Figure 4.23; the overall spectra normalized by the intensities estimated by SC01 are shown in the top panel, the straight-acceptance regions are selected in the middle panel, and the acceptance correction is made for the bottom panel. The definition of the used colors is listed in the caption of the figure.

The normalization factors of the intensities are relatively adjusted, similarly to the production spectra, in order to realize smooth connection between the different data sets. The adjusted spectra are shown in the top panel of Figure 4.26. By averaging the data sets at

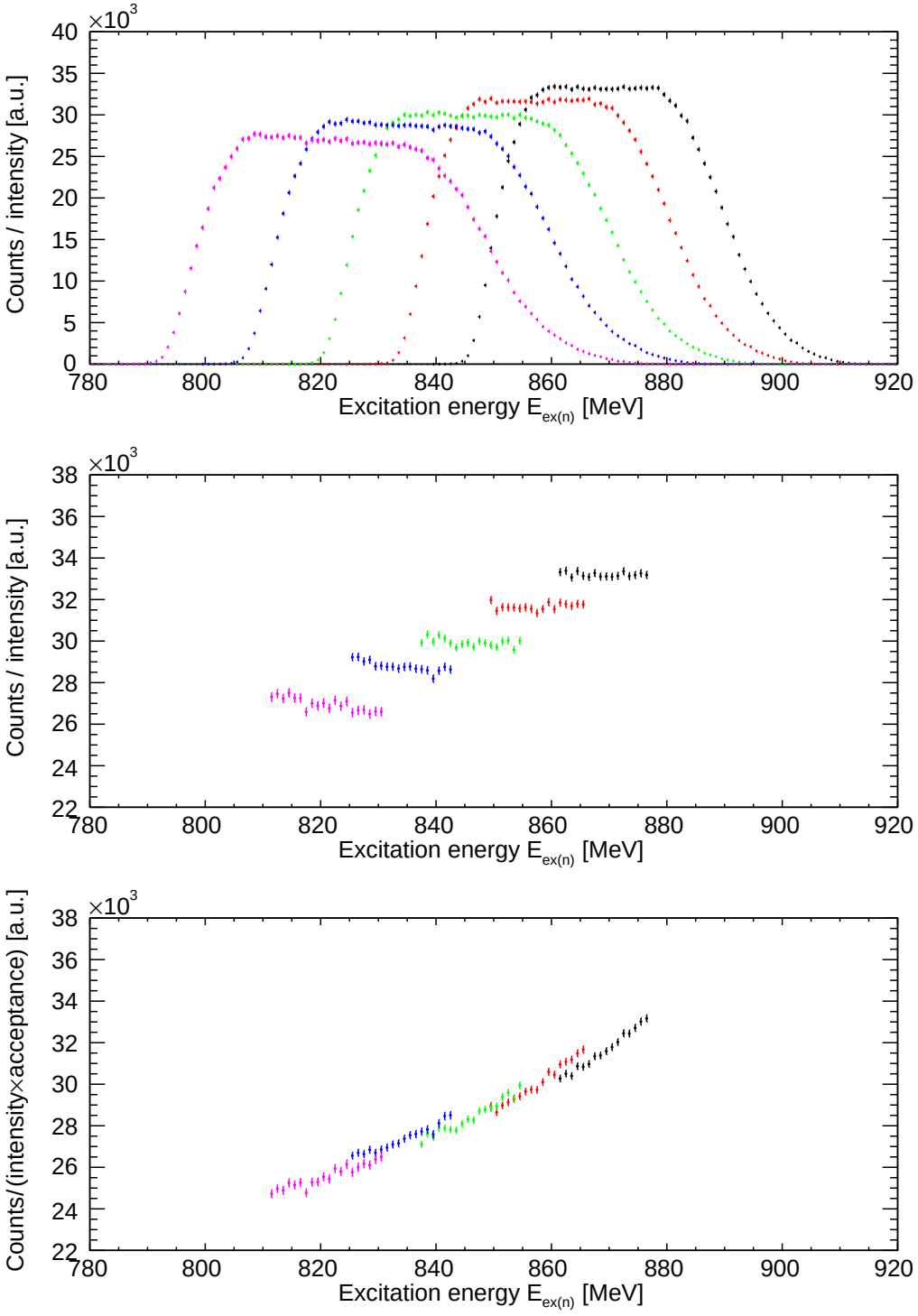

FIGURE 4.25: Analysis of the $CD_2(p,d)$ spectrum is explained. Histograms of the excitation energy normalized by the estimated intensities are shown (top) for all the reference data sets: Ref0980 (black), Ref0990 (red), Ref1000 (green), Ref1010 (blue), and Ref1020 (magenta). The acceptance-straight regions are selected (middle), and the acceptance-corrected spectra are shown (bottom).

every energy bin and applying the absolute normalization at the reference point[10] discussed in Table 4.8, a spectrum of the double differential cross section for CD_2 is obtained as shown in the middle panel of Figure 4.26. The overall systematic error of the double differential cross section for CD_2 is $\pm 13\%$ based on the error of the absolute normalization discussed in Section 4.7.2.

In order to extract the $d(p,d)$ spectrum, we need to subtract the carbon contribution from the CD_2 spectrum. The carbon contribution is evaluated with the production data, and shown by the blue graph in the bottom panel of Figure 4.26. Then, this carbon contribution is subtracted from the total CD_2 spectrum, and the remaining component is divided by two to obtain the $d(p,d)$ spectrum.

The obtained $d(p,d)$ spectrum is shown by the red graph in the bottom panel of Figure 4.26. Note that the obtained deuterium spectrum is plotted in a different scale from the carbon contribution. An excitation energy defined by $E_{\mathrm{ex}(d)} - E_0 = (M_{d(p,d)X} - M_p - M_{\eta'})c^2$, in which the missing mass is calculated with the deuteron mass, is indicated as well by the upper axis in this figure. The overall systematic error of the double differential cross section for the subtracted $d(p,d)$ spectrum is evaluated to be $\pm 19\%$ by taking into account correlated errors for the carbon spectrum and the CD_2 spectrum.

[10] The absolute normalization at the reference point given in Section 4.7 is for the excitation energy E_{ex}, in which the missing mass is calculated with the carbon mass. Thus, an additional factor $(\mathrm{d}E_{\mathrm{ex}}/\mathrm{d}E_{\mathrm{ex(n)}})$ is taken into account for the normalization in Figure 4.26.

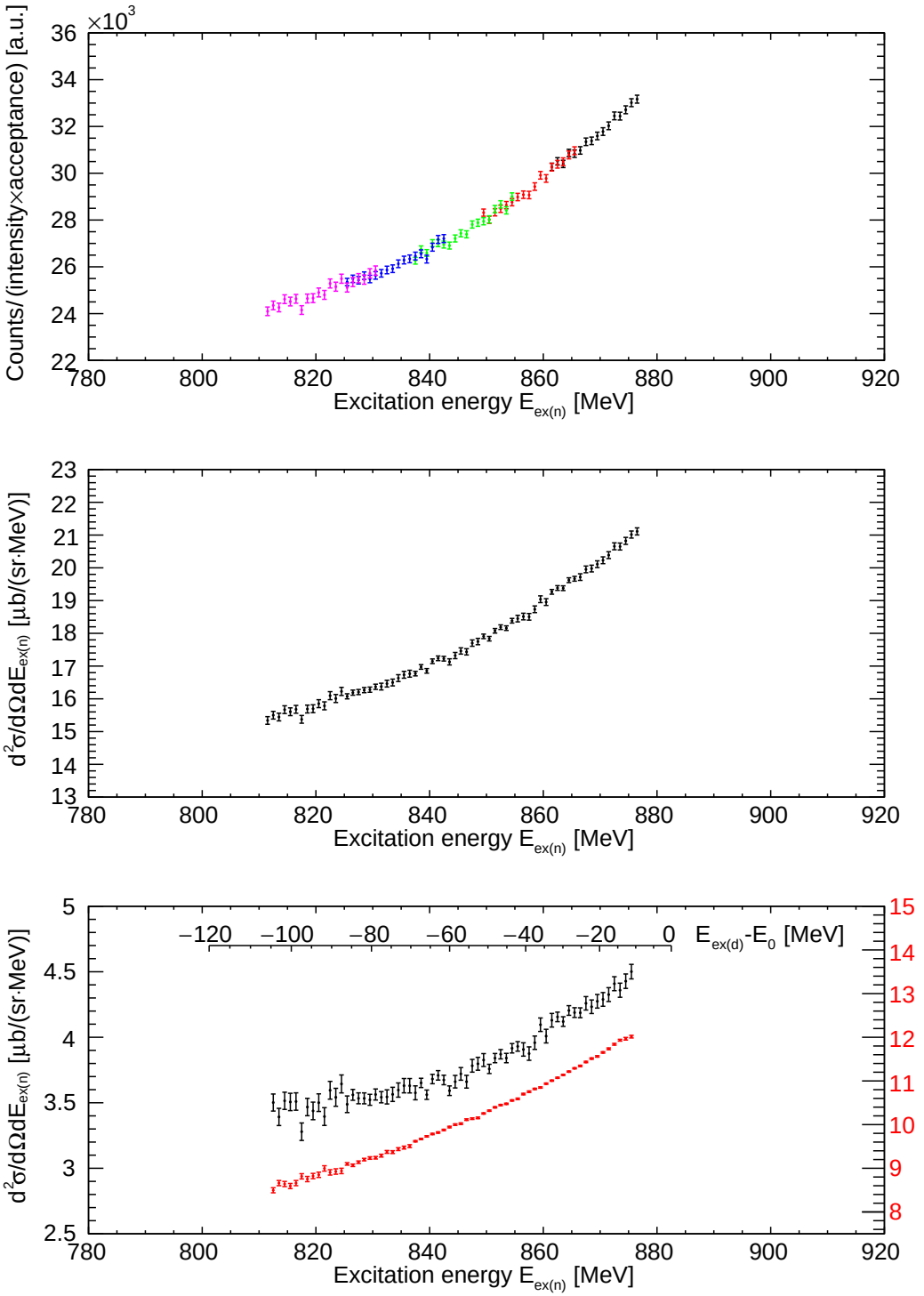

FIGURE 4.26: The $CD_2(p,d)$ spectrum with the adjustment of the relative normalization is given (top), with the colors same as Figure 4.25. The combined $CD_2(p,d)$ spectrum including averaging at every bin and the absolute normalization is shown (middle). The carbon contribution in the $CD_2(p,d)$ spectrum evaluated with the production data is shown by the red graph with the right ordinate (bottom). The obtained $d(p,d)$ spectrum by subtracting the carbon contribution is shown by the black graph with the left ordinate (bottom). The excitation energy $E_{ex(d)} - E_0$ is indicated by the upper axis. Note that there is the overall systematic error of $\pm 13\%$ in the absolute normalization of both the CD_2 spectrum and the carbon spectrum, as discussed in Section 4.7.2. The overall systematic error for the subtracted $d(p,d)$ spectrum is evaluated be $\pm 19\%$.

Chapter 5

Results and Discussion

5.1 Obtained Spectrum of the ^{12}C(p, d) Reaction

We have successfully obtained the excitation-energy spectrum of the $^{12}\mathrm{C}(p, d)$ reaction around the η' emission threshold, as shown in the bottom panel of Figure 4.23. A high statistical sensitivity at the level of better than 1% is achieved in the combined spectrum. At the same time, the experimental resolution of the excitation energy is evaluated to be 2.5 ± 0.1 MeV, which is sufficiently smaller than the expected widths of the η' mesic states.

As no clear peak structure is observed in the spectrum, we determine upper limits for the formation cross section of the η' mesic states in Section 5.2. Moreover, the obtained spectrum is directly compared with the theoretically calculated formation spectra for several sets of the η'-nucleus potential parameters in Section 5.3.

The total inclusive cross section in the obtained spectrum is about 5.4 μb/(sr·MeV) around the η' emission threshold. This value is of the same order of magnitude as our estimation based on a simulation described in Itahashi *et al.* [28]. It is also consistent with a calculation by a microscopic transport model, JAM [53], where 6–8 μb/(sr·MeV) in the region of -100 MeV $\leq E_{\mathrm{ex}} - E_0 \leq 50$ MeV is expected [54]. For the inclusive background, a comparison of the $^{12}\mathrm{C}(p,d)$ and $d(p,d)$ spectra is made in Appendix E.

5.2 Upper Limit for Formation of η' Mesic States

5.2.1 Determination of single-peak upper limit

We adopt a Voigt function in order to test a single Lorentzian peak in the spectrum. The Voigt function with a peak energy of E_{test} and a width of Γ_{test} under an experimental resolution of σ_{exp} is written as

$$\mathrm{Voigt}(E; E_{\mathrm{test}}, \Gamma_{\mathrm{test}}, \sigma_{\mathrm{exp}}) = \int_{-\infty}^{+\infty} \left(\frac{1}{2\pi} \frac{\Gamma_{\mathrm{test}}}{(E - E_{\mathrm{test}} + \varepsilon)^2 + \Gamma_{\mathrm{test}}^2/4} \right) \cdot \left(\frac{1}{\sqrt{2\pi}\sigma_{\mathrm{exp}}} \exp\left(-\frac{\varepsilon^2}{2\sigma_{\mathrm{exp}}^2} \right) \right) \mathrm{d}\varepsilon, \quad (5.1)$$

which is a Lorentzian function with E_{test} and Γ_{test} folded by a Gaussian distribution for the experimental resolution. The tested values of the peak position and width are taken from $E_{\mathrm{test}} = -60, -59, \ldots, +20$ MeV and $\Gamma_{\mathrm{test}} = 5, 10, 15$ MeV, respectively. The experimental resolution is taken to be $\sigma_{\mathrm{exp}} = 2.5$ MeV, as deduced in Section 4.5.4.

We assume a third-order polynomial for describing the inclusive background. The top panel of Figure 5.1 shows a result of fitting the spectrum only with a third-order polynomial.

The red curve is the fitted background function. χ^2/ndf of the fit is 118/124[1]. The bottom panel shows a residual plot of this fitting. The dashed lines indicate error regions of $\pm 2\sigma$ where σ is referred from the error bar of the data point at each energy. Since no significant deviations of the residues are seen, we adopt the third-order polynomial function for the background in the present analysis.

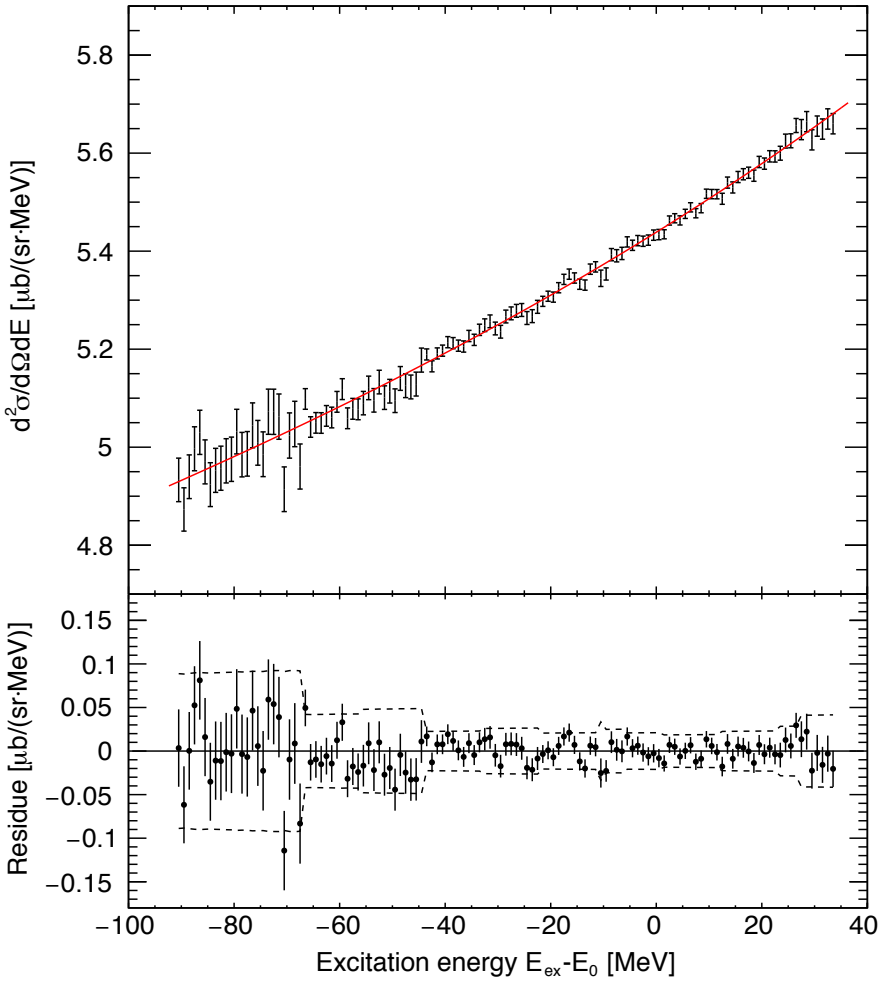

FIGURE 5.1: Fitting of the excitation-energy spectrum only with the background function. The fitting result is shown (top). Its residual plot is shown with $\pm 2\sigma$ error regions (bottom).

By combining the Voigt function and the polynomial background, we use the following $f(E)$ as a test function in the upper-limit analysis.

$$f(E) = A \cdot \mathrm{Voigt}(E; E_{\mathrm{test}}, \Gamma_{\mathrm{test}}, \sigma_{\mathrm{exp}}) + (p_0 + p_1 E + p_2 E^2 + p_3 E^3) \tag{5.2}$$

The coefficient A represents an area of the assumed peak, which stands for the differential cross section of the tested Lorentzian peak $(\mathrm{d}\sigma/\mathrm{d}\Omega)_{\mathrm{lab}}$ at $\theta = 0°$, and the upper limit of A is to be evaluated. p_0, p_1, p_2, p_3 are nuisance parameters to describe the polynomial background.

We employ a Gaussian approximation to discuss the upper limit of A. In this approach, we fit the spectrum with $f(t)$ treating both A and p_i $(i = 0, \ldots, 3)$ as fitting parameters. Then we consider a Gaussian probability density function of A with a mean of the fitted A

[1] Note that the number of degree of freedom (ndf) is slightly overestimated by about 7 due to the adjustment of the relative normalization described in Section 4.9.1.

and a standard deviation of the associated error σ_A. We consider this probability density function only in the physical region ($A \geq 0$), and determine the 95% confidence level upper limit. Since A and $p_i\,(i = 0, \ldots, 3)$ are fitted at the same time, a correlation between the parameter of interest, A, and the nuisance parameters, $p_i\,(i = 0, \ldots, 3)$, is taken into account in the present treatment. We also note that the obtained limits agree with those by the following two methods, since the likelihood function is actually well described by a Gaussian in the parameters space:

- Considering a probability density function[2] by taking a likelihood in which the nuisance parameters are optimized for every A (profiling),
- Bayesian approach with a prior distribution for A of $\pi(A) = 1$ for $A \geq 0$ and 0 for $A < 0$ and a marginalization of the nuisance parameters [55] with their uniform prior distributions, $\pi(p_i) = 1$ $(i = 0, \ldots, 3)$.

An example of the upper-limit analysis is given in Figure 5.2 for $(E_{\rm test}, \Gamma_{\rm test}) = (-5\,{\rm MeV}, 5\,{\rm MeV})$. First, the spectrum is fitted with the test function $f(E)$ as shown in the top panel. The fit region is taken as $E_{\rm test} - 35\,{\rm MeV} \leq E \leq E_{\rm test} + 35\,{\rm MeV}$. The signal component of the fitted $f(E)$ is shown by the blue curve in the middle panel, where the residual plot of the background-only fit is overlaid as a reference. Next, a probability density function is considered using the fitted value of A and its error σ_A. The solid curve in the bottom panel shows the probability density function with a horizontal axis converted into a height of the tested Lorentzian peak[3]. Then, the probability density function is normalized only in the physical region ($A \geq 0$), and a limit at 95% confidence level is deduced as indicated by the red arrow. A signal component corresponding to the obtained limit is plotted as well in the middle panel.

This upper-limit analysis is performed for all the combinations of the tested peak positions and widths taken from $E_{\rm test} = -60, -59, \ldots, +20$ MeV and $\Gamma_{\rm test} = 5, 10, 15$ MeV, respectively. Lorentzian peak heights corresponding to the fitted A with their errors σ_A are shown by the blue graphs, while those for the evaluated limits are shown by the red lines in Figure 5.3.

The obtained limits are summarized in Figure 5.4. The limits in the Lorentzian peak height are shown in the top panel, and those in $({\rm d}\sigma/{\rm d}\Omega)_{\rm lab}$ are shown in the bottom panel. They are plotted as functions of $E_{\rm test}$, and the colors correspond to the different tested widths $\Gamma_{\rm test}$. As a result, upper limits in the Lorentzian peak height of around 0.02 μb/(sr·MeV) are obtained near the η' emission threshold for all of $\Gamma_{\rm test} = 5, 10$, and 15 MeV. These correspond to about 0.1–0.2 μb/sr for $\Gamma_{\rm test} = 5$ MeV, 0.2–0.4 μb/sr for $\Gamma_{\rm test} = 10$ MeV, and 0.3–0.6 μb/sr for $\Gamma_{\rm test} = 15$ MeV as shown in the bottom panel of Figure 5.4.

Severe limits are obtained around the η' emission threshold, where peak structures are theoretically expected in many cases of the potential parameters shown in Figure 2.3. The obtained upper limits of around 0.02 μb/(sr·MeV) near the threshold are smaller than expected peak heights in several cases of the calculated spectra including the case of $(V_0, W_0) = (-150, -10)$ MeV, which corresponds to the in-medium mass reduction expected by the NJL model calculation [10, 11] and the width indicated by the transparency ratio measurements [20]. A quantitative comparison of the experimental spectrum with the theoretical calculations is discussed in Section 5.3.

[2] This function normalized by its maximum is shown in the bottom panel of Figure 5.2 by the open circles. There is a good agreement with the probability density function in the present analysis, shown by the solid curve.

[3] The height of the tested Lorentzian peak is expressed by $\frac{2A}{\pi\Gamma_{\rm test}}$. Note that the height of the Lorentzian peak is larger than that of the resolution-folded Voigt function, $A \cdot {\rm Voigt}(E_{\rm test}; E_{\rm test}, \Gamma_{\rm test}, \sigma_{\rm exp})$, used in the fitting function.

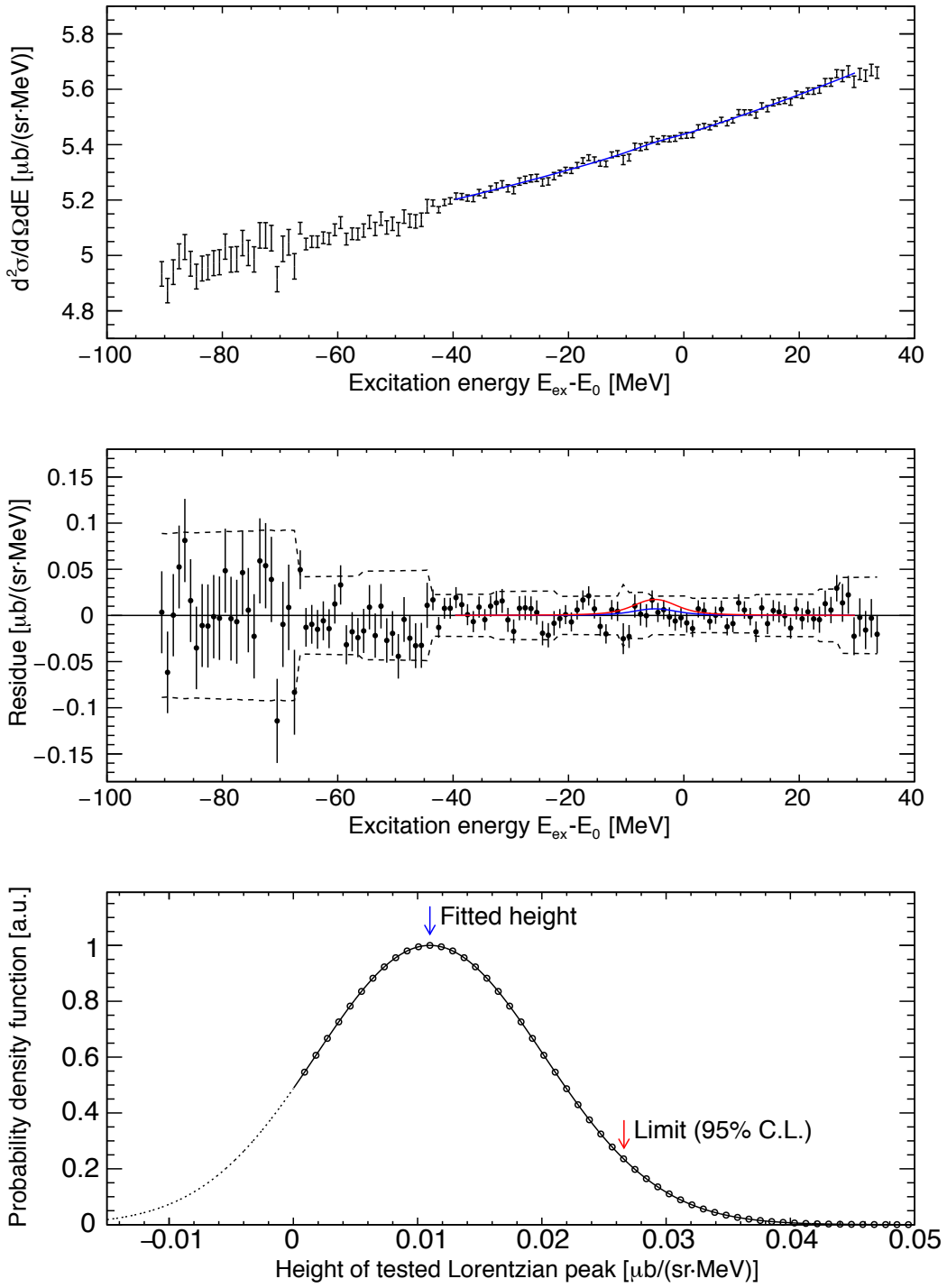

FIGURE 5.2: An upper-limit analysis for $(E_{\mathrm{test}}, \Gamma_{\mathrm{test}}) = (-5\,\mathrm{MeV},\ 5\,\mathrm{MeV})$ is explained. The spectrum fitted by $f(E)$ is shown by the blue curve (top). The signal component of the fitted $f(E)$ is shown in blue with the residual plot of the background-only fit as a reference. A signal component corresponding to the obtained limit is plotted as well (middle). The estimated probability density function is shown by the solid line, and the obtained 95% C.L. limit is indicated by the red arrow (bottom).

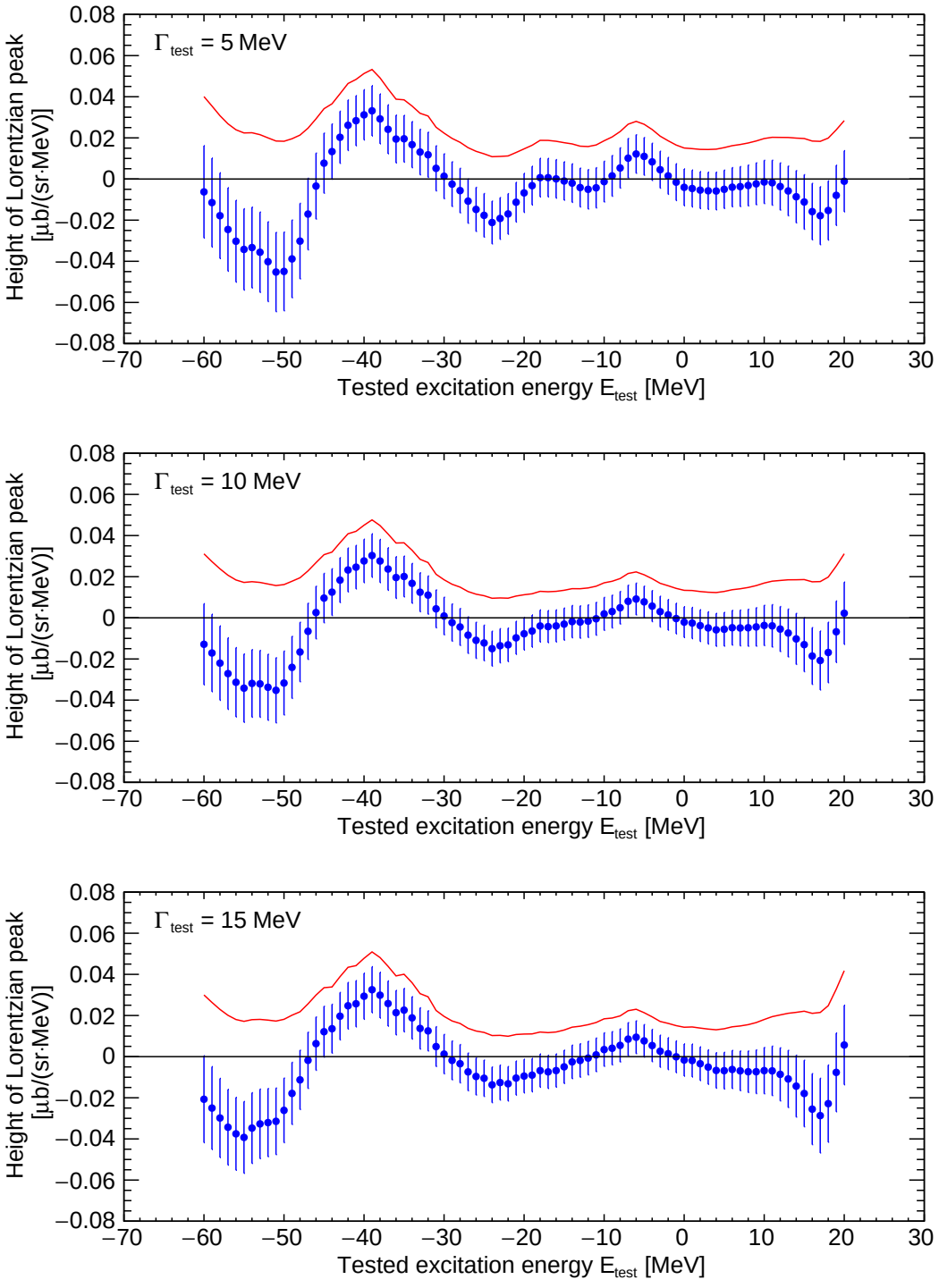

FIGURE 5.3: Fitted heights and errors of the tested Lorentzian peaks are shown by the blue graphs as functions of E_{test}. Obtained 95% C.L. upper limits for the tested Lorentzian peak height is shown by the red curves. The three panels correspond to $\Gamma_{\text{test}} = 5$ MeV (top), 10 MeV (middle), and 15 MeV (bottom).

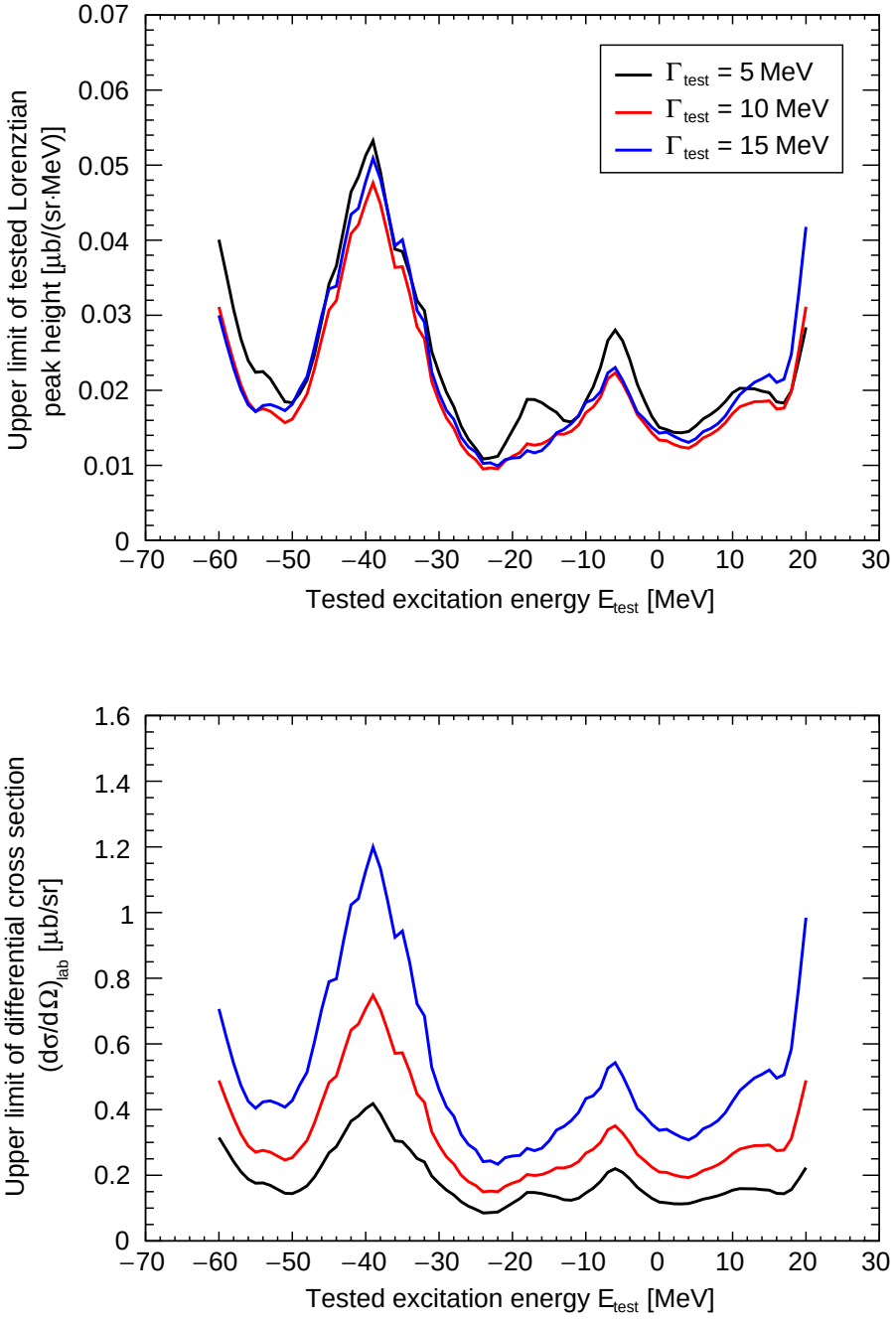

FIGURE 5.4: Obtained 95% C.L. upper limits for the formation cross section of η' mesic states are summarized as functions of E_{test}. The colors correspond to $\Gamma_{\text{test}} = 5$ MeV (black), 10 MeV (red), and 15 MeV (blue). The upper limits for the height of the tested Lorentzian peak are given in the top panel, and the upper limits for the differential cross section $(\mathrm{d}\sigma/\mathrm{d}\Omega)_{\text{lab}}$ in the bottom panel.

5.2.2 Systematic error for single-peak upper limit

Systematic errors on the obtained upper limits are discussed in this section. We consider the following sources of the systematic errors.

- systematic error on the absolute cross section of ±13% (σ_+, σ_-)
- systematic error on the missing-mass calculation of ±1.7 MeV/c^2 (M_+, M_-)
- uncertainty for the slope of the momentum acceptance of ±0.03/% (a_{1+}, a_{1-})
- systematic error on the experimental resolution of ±0.1 MeV ($\sigma_{\mathrm{exp}+}$, $\sigma_{\mathrm{exp}-}$)
- other choice of the fit region: ±30 or ±40 MeV around each E_{test} (narrow, wide)

In order to investigate the systematic errors on the obtained upper limits associated with these sources, the analysis of the upper limits is carried out by modifying each of the above conditions. The symbol in the parenthesis is used as a label for each modification.

Obtained results of the systematic errors are tabulated in Tables 5.1, 5.2, and 5.3 for the tested widths of $\Gamma_{\mathrm{test}} = 5$, 10, and 15 MeV, respectively. For each source of the systematic errors, upper limits are analyzed with the modified condition and listed for the excitation energies of every 15 MeV. The upper limits obtained in Section 5.2.1 are also shown with a label of "limit".

In the present analysis, the upper limits are determined using the averaged spectrum in the bottom panel of Figure 4.24. However, the number of degree of freedom in this spectrum is partly reduced due to the preceding adjustment of the relative intensities and averaging for the eight data sets. In order to estimate a systematic error introduced by this treatment, we analyze upper limits based on a simultaneous fitting of the eight spectra without averaging them. In this approach, the relative intensity factors are treated as free parameters, and the number of degree of freedom is correctly taken into account. The detail of this analysis is described in Appendix D. As a result, the introduced error is evaluated to be small, and therefore the validity of the present approach described in Section 5.2.1 is confirmed. The difference of the obtained limit between the present treatment and the simultaneous fitting is also included in Tables 5.1, 5.2, and 5.3 with a label of "simultaneous".

The total systematic errors are estimated by calculating root sum squares of all the contributions. The results are given in the last lines in Tables 5.1, 5.2, and 5.3. Typically, the total systematic errors are evaluated to be about 20–40%, depending on the tested energy E_{test} and width Γ_{test}.

TABLE 5.1: Systematic errors of the obtained upper limits for the Lorentzian width of $\Gamma =$ 5 MeV are listed. For the total systematic errors, root sum squares of all the contributions are calculated.

	$d\sigma_{\rm limit}/d\Omega_{\rm lab}$ [μb/sr] at $E_{\rm ex} - E_0 =$					
	-60 MeV	-45 MeV	-30 MeV	-15 MeV	0 MeV	15 MeV
limit	0.315	0.268	0.175	0.139	0.118	0.155
σ_+	0.355	0.303	0.198	0.157	0.134	0.175
σ_-	0.274	0.234	0.153	0.121	0.103	0.135
mm_+	0.384	0.202	0.233	0.147	0.142	0.159
mm_-	0.253	0.318	0.145	0.128	0.113	0.144
a_{1+}	0.300	0.273	0.149	0.155	0.119	0.153
a_{1-}	0.334	0.271	0.198	0.130	0.118	0.154
$\sigma_{\rm exp+}$	0.319	0.274	0.178	0.140	0.121	0.158
$\sigma_{\rm exp-}$	0.312	0.263	0.173	0.137	0.116	0.152
wide	0.315	0.225	0.189	0.128	0.119	0.187
narrow	0.328	0.289	0.176	0.184	0.131	0.170
simultaneous	0.322	0.264	0.178	0.169	0.108	0.157
Total	$^{+0.08}_{-0.08}$	$^{+0.07}_{-0.09}$	$^{+0.07}_{-0.05}$	$^{+0.06}_{-0.03}$	$^{+0.03}_{-0.02}$	$^{+0.04}_{-0.02}$

TABLE 5.2: Systematic errors of the obtained upper limits for the Lorentzian width of $\Gamma = 10$ MeV are listed. For the total systematic errors, root sum squares of all the contributions are calculated.

	$d\sigma_{\rm limit}/d\Omega_{\rm lab}$ [μb/sr] at $E_{\rm ex} - E_0 =$					
	-60 MeV	-45 MeV	-30 MeV	-15 MeV	0 MeV	15 MeV
limit	0.489	0.482	0.291	0.210	0.210	0.292
σ_+	0.552	0.545	0.328	0.238	0.237	0.330
σ_-	0.425	0.420	0.253	0.183	0.183	0.254
mm_+	0.615	0.370	0.406	0.201	0.240	0.293
mm_-	0.391	0.564	0.243	0.224	0.202	0.275
a_{1+}	0.461	0.491	0.247	0.234	0.213	0.293
a_{1-}	0.522	0.487	0.327	0.197	0.208	0.289
$\sigma_{\rm exp+}$	0.492	0.489	0.294	0.212	0.213	0.297
$\sigma_{\rm exp-}$	0.485	0.476	0.288	0.209	0.207	0.288
wide	0.487	0.389	0.317	0.190	0.210	0.366
narrow	0.516	0.557	0.298	0.302	0.245	0.324
simultaneous	0.510	0.475	0.295	0.250	0.190	0.302
Total	$^{+0.15}_{-0.12}$	$^{+0.13}_{-0.16}$	$^{+0.13}_{-0.08}$	$^{+0.11}_{-0.04}$	$^{+0.05}_{-0.03}$	$^{+0.09}_{-0.04}$

TABLE 5.3: Systematic errors of the obtained upper limits for the Lorentzian width of $\Gamma = 15$ MeV are listed. For the total systematic errors, root sum squares of all the contributions are calculated.

	$d\sigma_{limit}/d\Omega_{lab}$ [μb/sr] at $E_{ex} - E_0 =$					
	-60 MeV	-45 MeV	-30 MeV	-15 MeV	0 MeV	15 MeV
limit	0.706	0.790	0.461	0.305	0.337	0.521
σ_+	0.798	0.892	0.521	0.344	0.380	0.588
σ_-	0.615	0.687	0.401	0.265	0.293	0.453
mm_+	0.899	0.620	0.658	0.278	0.377	0.505
mm_-	0.563	0.905	0.392	0.348	0.329	0.502
a_{1+}	0.662	0.802	0.395	0.336	0.344	0.526
a_{1-}	0.757	0.800	0.516	0.287	0.332	0.511
σ_{exp+}	0.709	0.797	0.465	0.306	0.340	0.528
σ_{exp-}	0.706	0.782	0.457	0.303	0.334	0.514
wide	0.702	0.617	0.505	0.269	0.335	0.666
narrow	0.766	0.982	0.487	0.470	0.414	0.570
simultaneous	0.747	0.779	0.469	0.355	0.306	0.548
Total	$^{+0.23}_{-0.18}$	$^{+0.25}_{-0.26}$	$^{+0.22}_{-0.11}$	$^{+0.18}_{-0.06}$	$^{+0.10}_{-0.05}$	$^{+0.17}_{-0.07}$

5.3 Comparison with Theoretically Calculated Spectra

We compare the obtained excitation-energy spectrum with the theoretically calculated spectra in order to discuss the potential parameters (V_0, W_0). While the upper limits for the formation cross section are analyzed for the single Lorentzian peak in Section 5.2, the theoretically calculated spectra, shown in Section 2.2, have more complicated structures due to their sub-components. For this reason, it is not straightforward to quantitatively compare the obtained single-peak upper limits with the theoretically calculated spectra. Thus, in this section, we directly compare the experimental spectrum with the theoretical calculations.

The analysis procedure is similar to that for the single-peak upper limits except for the test function. We use the following test function $F(E)$ for fitting the spectrum:

$$F(E) = \mu \cdot S(E; V_0, W_0, \sigma_{\rm exp}) \ + \ (p_0 + p_1 E + p_2 E^2 + p_3 E^3). \tag{5.3}$$

$S(E; V_0, W_0, \sigma_{\rm exp})$ is the theoretically-calculated double differential cross section for the potential parameters of V_0 and W_0 folded by the experimental resolution of $\sigma_{\rm exp} = 2.5$ MeV. Figure 5.5 shows $S(E; V_0, W_0, \sigma_{\rm exp})$ for all the combinations of (V_0, W_0) described in Section 2.2 and for additionally calculated $V_0 = -80, -60$ MeV and $W_0 = -15, -10, -5$ MeV [4, 56]. The coefficient μ in Equation (5.3) is a strength parameter introduced to evaluate an allowed scale of $S(E; V_0, W_0, \sigma_{\rm exp})$ for given V_0 and W_0.

We evaluate an upper limit of μ for each fixed set of (V_0, W_0). The parameters for the background, $p_i (i = 0, \ldots, 3)$, are treated in the same way as the analysis in Section 5.2.1. Fitted values of μ and their errors are shown by the black graphs in Figure 5.6 as functions of the potential depth. The fitted values of μ are consistent with zero for all the cases of the potential parameters. Then we evaluate the upper limit for μ at 95% confidence level by considering its Gaussian probability density function in $\mu \geq 0$. The obtained limits of μ are shown by the red graphs in Figure 5.6, and summarized in Figure 5.7 as functions of the real part of the potential. Furthermore, a linearly-interpolated contour plot on the two dimensional plane of (V_0, W_0) is shown as well in Figure 5.8.

The potential parameters can be discussed base on the obtained limits for μ. If we assume the theoretically calculated cross-section spectra, then Figures 5.7 and 5.8 indicate that sets of the parameters (V_0, W_0) giving (limit of μ) < 1 are excluded at 95% confidence level. With this assumption, a large potential depth of $V_0 = -150$ MeV, which corresponds to the mass reduction of 150 MeV/c^2 at normal nuclear density predicted in the NLJ model [10], is disfavored for the considered region of the imaginary part of $(-W_0) < 20$ MeV. If we further assume 7.5 MeV $\leq (-W_0) \leq$ 12.5 MeV, as indicated by the transparency-ratio measurements [20], a region of the potential depth of $|V_0| \geq 100$ MeV is excluded.

We have achieved a good sensitivity for the deep potential case of the order of 100 MeV, as intended. On the other hand, for a shallower potential case, the obtained spectrum does not have a sufficient sensitivity, because the expected structure in the theoretical spectrum is relatively small. The potential depth of 37 MeV indicated by Nanova *et al.* [21], the mass reduction of 80 MeV/c^2 expected by the linear sigma model [18], and that of 37 MeV/c^2 by the QMC model [19] are consistent with the obtained spectrum in the above comparison.

We note that the above discussion on V_0 and W_0 depends on the theoretically calculated spectra. Particularly, it depends on the magnitude of the cross sections including the elementary cross section[4] used in the calculation. If the magnitude of the calculated spectra is twice overestimated, for example, then potential parameters (V_0, W_0) with $\mu < \frac{1}{2}$ are to

[4] There is no experimental data for the elementary cross section, as mentioned in Section 2.2. We estimate it to be 30 μb/sr, as explained in Itahashi *et al.* [28]

be excluded. However, the large mass reduction of 150 MeV/c^2 at normal nuclear density, expected in the NJL model, is still not excluded, if the magnitude of the cross section in reality is smaller than that of the theoretical calculation by a factor about four. Thus, direct data of the cross section for the elementary process $pn \to d\eta'$ are important to reduce the uncertainty of the magnitude of the calculated formation spectra and to make a better comparison between the experimental and theoretical spectra.

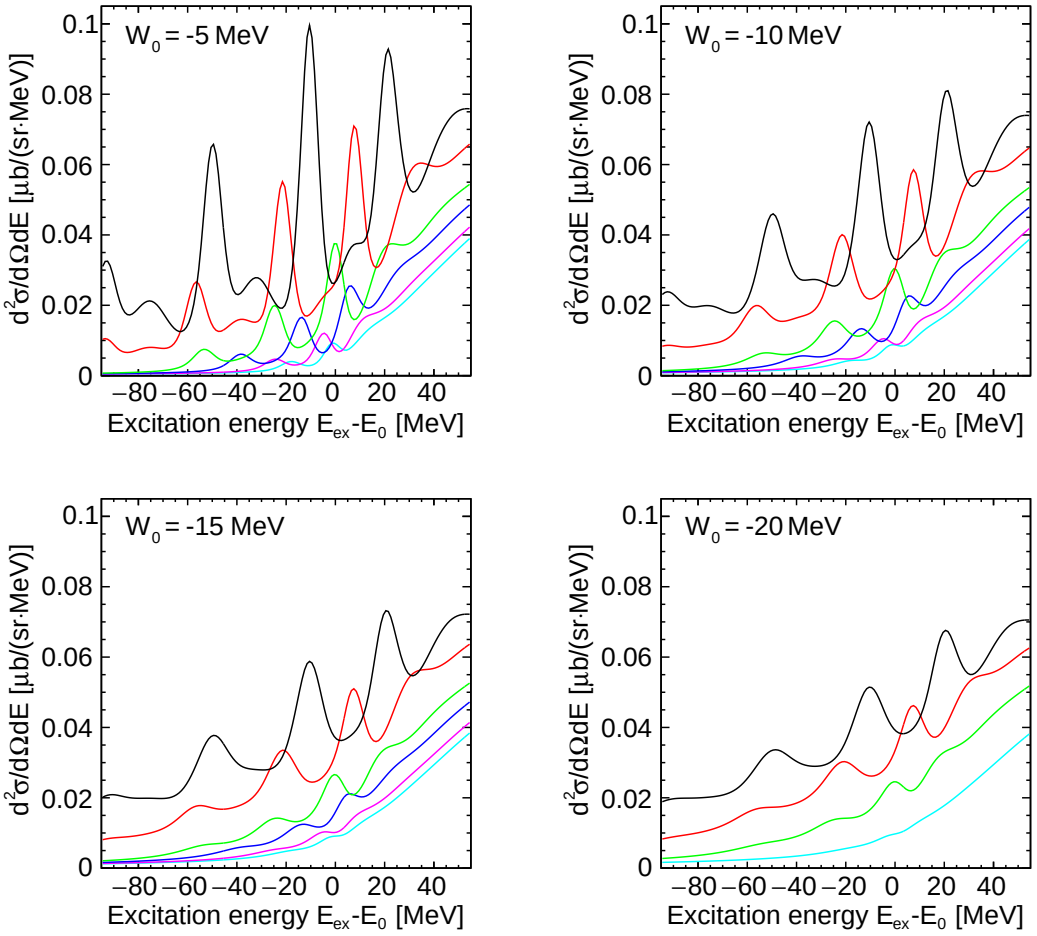

FIGURE 5.5: Theoretically-calculated spectra convoluted with the experimental resolution. The colors correspond to different assumptions of the potential depth: $V_0 = -50$ MeV (cyan), -60 MeV (magenta), -80 MeV (blue), -100 MeV (green), -150 MeV (red), -200 MeV (black). The imaginary parts of the potential are taken as $W_0 = -5$ MeV (top-left), -10 MeV (top-right), -15 MeV (bottom-left), and -20 MeV (bottom-right).

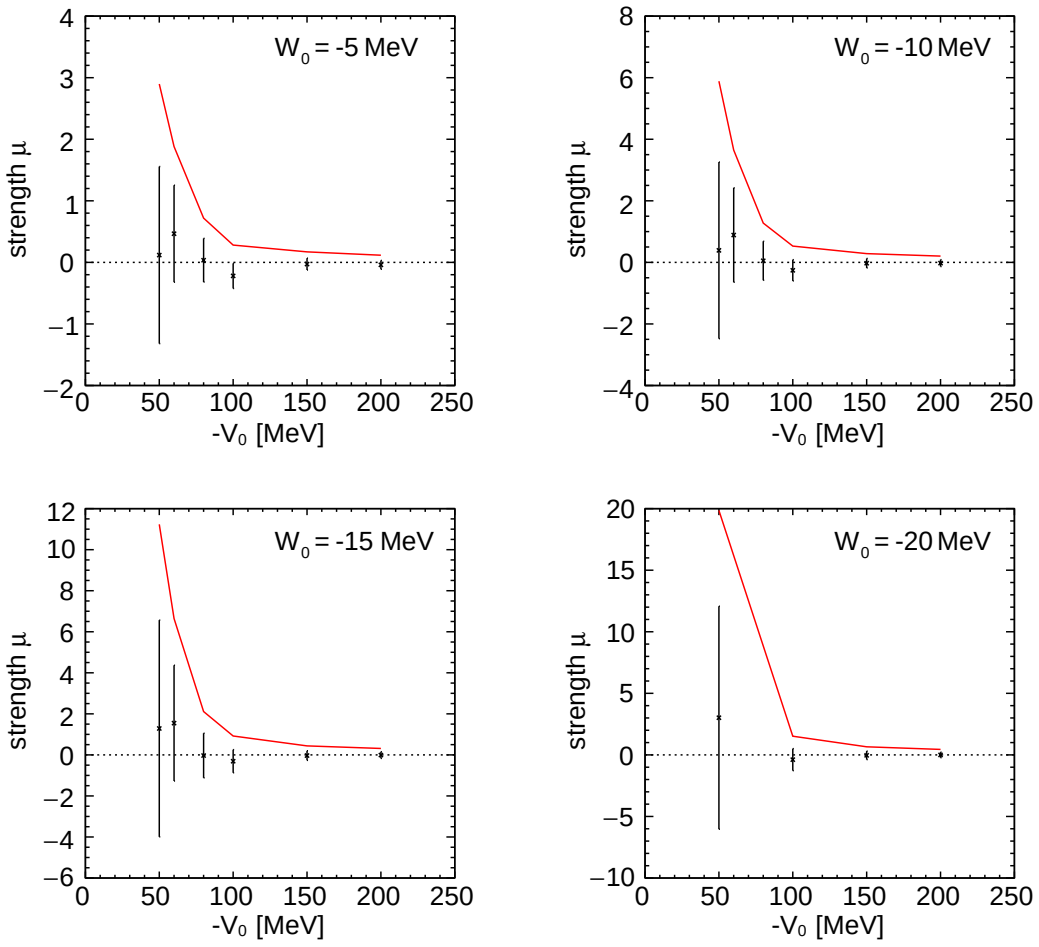

FIGURE 5.6: Fitted values and errors of the strength parameter μ are shown by the black graphs for all the combinations of the potential parameters (V_0, W_0) given in Figure 5.5. Evaluated 95% C.L. upper limits of μ are shown by the red lines.

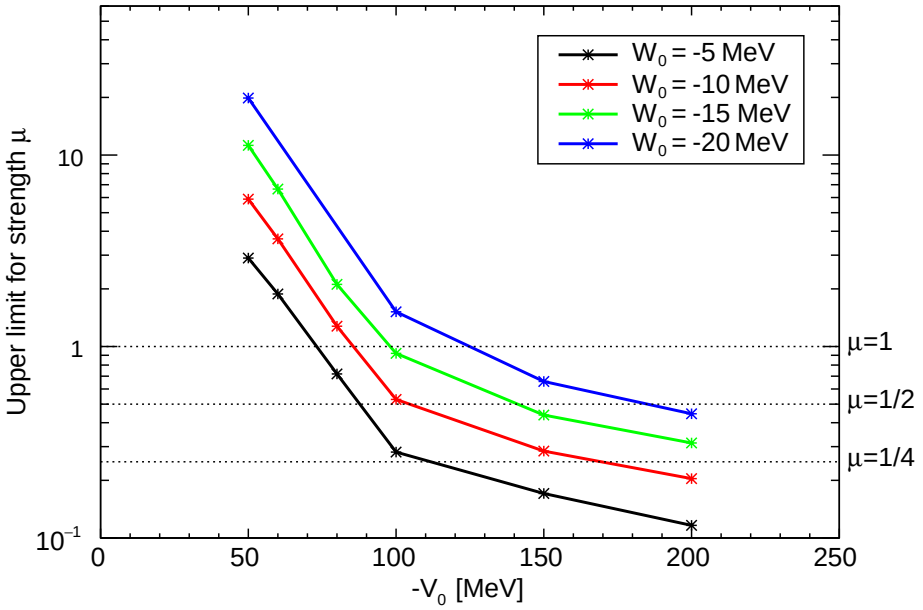

FIGURE 5.7: Evaluated 95% C.L. upper limits for the strength parameter μ are summarized. The colors correspond to different imaginary-part parameters W_0. The evaluated points are linearly interpolated as shown by the solid lines.

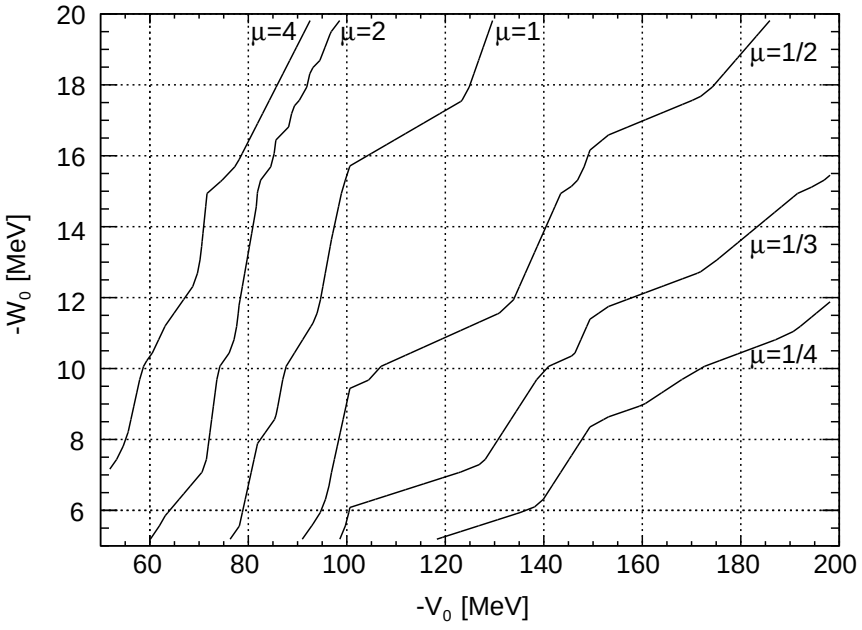

FIGURE 5.8: A contour plot of the 95% C.L. upper limit for the strength parameter μ is shown as functions of the potential parameters $(-V_0, -W_0)$. This figure is based on a linear interpolation between the points shown in Figure 5.7. The contour lines are indicated for $\mu = \frac{1}{4}, \frac{1}{3}, \frac{1}{2}, 1, 2$, and 4.

Chapter 6

Conclusion and Future Outlook

We performed the missing-mass spectroscopy experiment of the ^{12}C(p,d) reaction in order to search for η' mesic nuclei. The 2.5 GeV proton beam of the SIS-18 at GSI was employed to produce the η' mesic nuclei via the ^{12}C(p,d)^{11}C$\otimes\eta'$ reaction, and the momentum of the ejectile deuteron was measured by the FRS spectrometer.

We successfully obtained the excitation-energy spectrum of ^{11}C from -90 MeV to $+30$ MeV from the η' emission threshold. We achieved a high statistical sensitivity at the level of better than 1% in the obtained spectrum, which is essentially important in the inclusive measurement. The experimental resolution of the obtained spectrum was evaluated to be 2.5 MeV, which is sufficiently smaller than the expected widths of the η' mesic states.

Since no peak structure was observed in the excitation-energy spectrum, we determined the upper limits for the formation cross sections of the η' mesic nuclei. The obtained upper limits around the η' emission threshold are 0.1–0.2 μb/sr for the assumed width of the Lorentzian peak of $\Gamma = 5$ MeV, 0.2–0.4 μb/sr for $\Gamma = 10$ MeV, and 0.3–0.6 μb/sr for $\Gamma = 15$ MeV at 95% confidence level. These upper limits are as small as the theoretically-expected cross sections for the deep η'-nucleus potential of the order of 100 MeV. As far as we compare the obtained energy spectrum with the theoretically-calculated spectra, the depth of the η'-nucleus potential, which can be interpreted as the η' mass reduction at normal nuclear density, of larger than 100 MeV is disfavored for the assumed imaginary part of the potential around 10 MeV.

In the future, further experimental investigations to search for η' mesic nuclei are necessary toward a direct study of in-medium properties of the η' meson. Future experiments require a higher experimental sensitivity than the present experiment, and two approaches are considered. One is a similar inclusive measurement of the ^{12}C(p,d) reaction with much better statistics by using a higher-intensity proton beam. The other is a semi-exclusive measurement of the ^{12}C(p,dp) reaction. Once η' mesic nuclei are formed, they are expected to decay via one-nucleon absorption ($\eta' N \to \eta N$ or πN) or two-nucleon absorption ($\eta' NN \to NN$) processes. By tagging the proton from these decay processes in coincidence with the measurement of the forward emitted deuteron, the large amount of background in the missing-mass spectrum can be drastically suppressed. Both of the two experiments are feasible and planned at the future facility FAIR, using the newly constructed accelerator (SIS-100) and the spectrometer system (Super-FRS). Moreover, a measurement of the cross section of the elementary process, $pn \to d\eta'$, is also important to reduce the uncertainty of the magnitude of the theoretically calculated formation cross section and thus to provide a better theoretical reference for the further experimental studies.

Acknowledgements

First and foremost, I would like to express my sincere appreciation to my supervisor Prof. Dr. Ryugo S. Hayano, who introduced me this interesting filed of physics. His broad perspective, brilliant ideas, and wide knowledge of physics impressed and inspired me very much, and there were so many things I learned from him during my five-year study in his group. I would like to thank him for giving me the opportunity to work on the first spectroscopy experiment of η' mesic nuclei, and I acknowledge his invaluable advices and supports throughout my work which greatly helped and encouraged me.

I am deeply grateful to Dr. Kenta Itahashi and Dr. Hiroyuki Fujioka for giving me the opportunity to work on this very interesting experiment. I joined the group just when this project was started, and it was very fortunate for me that I acquired various experiences like hardware and software developments, performing the main experiment, and the data analysis. I discussed many practical issues with Dr. Itahashi and Dr. Fujioka at every stage of the experiment, and their advices and suggestions greatly helped and encouraged me. Not only for this experiment, I learned also many other related topics from their wide knowledge of physics.

I would like to express my great thanks to Prof. Dr. Hans Geissel, Prof. Dr. Christoph Scheidenberger, and Dr. Helmut Weick for accepting me in the FRS group and taking care of me during my stay at GSI. I spent almost two years in total at GSI, and learned many things particularly on the FRS spectrometer system. They introduced me a basic concept of ion optics and also technical methods such as an optics simulation, optics tuning, and analysis of the optics properties. These were very helpful and useful to consider the experimental setup of this experiment. They also gave me opportunities to participate in other experiments performed at the FRS, and I was impressed to know the wide applicability of the FRS spectrometer system.

I would like to express my appreciation to all the collaborators[1] of this experiment for their contributions to the experiment. Especially, I would like to thank Prof. Dr. Volker Metag, Dr. Mariana Nanova, Dr. Stefan Friedrich, Dr. Ken Suzuki, Dr. Satoru Terashima, Mr. Takahiro Nishi, Mr. Yuni N. Watanabe, and Mr. Hiroki Yamakami, who gave me a lot of valuable advices and suggestions not only in the main experiment but throughout the whole work including test experiments for detector developments and weekly meetings for discussing detailed data analysis. I learned many experimental techniques and data analysis methods from them. I would like to also express my special appreciation to the collaborators in the FRS group at GSI. Their expert knowledge of the FRS was invaluable in preparing the experimental setup, developing the ion optics, and carrying out the measurements.

I am deeply grateful to Prof. Dr. Satoru Hirenzaki, Prof. Dr. Daisuke Jido, Dr. Hideko Nagahiro, Dr. Natsumi Ikeno, and Ms. Yuko Higashi for their theoretical contributions to the experiment. Their theoretical suggestions were very important to plan the experiment and also will be important to make a future experimental plan. Their intuitive and comprehensive explanations helped me to learn theoretical aspects of studying the η' mesic nuclei.

I would like to express my gratitude to Mr. Karl-Heinz Behr, Mr. Tobias Blatz, Mr. Adolf Bruenle, Mr. Christos Karagiannis, Mr. Alexander Kratz, Mr. Christian Schloer, and Mr. Bogdan Szczcepanczyk, the technical group of the FRS. Their accurate and quick technical support was invaluable in preparing for all the detector test experiments and the main experiment.

[1] The collaboration members are listed in Appendix F.

I would like to thank the accelerator group at GSI for their effort in tuning the beam and keeping its stable condition. During the beam time in August 2014, the beam conditions were very stable, and that was essentially important for achieving a high statistical sensitivity.

I would like to acknowledge Prof. Dr. James Ritman, Dr. Frank Goldenbaum, Dr. Dieter Prasuhn, and Dr. Olaf Felden at Institute for Nuclear Physics in Forschungszentrum Jülich for their kind support to our detector test experiment at the COSY accelerator. This test experiment greatly helped the hardware development and preparation for the production experiment at GSI.

I would like to express my special thanks to the members of the nuclear physics experiment (NEX) group at the University of Tokyo: Prof. Dr. Ryugo S. Hayano, Dr. Takatoshi Suzuki, Dr. Masaharu Sato, Dr. Hideyuki Tatsuno, Dr. Satoshi Itoh, Mr. Yuya Fujiwara, Dr. Hexi Shi, Dr. Tadashi Hashimoto, Dr. Takumi Kobayashi, Dr. Koichi Todoroki, Mr. Takahiro Nishi, Mr. Kota Okochi, Mr. Yohei Murakami, Mr. HiroyukiYamada, Mr. Yuni N. Watanabe, Mr. Hiroshi Horii, Mr. Takashi Ando, Prof. Dr. Hiroyoshi Sakurai, Dr. Megumi Niikura, Dr. Zhengyu Xu, Dr. Nobuyuki Kobayashi, Mr. Ryo Taniuchi, Mr. Keishi Matsui, Mr. Satoru Momiyama, Mr. Takuya Miyazaki, Mr. Shunpei Koyama, Mr. Takeshi Saito, Mr. Shunsuke Nagamine, Dr. Kathrin Wimmer, Prof. Dr. Kentaro Yako, Prof. Dr. Kyoichiro Ozawa, Dr. Yosuke Watanabe, Mr. Yusuke Komatsu, Mr. Shinichi Masumoto, Ms. Atsuko Takagi, Mr. Koki Kanno, Mr. Wataru Nakai. I enjoyed daily research life with them in the Hongo campus. They are working on a variety of experiments, and I learned many topics through discussions with them. Particularly, I would like to thank Dr. Itoh, Mr. Nishi, Mr. Okochi, and Mr. Watanabe, with whom I worked together on the η' mesic nucleus experiment at GSI and the pionic atom experiment at RIKEN. I enjoyed working with them very much. We discussed many things like detector developments, data analysis, and so on, and they gave me a lot of helpful suggestions. Moreover, I would like to especially thank the senior students in Hayano group, Dr. Itoh, Mr. Fujiwara, Dr. Shi, Dr. Hashimoto, Dr. Kobayashi, Dr. Todoroki, and Mr. Nishi. They kindly taught me many basic skills of experiments and computing in the beginning of my study.

I would like to express my thanks to Ms. Miwa Sugawara, Ms. Yuko Oshika, the secretaries of the NEX group at the University of Tokyo, and Ms. Siglind Raiss and Ms. Luise Dörsching-Steitz, the secretaries of the FRS group at GSI. Ms. Sugawara and Ms. Oshika helped me with a lot of paperwork in Japan during my stay in Germany. Ms. Raiss and Ms. Dörsching-Steitz kindly helped me to complete necessary procedures to stay in Germany for a long period, such as finding accommodation, applying for German visa, and so on. They also sometimes introduced me some interesting places to visit, and I enjoyed staying in Germany very much.

I would like to express my gratitude to the thesis examiners, Prof. Dr. Susumu Shimoura, Prof. Dr. Tetsuo Hatsuda, Prof. Dr. Kyoichiro Ozawa, Prof. Dr. Hiroyoshi Sakurai, and Prof. Dr. Kentaro Yako, for reviewing my doctoral thesis and giving me many valuable comments.

Last but not least, I would like to thank my family and all my friends for their continuous supports and encouragements.

Appendix A

Beam Energy

A.1 Mean Value of Beam Energy

Kinetic energies of the primary proton beams are determined from measured Schottky-noise frequencies in the SIS-18 synchrotron. Table A.1 lists the measured frequencies, harmonic numbers, and a circumference of SIS-18[1] for the 2.5 GeV and 1.6 GeV beams. The revolution frequency of the beam is calculated by dividing the measured frequency by the harmonic number. Then, the kinetic energy is obtained by calculating the velocity of the beam.

TABLE A.1: Values used for determination of the beam energies.

	2.5 GeV beam	1.6 GeV beam
Circumference of SIS-18	216.711 ± 0.010 m	216.711 ± 0.010 m
Measured frequency	23.9552 ± 0.0001 MHz	24.4550 ± 0.0002 MHz
Harmonic number	18	19
Revolution frequency	1.33084 ± 0.00001 MHz	1.28710 ± 0.00001 MHz
Beam energy	2499.1 ± 2.0 MeV	1621.6 ± 0.8 MeV

Next, we evaluate a systematic error for the missing-mass calculation. Since the 1.6 GeV beam energy affects the calibration momentum $P_{\mathrm{calibration}}$ in Section 4.5.1, the errors of both the two energies contribute to the systematic error of the missing-mass calculation for the production measurement. In order to take into account a correlation between the errors of the two energies originating from the uncertainty of the circumference, we first estimate the mean circumference for the two energies as $L_{\mathrm{mean}} = 216.711 \pm 0.010$ m and their difference as $L_{\mathrm{diff}} = 0 \pm 0.005$ m. Then, by considering $\Delta L_{\mathrm{mean}} = 0.010$ m and $\Delta L_{\mathrm{diff}} = 0.005$ m independently, the systematic error for the missing-mass calculation is evaluated to be ± 1.4 MeV/c^2.

A.2 Extraction Time Dependence of Beam Energy

An extraction-time dependence of the beam energy is analyzed using the the data of the $d(p,d)p$ elastic scattering. Figure A.1 shows a correlation between the extraction time from the start timing of each spill and the optics-corrected position at the F4 focal plane observed in the proton-deuteron elastic scattering at 2.5 GeV. The evaluated peak position for each extraction-time bin is shown by the blue graph. This graph is fitted by a linear function, as shown by the red line, and the slope is evaluated to be 1.58 mm/s.

[1] The circumference of SIS-18 was re-measured in 2014 before this experiment.

The observed correlation is attributed to the extraction-time dependence of the beam energy. Since no significant position shift of the beam at the target was observed[2], the only possible explanation for the observed shift in Figure A.1 is the shift of the beam energy during every spill. By a kinematical calculation, the rate of the beam energy shift is evaluated to be $\frac{dT_p}{dt} = -1.57$ MeV/s.

A long-term stability of the rate of the energy shift is estimated to be within ±13% based on the same analysis for the elastic scattering at 1.6 GeV, which was measured frequently for the spectrometer calibration. A similar dependence is seen also for the 1.6 GeV beam, and the evaluated rate of the energy shift is stable within ±13% for all the measurements.

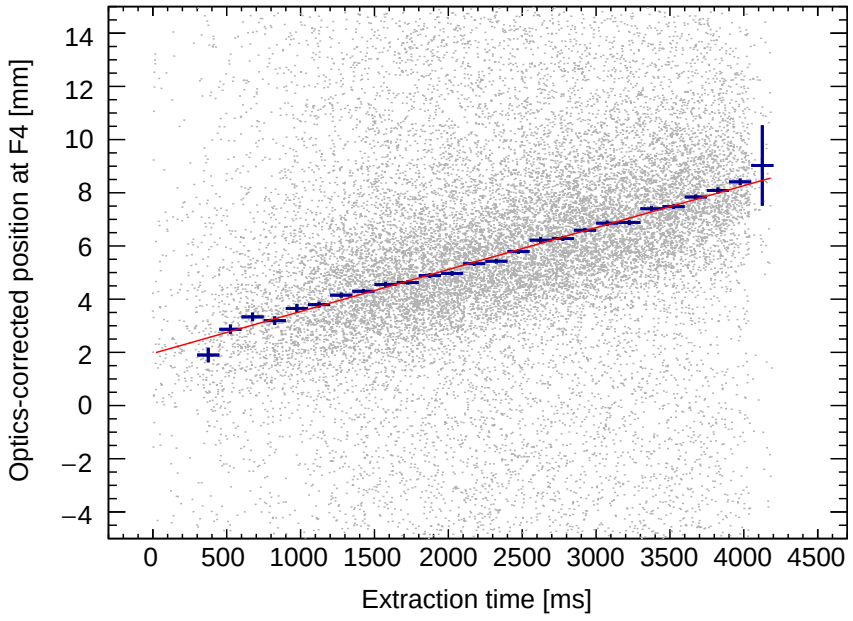

FIGURE A.1: Extraction-time dependence of the beam energy observed in the proton-deuteron elastic scattering at 2.5 GeV. The horizontal axis is the extraction time from the start timing of each spill, and the vertical axis is the optics-corrected position of the deuteron at F4. The blue graph shows the fitted peak position for each extraction-time bin, and this graph is fitted by a linear function, as indicated by the red line.

[2] We checked the beam position at the target by using a scintillator target and a camera.

Appendix B

Simulation of MWDC Analysis

The conventional method of the MWDC analysis described in Section 4.3 causes a distortion in the reconstructed position spectrum. The origin of the distortion is found to be the χ^2 fitting, where a track with a minimum χ^2 is always adopted. In this appendix, we demonstrate the distortion of the reconstructed position spectrum by a simplified simulation of the MWDC analysis.

As a first step of the simulation, a track is randomly generated with a uniform spatial distribution in -100 mm $\leq x \leq 100$ mm, -40 mm $\leq y \leq 40$mm, -20 mrad $\leq a \leq 20$ mrad, and -20 mrad $\leq b \leq 20$ mrad. Then, a drift length in each MWDC plane is calculated[1], and a measured drift time in the simulation is set by

$$(\text{drift time}) = 20\,\text{ns/mm} \times (\text{drift length}) + (\text{Gaussian resolution with } \sigma = 5 \text{ ns}), \quad \text{(B.1)}$$

where a constant drift velocity of 0.05 mm/ns and a constant resolution of 5 ns are assumed. The generated distribution of the drift length and the drift time is shown in Figure B.1.

Next, the generated drift time is analyzed in the same way as the analysis in Section 4.3. Two methods are considered for the conversion of the drift time to the drift length. One is the same as our analysis, where a length with a highest probability is adopted for each measured time. This conversion function is shown by the red line in Figure B.1, and the converted drift-length distribution is shown in the left panel of Figure B.2. In this method, deduced drift lengths for drift times shorter than 0 ns and longer than 50 ns are 0 mm and 2.5 mm, respectively. The other method is to use a conversion function which makes a converted length distribution completely flat from 0 mm to 2.5 mm. This function can be constructed by Equation (4.5). The obtained conversion function is shown by the blue line in Figure B.1, and the converted length distribution is shown in the right panel of Figure B.2. While the converted length distribution becomes completely flat, the conversion function is slightly shifted from the input relation around 0 mm and 2.5 mm.

Tracks are reconstructed for both of the considered calibration functions by the χ^2 fitting in the same way as described in Section 4.3. All of the 16 planes, including the X-type planes, are used for the fitting. The reconstructed horizontal positions on the first X plane are shown in Figure B.3. In both of the cases, structures due to the distortion around the wire positions are observed. The result in the left panel shows that the distortion is caused even with the simplified and known time-to-length relation, while the result in the right panel shows that the calibration function constructed to make the flat length distribution does not result in a flat distribution of the reconstructed position. As far as these conventional methods with the χ^2 fitting are used, such distorted structures are inevitably introduced, and they need to be carefully considered particularly for a measurement with a high statistical sensitivity.

[1] The configuration of the MWDCs in this simulation is the same as that in the experiment.

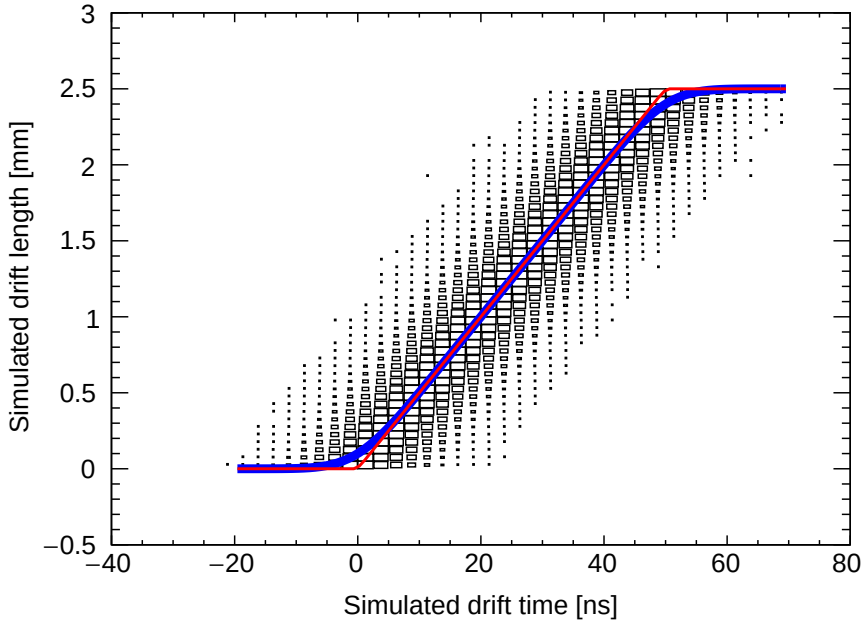

FIGURE B.1: A generated distribution of the drift length (input) and the drift time (simulated data). The red and blue lines are functions used to deduce a drift length from the simulated drift time. See the text for the detail.

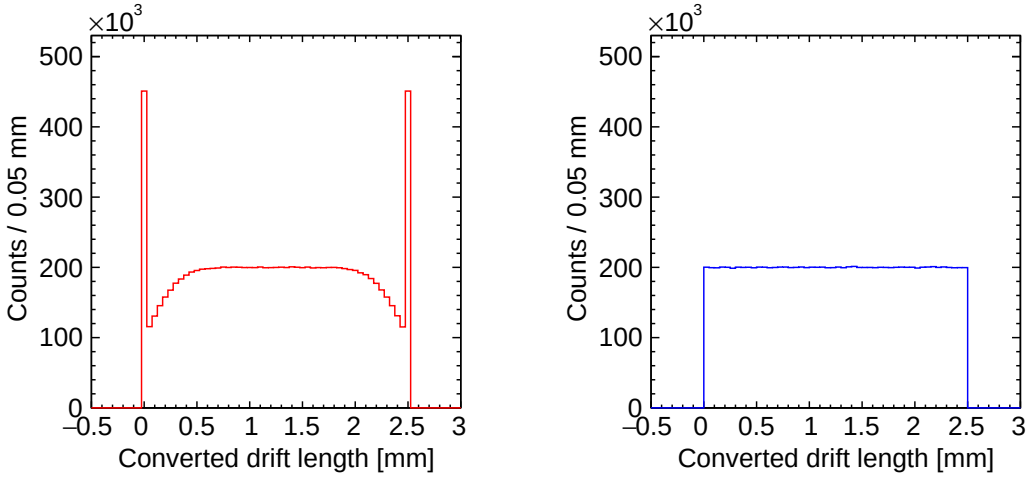

FIGURE B.2: Histograms of the deduced drift length in the simulation. The left panel corresponds to the calibration function shown by the red line in Figure B.1, and the right panel corresponds to that by the blue line in Figure B.1.

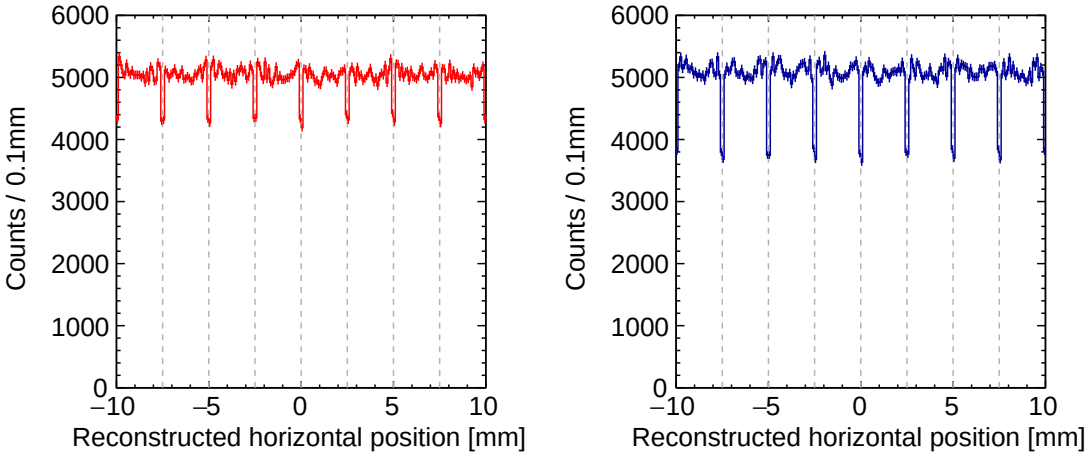

FIGURE B.3: Reconstructed position spectra in the simulation at the first X-type plane are shown. The left panel corresponds to the calibration function shown by the red line in Figure B.1, and the right panel corresponds to that by the blue line in Figure B.1. The gray dashed lines show the wire positions on this plane.

Appendix C

^{11}C in Calibration Measurements

In the calibration measurements with the 1.6 GeV proton beam and the CD_2 target, not only the $d(p,d)p$ elastic peak but also peaks of the ^{11}C ground state and some excited states are observed near the edge of the momentum acceptance. While the calibration parameters of the ion-optics are determined only with the $d(p,d)p$ elastic peaks measured at the several FRS scaling factors, the observed ^{11}C peaks are used for additional confirmation of the calibration in this appendix.

Figure C.1 shows the optics-corrected horizontal positions at F4 obtained in the calibration measurements at the FRS scaling factors of $f = 1.01$ in the top panel and $f = 1.02$ in the bottom panel. The proton-deuteron elastic scattering is seen around 35 mm for $f = 1.01$ and 70 mm for $f = 1.02$, and additionally small structures are observed around -70 mm for $f = 1.01$ and -35 mm for $f = 1.02$. An enlarged plot of the structure is shown inside each figure with the calculated excitation energy of ^{11}C in the upper axis. The ground state of ^{11}C and excited states around 7 MeV and 13 MeV are observed. This behavior is similar to the $^{12}C(p,d)$ spectrum at 800 MeV proton energy reported in Smith *et al.* [57], in which larger contributions from the ^{11}C ground state, the $\frac{7}{2}^-$ state at 6.48 MeV, and a wide enhancement around 13.2 MeV are seen.

The observed position of the ground state is consistent with the calculated position, which is based on the calibration parameters determined only with the proton-deuteron elastic peak, within the experimental errors. Thus, this provides additional confirmation of the validity of the optics calibration discussed in Section 4.4.

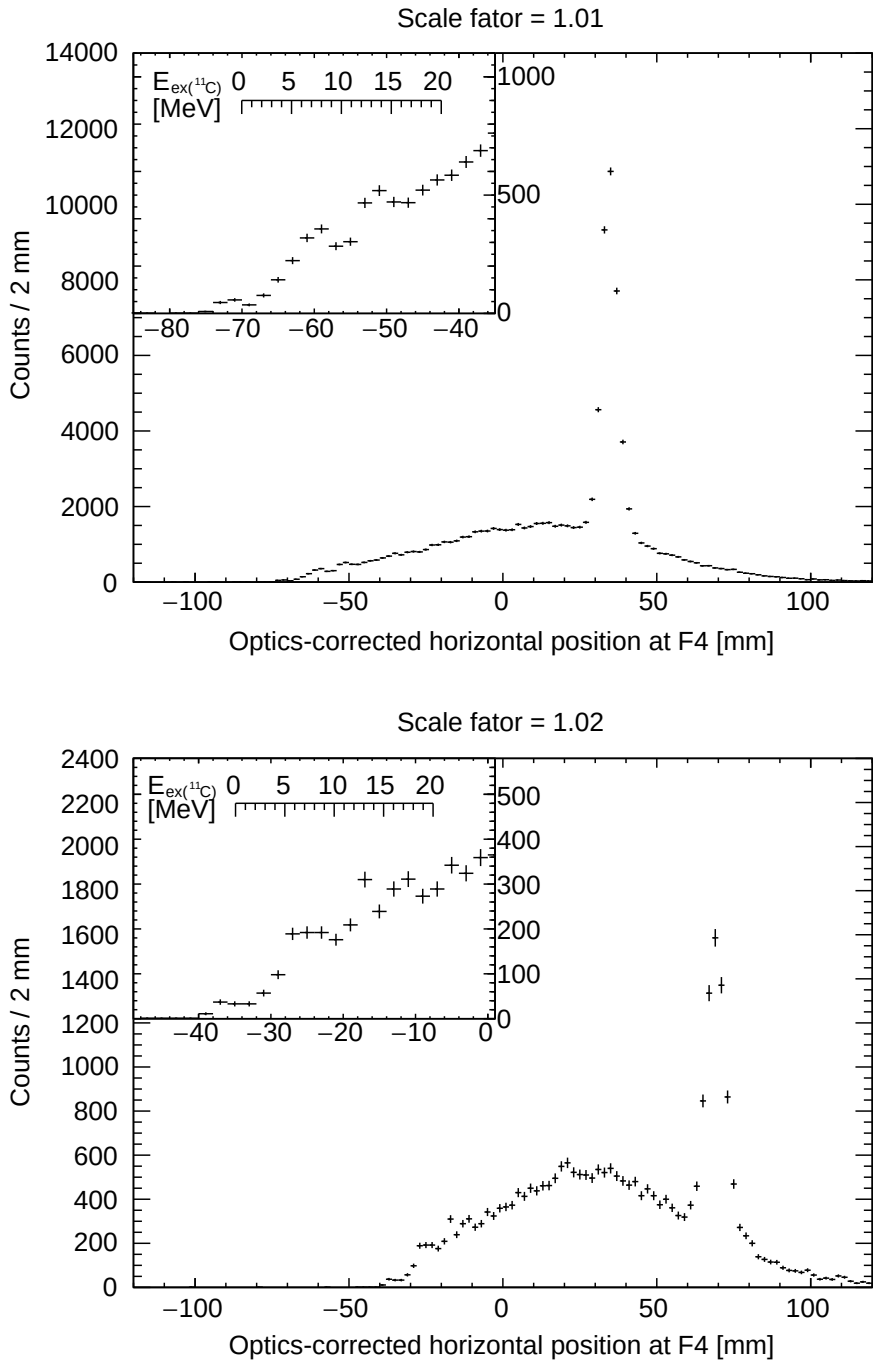

FIGURE C.1: Optics-corrected position spectra at F4 obtained in the calibration measurements are shown. The spectrum with the FRS scaling factor of $f = 1.01$ is shown in the top panel, and that with $f = 1.02$ in the bottom panel. An enlarged plot around the ^{11}C states is shown inside each figure, and the calculated excitation energy for ^{11}C is indicated by the upper axis.

Appendix D

Simultaneous Fitting of Spectra

In this appendix, upper limits for the formation cross sections of η' mesic states are evaluated by simultaneous fitting of all the production data sets in order to check the validity of the discussion based on the averaged spectrum in Section 5.2. Here, the eight spectra of the production measurements, shown in the top panel of Figure 4.24, are fitted simultaneously as

$$\begin{aligned}
&\text{Spectrum of dataset “Prod0980”} \leftarrow I_{\text{Prod0980}} \times f(E) && \text{(D.1)}\\
&\text{Spectrum of dataset “Prod0983”} \leftarrow I_{\text{Prod0983}} \times f(E) && \text{(D.2)}\\
&\qquad\qquad\qquad\qquad\vdots\\
&\text{Spectrum of dataset “Prod1020”} \leftarrow I_{\text{Prod1020}} \times f(E). && \text{(D.3)}
\end{aligned}$$

$f(E)$ is the test function defined in Equation (5.2), which contains the parameter for the peak height A and the background parameters p_0, p_1, p_2, p_3. Additionally, factors I_{Prod0980}, I_{Prod0983}, …, I_{Prod1020} are introduced to allow shifts of the relative normalization of the spectra. One of these factors is fixed at 1, and all the other factors are treated as free parameters together with the background parameters.

Figure D.1 shows a result of simultaneous fitting only with the third-order polynomial background by fixing $A = 0$. χ^2/ndf of the fit is 263/257. In this treatment, ndf (number of degree of freedom) is correctly defined. The residual plots are also shown in Figure D.2, where $\pm 2\sigma$ error regions are shown by the dashed lines. The spectra are well fitted with the third-order polynomial also in this method.

Upper limits for the formation cross sections are evaluated in the same method as in Section 5.2, except for the additional free parameters. Figure D.3 shows the fitted spectra with the test functions for $(E_{\text{test}}, \Gamma_{\text{test}}) = (-5\ \text{MeV}, 5\ \text{MeV})$, as an example. The fit region is taken as $E_{\text{test}} - 35\,\text{MeV} \leq E \leq E_{\text{test}} + 35\,\text{MeV}$. Then, the upper limit at 95% confidence level is determined from the fitted height and its associated error. In Figure D.4, the signal component with the fitted height is shown in blue, and that with the evaluated limit is shown in red.

Obtained upper limits for all the tested excitation energies and widths are summarized in Figure D.5. The solid lines show the results by the simultaneous fitting, and the dashed lines show those by the fitting of the averaged spectrum, discussed in Section 5.2. Very similar results are obtained by the two methods, which means the treatment in Section 5.2 is not significantly affected by the averaging of the eight spectra. Small differences between the two methods observed in Figure D.5 are included in the evaluation of the systematic errors in Section 5.2.2.

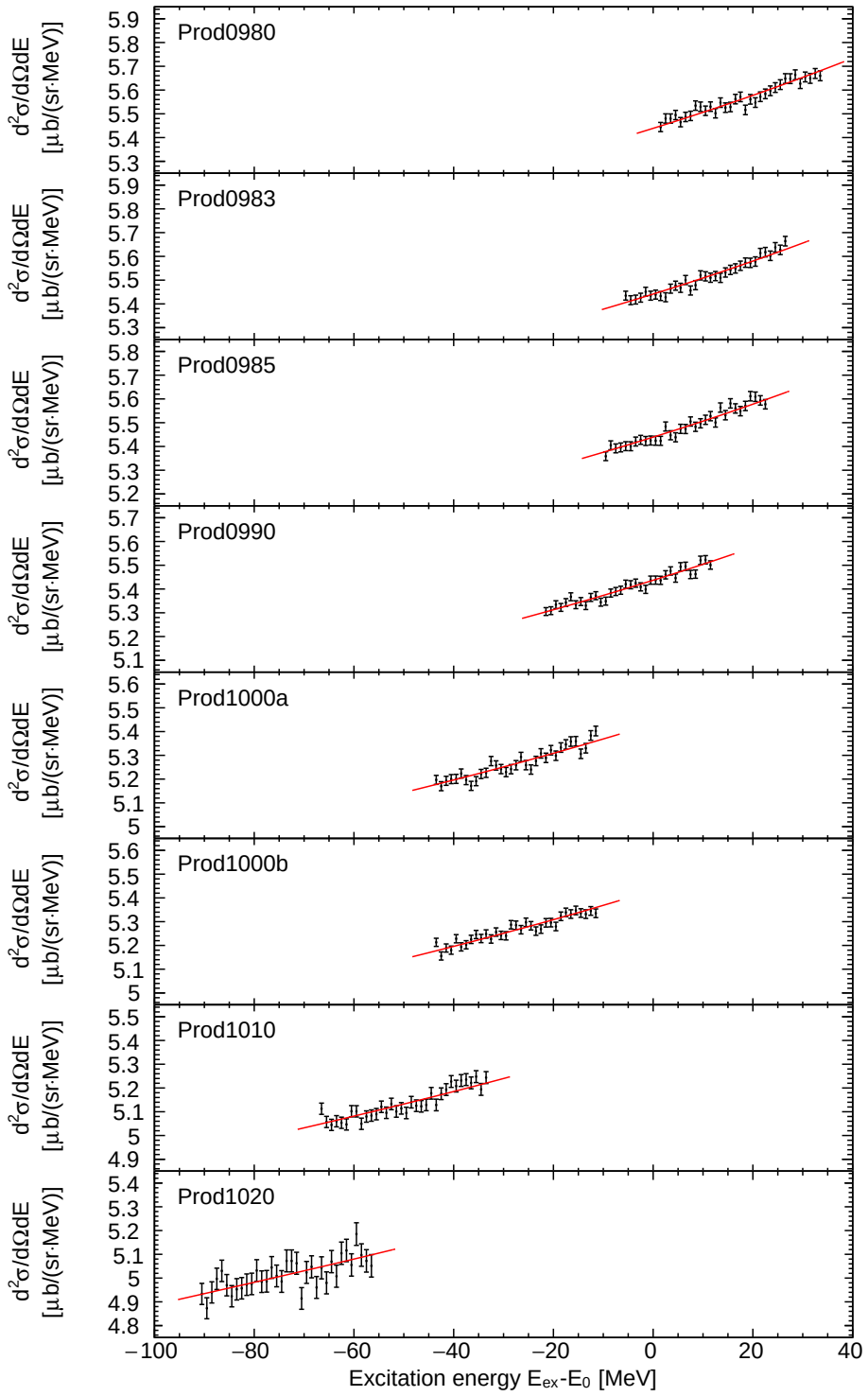

FIGURE D.1: Simultaneous fitting of the spectra only with the polynomial background.

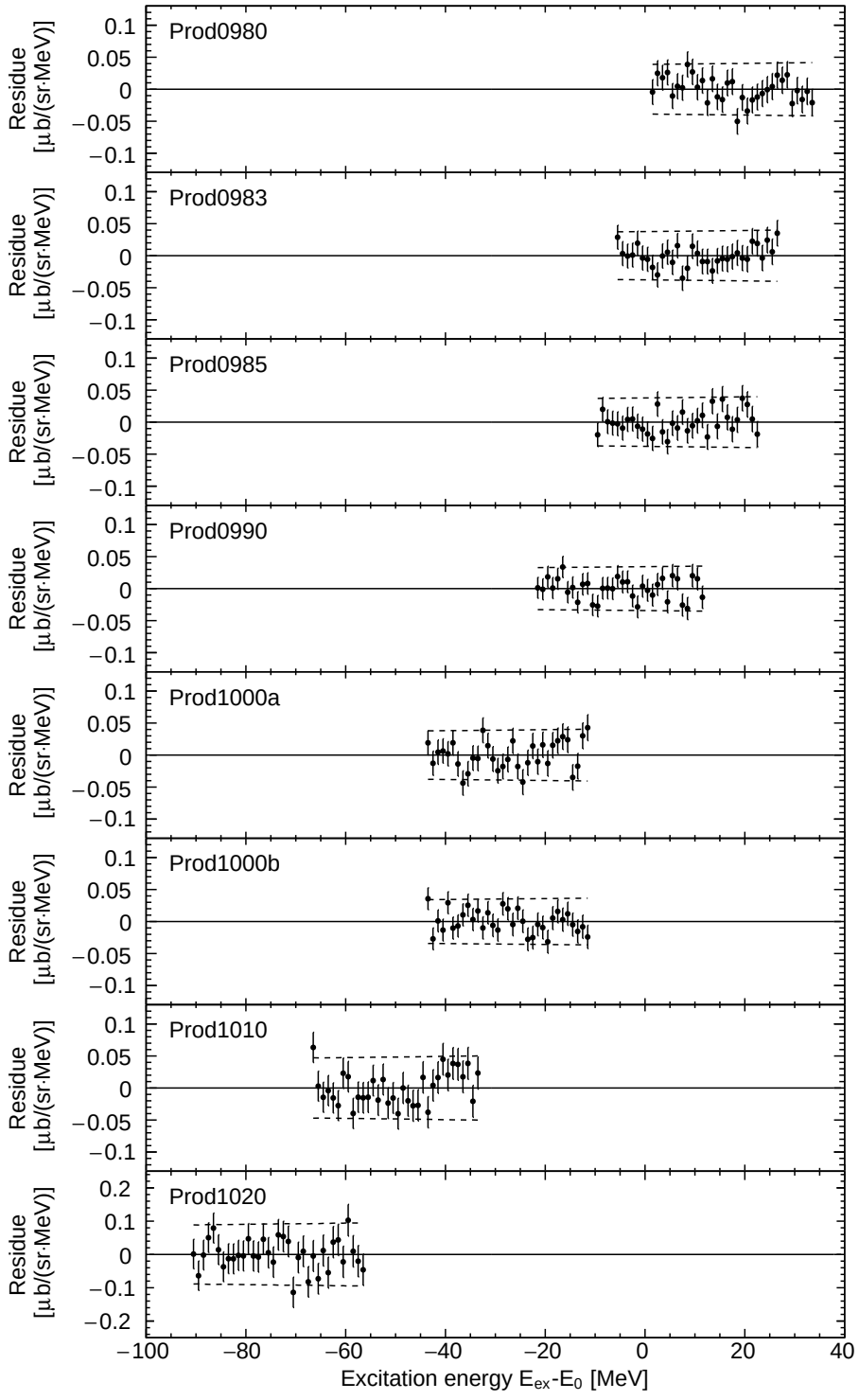

FIGURE D.2: Residual plots for the simultaneous fitting of the spectra only with the polynomial background are shown. The dashed lines indicate $\pm 2\sigma$ error regions.

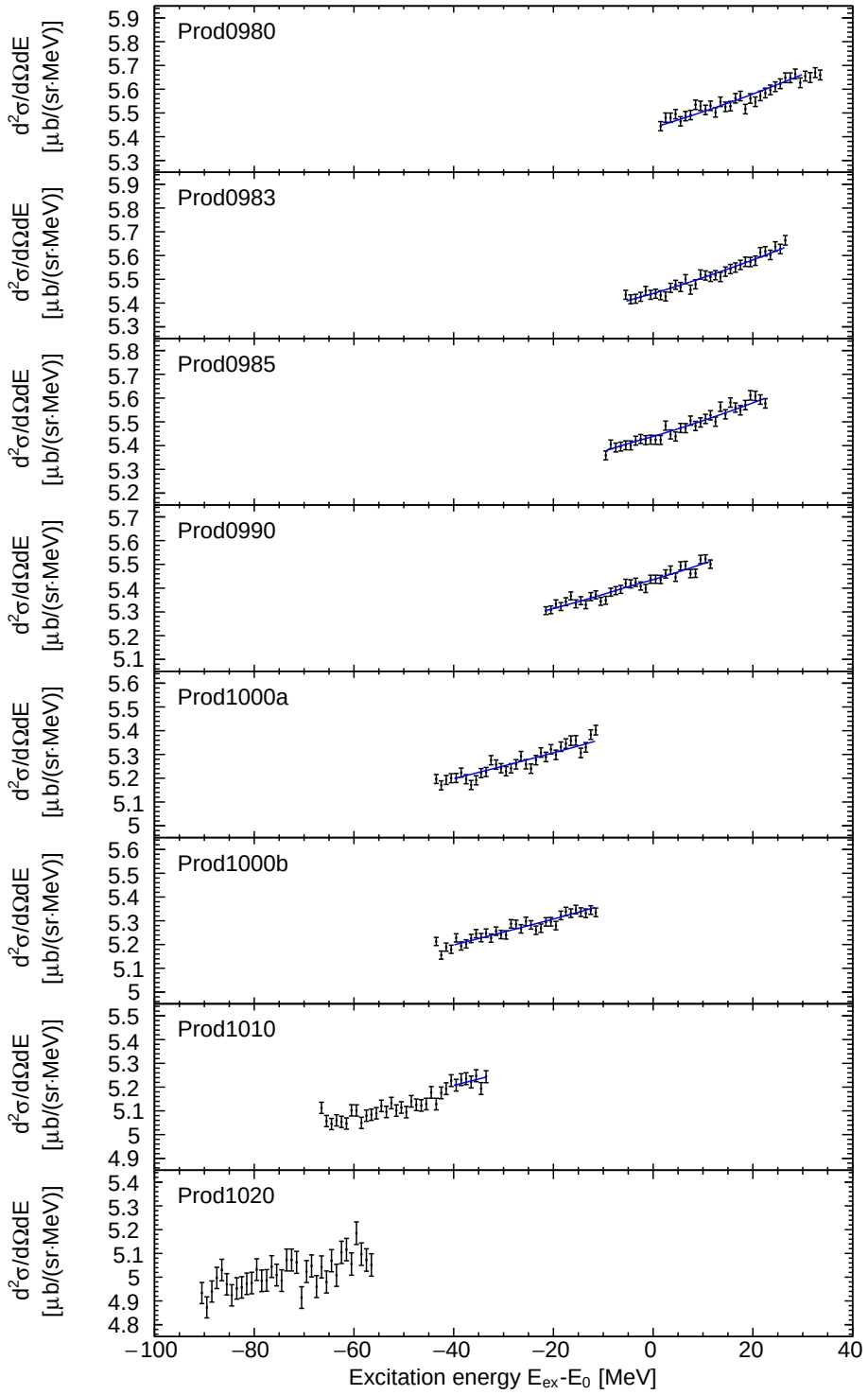

FIGURE D.3: Simultaneous fitting of the spectra for $(E_{\text{test}}, \Gamma_{\text{test}}) = (-5\,\text{MeV}, 5\,\text{MeV})$. In this case, the fit region is $-40\,\text{MeV} \leq E \leq 30\,\text{MeV}$, and the dataset "Prod1020" is not included in the fitting.

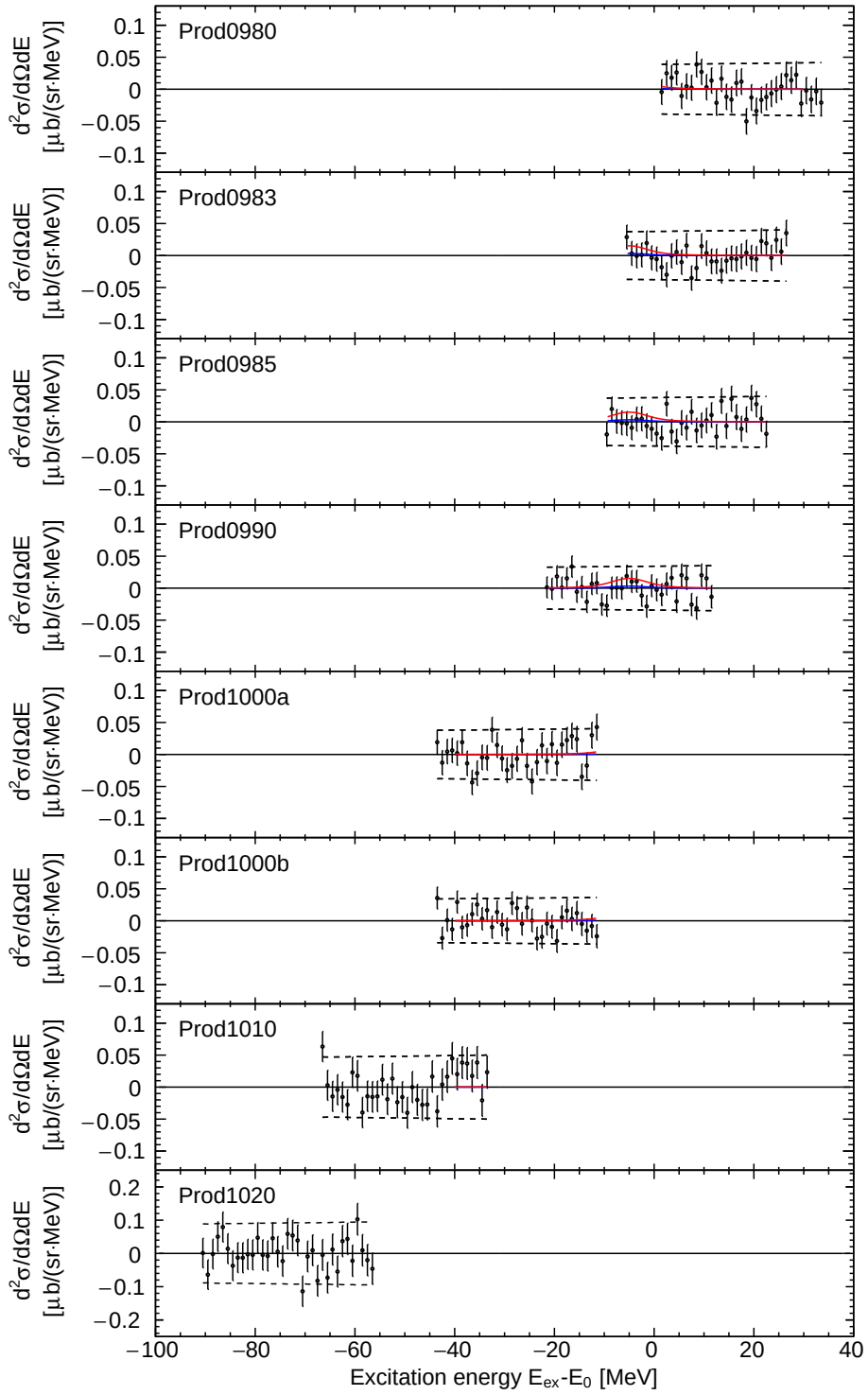

FIGURE D.4: Signal components for the fitted height (blue) and the evaluated limit (red) by the simultaneous fitting are shown for $(E_{\mathrm{test}}, \Gamma_{\mathrm{test}}) = (-5\,\mathrm{MeV},\ 5\,\mathrm{MeV})$. The residual plots of the background-only fit, in Figure D.2, are shown as references.

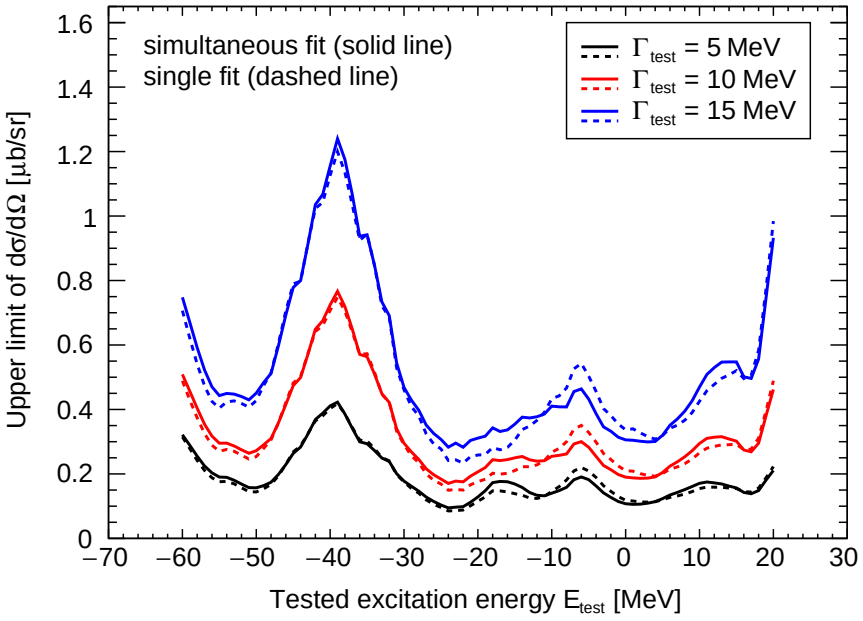

FIGURE D.5: Obtained 95% C.L. upper limits for the formation cross sections by the simultaneous fitting are shown by the solid lines. The limits by the single fitting of the averaged spectrum, described in Section 5.2, are shown by the dashed lines. The colors correspond to the different widths Γ_{test}, as indicated in the box.

Appendix E

Understanding of Background in Inclusive Spectrum

In this appendix, the ^{12}C(p,d) spectrum is compared with the d(p,d) spectrum, which was measured as a reference of the quasi-free background in the inclusive spectrum. The left panel of Figure E.1 shows the ^{12}C(p,d) and d(p,d) spectra in red and black, respectively, which are obtained in Section 4.9. Both of these spectra are plotted as functions of $E_{\mathrm{ex}(n)}$, the excitation energy calculated with the neutron mass. A ratio of the cross section for carbon to that for deuterium is calculated at each energy bin and plotted in the right panel of the figure. The ratio is constant in a higher energy region, as indicated by the red dashed line, while the ratio decreases in the lower excitation-energy region.

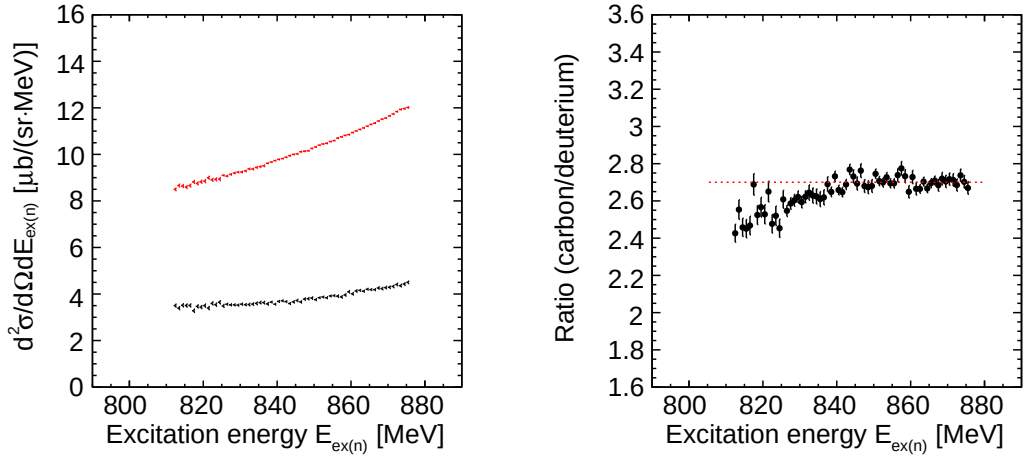

FIGURE E.1: Obtained spectra of the ^{12}C(p,d) and d(p,d) reactions are shown in red and black, respectively (left). The ratio of the carbon spectrum to the deuterium spectrum is plotted as a function of $E_{\mathrm{ex}(n)}$ (right).

One of the possible reasons for this difference of the spectrum shape in the lower energy region is the quasi-free ω meson production. Since the mass of the ω meson, 783 MeV/c^2, is close to the measured region of the excitation energy $E_{\mathrm{ex}(n)}$, a difference of the nucleon momentum distribution between deuterium and carbon may lead to the difference of the spectrum shape.

In order to estimate the contribution of the quasi-free ω production, we perform a simplified simulation of the quasi-free processes, taking into account different nucleon momentum distributions for carbon [58] and deuterium [59]. We consider the multi-pion production

and the ω meson production $p\,N \to d\,X$ $(X = 2\pi,\, 3\pi,\, 4\pi,\, \omega)$ as the major background, following the approach by Lehmann [60]. The total cross section of $p\,n \to d\,\omega$ is estimated by extrapolating data in Barsov *et al.* [61], and for the cross sections of the pion productions, we use parameterization given in Lehmann [60]. Then, double differential cross sections of the quasi-free processes for carbon and deuterium are simulated by assuming a uniform angular distribution in the center-of-mass frame.

Figure E.2 shows simulated cross sections for deuterium in the left panel and for carbon in the right panel. The contributions of the 2π, 3π, 4π, and ω productions are shown by the blue, green, magenta, and red lines, respectively, and the total spectra are shown by the black lines. The simulation results for the carbon target correspond to one proton and one neutron in the carbon nucleus, and it needs to be multiplied by an effective nucleon number. In these simulation results, a difference of the spectrum shape can be seen between the two targets, mainly due to the difference in the ω production spectrum.

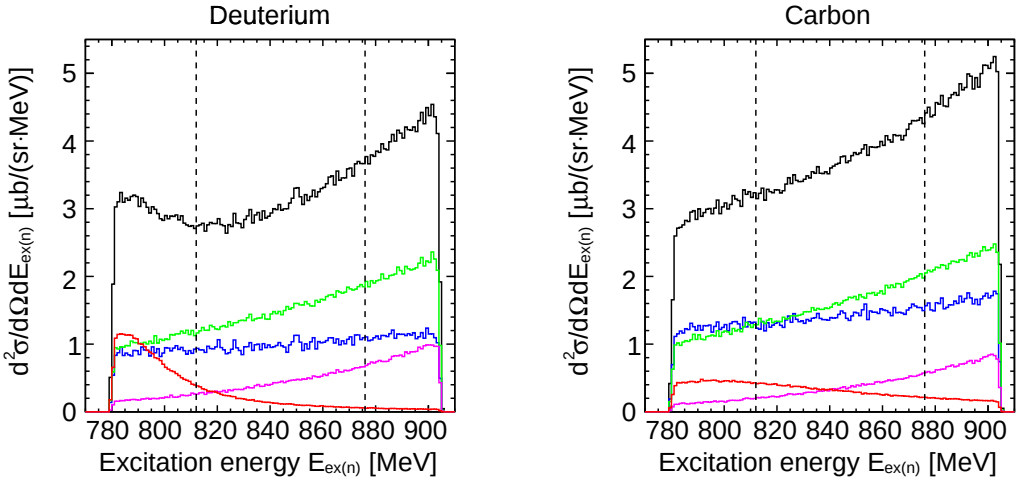

FIGURE E.2: Simulated cross sections of the quasi-free processes are shown for the deuteron target (left) and for the carbon target (right). Contributions of the 2π, 3π, 4π, and ω productions are shown in blue, green, magenta, and red, respectively. The black lines show the total spectra. The cross section for the carbon target corresponds to one proton and one neutron in the carbon nucleus, and it needs to be multiplied by an effective nucleon number. The dashed lines indicate the regions of the experimentally obtained spectra.

The experimental spectra are compared with the simulated cross sections in Figure E.3. In the left panel, the experimental $d(p,d)$ spectrum is shown by the blue graph, and the simulated total spectrum scaled by a factor $\alpha(d) \sim 1.25$ is shown by the black line. The experimental spectrum is well described by the simulated spectrum, by allowing an additional scale factor of $\alpha(d) \sim 1.25$. In the right panel, the red graph shows the experimental $^{12}\mathrm{C}(p,d)$ spectrum, and the black line shows the simulated total spectrum scaled by a factor $\alpha(\mathrm{C}) \sim 2.75$, which corresponds to an effective nucleon number of about $\alpha(\mathrm{C})/\alpha(d) \sim 2.2$. The simulated spectrum with the adjusted scale factor well describes the overall shape of the experimental spectrum also for the carbon target. Thus, the inclusive background in the $^{12}\mathrm{C}(p,d)$ spectrum can be understood with the quasi-free processes in comparison with the $d(p,d)$ spectrum obtained in the reference measurement.

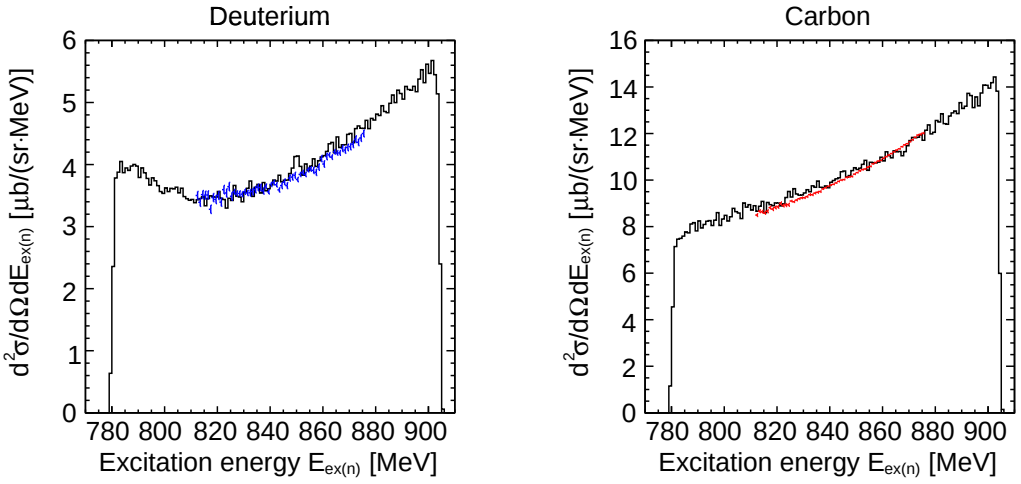

FIGURE E.3: The experimentally obtained $d(p,d)$ spectrum is shown by the blue graph (left) and the ^{12}C(p,d) spectrum is shown by the red graph (right). The simulated spectra are shown by the black lines for both of the targets. The simulated spectra are scaled by an additional factor of $\alpha(d) \sim 1.25$ in the left panel and by $\alpha(\mathrm{C}) \sim 2.75$ in the right panel.

Appendix F

Collaborators

Yoshiki K. Tanaka[a], Yassid Ayyad[b], Jose Benlliure[c], Kai-Thomas Brinkmann[d], Stefan Friedrich[d], Hiroyuki Fujioka[e,1], Hans Geissel[d,f], Jnaneswari Gellanki[g], Chenlei Guo[h], Eric Gutz[d], Emma Haettner[f], Muhsin N. Harakeh[g], Ryugo S. Hayano[a], Yuko Higashi[i], Satoru Hirenzaki[i], Christine Hornung[d], Yoichi Igarashi[j], Natsumi Ikeno[k], Kenta Itahashi[ℓ,2], Masahiko Iwasaki[ℓ], Daisuke Jido[m], Nasser Kalantar-Nayestanaki[g], Rituparna Kanungo[n], Ronja Knoebel[d,f], Nikolaus Kurz[f], Volker Metag[d], Ivan Mukha[f], Tomofumi Nagae[e], Hideko Nagahiro[i], Mariana Nanova[d], Takahiro Nishi[ℓ], Hooi Jin Ong[b], Stephane Pietri[f], Andrej Prochazka[f], Christophe Rappold[f], Moritz P. Reiter[f], Jose Luis Rodríguez Sánchez[c], Christoph Scheidenberger[d,f], Haik Simon[f], Branislav Sitar[o], Peter Strmen[o], Baohua Sun[h], Ken Suzuki[p], Imrich Szarka[o], Maya Takechi[q], Isao Tanihata[b,h], Satoru Terashima[h], Yuni N. Watanabe[a], Helmut Weick[f], Eberhard Widmann[p], John S. Winfield[f], Xiaodong Xu[f], Hiroki Yamakami[e], Jianwei Zhao[h]

[a]The University of Tokyo, 7-3-1 Hongo, Bunkyo, 113-0033 Tokyo, Japan
[b]RCNP, Osaka University, 10-1 Mihogaoka, Ibaraki, 567-0047 Osaka, Japan
[c]Universidade de Santiago de Compostela, 15782 Santiago de Compostela, Spain
[d]Universität Giessen, Heinrich-Buff-Ring 16, 35392 Giessen, Germany
[e]Kyoto University, Kitashirakawa-Oiwakecho, Sakyo-ku, 606-8502 Kyoto, Japan
[f]GSI, Planckstrasse 1, 64291 Darmstadt, Germany
[g]KVI-CART, University of Groningen, Zernikelaan 25, 9747 AA Groningen, the Netherlands
[h]Beihang University, Xueyuan Road 37, Haidian District, 100191 Beijing, China
[i]Nara Women's University, Kita-Uoya Nishi-Machi, 630-8506 Nara, Japan
[j]KEK, 1-1 Oho, Tsukuba, 305-0801 Ibaraki, Japan
[k]Tottori University, 4-101 Koyamacho-minami, 680-8551 Tottori, Japan
[ℓ]Nishina Center, RIKEN, 2-1 Hirosawa, Wako, 351-0198 Saitama, Japan
[m]Tokyo Metropolitan University, 1-1 Minami-Osawa, Hachioji, 192-0397 Tokyo, Japan
[n]Saint Mary's University, 923 Robie Street, Halifax, Nova Scotia B3H 3C3, Canada
[o]Comenius University Bratislava, Mlynská dolina, 842 48 Bratislava, Slovakia
[p]Stefan-Meyer-Institut für subatomare Physik, Boltzmangasse 3, 1090 Vienna, Austria
[q]Niigata University, 8050 Ikarashi 2-no-cho, Nishi-ku, 950-2181 Niigata, Japan

[1]Co-spokesperson
[2]Spokesperson

Bibliography

[1] S. Weinberg, Phys. Rev. D **11**, 3583 (1975).

[2] E. Witten, Nucl. Phys. B **156**, 269 (1979).

[3] D. Jido, H. Nagahiro, and S. Hirenzaki, Phys. Rev. C **85**, 032201 (2012).

[4] H. Nagahiro *et al.*, Phys. Rev. C **87**, 045201 (2013).

[5] S. H. Lee and T. Hatsuda, Phys. Rev. D **54**, 1871 (1996).

[6] T. D. Cohen, Phys. Rev. D **54**, 1867 (1996).

[7] K. Suzuki *et al.*, Phys. Rev. Lett. **92**, 072302 (2004).

[8] E. E. Kolomeitsev, N. Kaiser, and W. Weise, Phys. Rev. Lett. **90**, 092501 (2003).

[9] D. Jido, T. Hatsuda, and T. Kunihiro, Phys. Lett. B **670**, 109 (2008).

[10] H. Nagahiro, M. Takizawa, and S. Hirenzaki, Phys. Rev. C **74**, 045203 (2006).

[11] P. Costa, M. C. Ruivo, and Y. L. Kalinovsky, Phys. Lett. B **560**, 171 (2003).

[12] H. Nagahiro and S. Hirenzaki, Phys. Rev. Lett. **94**, 232503 (2005).

[13] Y. Nambu and G. Jona-Lasinio, Phys. Rev. **122**, 345 (1961).

[14] Y. Nambu and G. Jona-Lasinio, Phys. Rev. **124**, 246 (1961).

[15] M. Kobayashi and T. Maskawa, Prog. Theor. Phys. **44**, 1422 (1970).

[16] M. Kobayashi, H. Kondo, and T. Maskawa, Prog. Theor. Phys. **45**, 1955 (1971).

[17] G. 't Hooft, Phys. Rev. Lett. **37**, 8 (1976).

[18] S. Sakai and D. Jido, Phys. Rev. C **88**, 064906 (2013).

[19] S. D. Bass and A. W. Thomas, Phys. Lett. B **634**, 368 (2006).

[20] M. Nanova *et al.*, Phys. Lett. B **710**, 600 (2012).

[21] M. Nanova *et al.*, Phys. Lett. B **727**, 417 (2013).

[22] E. Y. Paryev, J. Phys. G: Nucl. Part. Phys. **40**, 025201 (2013).

[23] E. Czerwiński *et al.*, Phys. Rev. Lett. **113**, 062004 (2014).

[24] P. Moskal *et al.*, Phys. Lett. B **474**, 416 (2000).

[25] P. Moskal *et al.*, Phys. Lett. B **482**, 356 (2000).

[26] T. Csörgő, R. Vértesi, and J. Sziklai, Phys. Rev. Lett. **105**, 182301 (2010).

[27] K. Itahashi *et al.*, Letter of Intent for GSI-SIS (unpublished) (2011).

[28] K. Itahashi *et al.*, Prog. Theor. Phys. **128**, 601 (2012).

[29] O. Morimatsu and K. Yazaki, Nucl. Phys. A **435**, 727 (1985).

[30] O. Morimatsu and K. Yazaki, Nucl. Phys. A **483**, 493 (1988).

[31] GSI web page, https://www.gsi.de/en/research/accelerator_facility.htm.

[32] H. Geissel *et al.*, Nucl. Instrum. Methods B **70**, 286 (1992).

[33] T. Yamazaki *et al.*, Z. Phys. A **355**, 219 (1996).

[34] T. Yamazaki *et al.*, Phys. Lett. B **418**, 246 (1998).

[35] H. Gilg *et al.*, Phys. Rev. C **62**, 025201 (2000).

[36] K. Itahashi *et al.*, Phys. Rev. C **62**, 025202 (2000).

[37] H. Geissel *et al.*, Phys. Rev. Lett. **88**, 122301 (2002).

[38] H. Geissel *et al.*, Phys. Lett. B **549**, 64 (2002).

[39] Web page of GICOSY program, http://web-docs.gsi.de/~weick/gicosy/.

[40] B. Jurado *et al.*, Nucl. Instrum. Methods A **483**, 603 (2002).

[41] R. Anne *et al.*, GSI Scientific Report 1989, 257 (1990).

[42] R. Janik *et al.*, Nucl. Instrum. Methods A **640**, 54 (2011).

[43] M. Tabata *et al.*, Nucl. Instrum. Methods A **623**, 339 (2010).

[44] R. Orito *et al.*, IEEE Trans. Nucl. Sci. **51**, 1337 (2004).

[45] T. Yoneyama, Master Thesis at Tokyo Institute of Technology (2001).

[46] H. G. Essel *et al.*, IEEE Trans. Nucl. Sci. **43**, 132 (1996).

[47] P. Berthet *et al.*, J. Phys. G: Nucl. Phys. **8**, L111 (1982).

[48] R. K. Carnegie *et al.*, Nucl. Instrum. Methods A **538**, 372 (2005).

[49] O. B. Tarasov and D. Bazin, Nucl. Instrum. Methods B **266**, 4657 (2008).

[50] Web page of ATIMA program, http://web-docs.gsi.de/~weick/atima/.

[51] J. Lindhard and A. H. Sørensen, Phys. Rev. A **53**, 2443 (1996).

[52] N. Iwasa *et al.*, Nucl. Instrum. Methods B **126**, 284 (1997).

[53] Y. Nara *et al.*, Phys. Rev. C **61**, 024901 (2000).

[54] Y. Higashi, private communication (2014).

[55] K. A. Olive *et al.*, Chin. Phys. C **38**, 090001 (2014).

[56] H. Nagahiro, private communication (2013).

[57] G. R. Smith *et al.*, Phys. Rev. C **30**, 593 (1984).

[58] C. Ciofi degli Atti, E. Pace, and G. Salmè, Phys. Rev. C **43**, 1155 (1991).

[59] M. Lacombe *et al.*, Phys. Lett. B **101**, 139 (1981).

[60] I. Lehmann, PhD Thesis at Universität zu Köln (2003).

[61] S. Barsov *et al.*, Eur. Phys. J. A **21**, 521 (2004).